Investigation of Quantum Phase Transitions in Ising-like Systems, by Torque Magnetometry and Neutron Scattering

Sara Eisenhardt
Supervisor: Kim Lefmann

May 2010

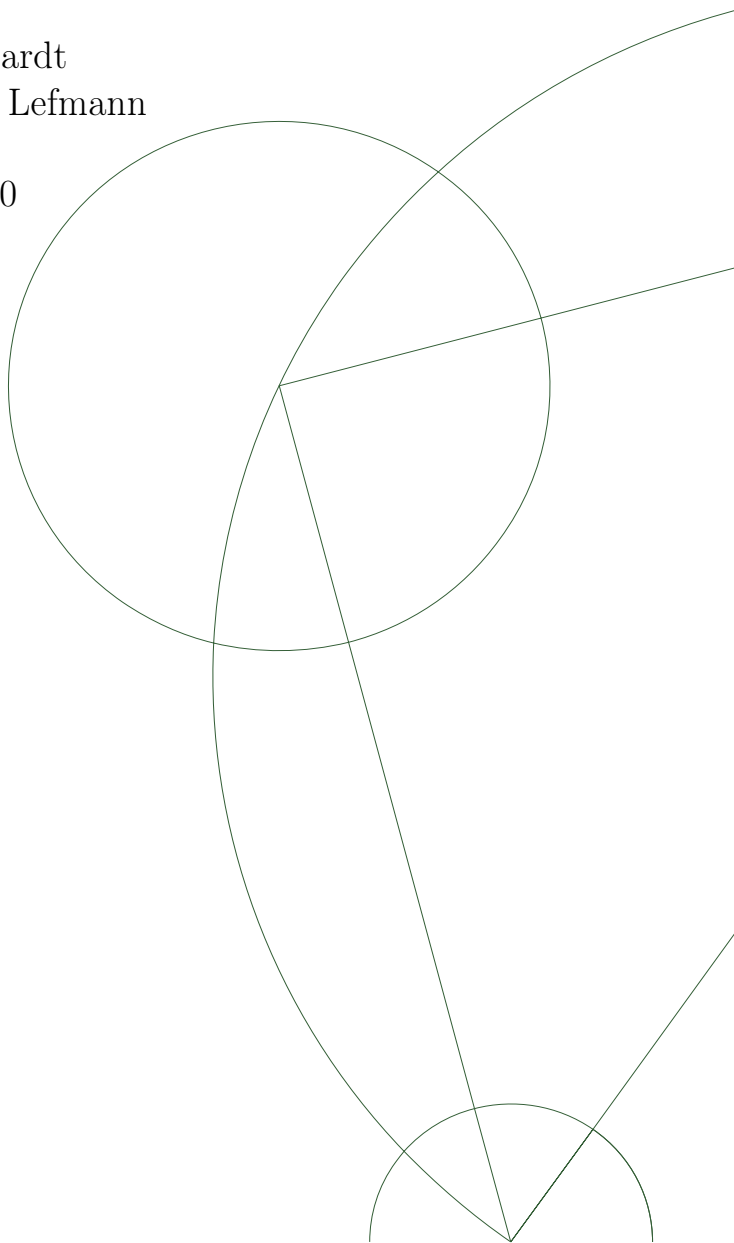

Preface and Acknowledgments

This thesis is the conclusion of the experimental work, I have conducted in order to fulfil the requirements for a Master of Science degree in physics at Copenhagen University. The calibration and testing of the setup was performed at the H. C. Ørsted laboratory, Niels Bohr Institute, Copenhagen University. The actual measurements was conducted at Ecole Polytechnique Fédérale de Lausanne (EPFL).
My supervisor on this project was associate professor Kim Lefmann, along with co-supervisors Finn Berg Rasmussen and professor Henrik Rønnow (EPFL). I wish to thank Kim Lefmann, Finn Berg Rasmussen, Jens Jensen and Henrik Rønnow for many inspiring discussions. A thank to Henrik Rønnow for giving me the opportunity to perform the experiments at EPFL. Julian Piatek for help with running the dilution refrigerator at EPFL. Bastian Dalla Piazza for giving me the opportunity to use his mean field program. Further I thank Jonas Hauptmann and Thomas Sand Jespersen for their help with running the dilution refrigerator in Copenhagen and general help in the laboratory.
Dmitry Khakhulin for helping with the X-Ray diffraction. Thomas Stibius Jensen for helping with the Laue diffraction at DTU - RISØ. Mogens Christensen at the Institute of Chemistry, Århus University for letting me cut the crystal. Kristian Mølhave at Department of Micro- and Nanotechnology, DTU for helping with the preliminary strain gauge design. I would like to thank Jacob Larsen for the chance to perform neutron scattering experiments.Instrument responsibles Markos Skoulatos and Klaus Habicht at V2 (FLEX), Helmholtz-Zentrum Berlin (HZB).
I also wish to thank Kim Georg Lind, Thomas Nørskov Nielsen and Jacob Larsen for their help correcting the written words.

Copenhagen, May 2010
Sara Eisenhardt

Contents

Chapter 1

Introduction

1.1 Thermal Phase Transition

Phase transitions occur when an external parameter is being varied. This variation changes the characteristics of the system. Normally one thinks of a phase transition as a change in a system's properties when the temperature changes. The system has a certain order which is destroyed by thermal fluctuations (*i.e.* the temperature changes). An everyday example is the case of ice melting, where the crystal structure is destroyed. Below 0°C the H_2O molecules are bound in a crystal lattice making an ice structure, where the molecules stay very close to their lattice point. Above 0°C the H_2O molecules move almost freely around in the liquid phase. Why is it that all the H_2O molecules decide to become mobile at a certain temperature, changing the phase from ice to water? A phase transition like this can be understood through the competition of entropy S and energy E. From thermodynamics we know that a system in thermal equilibrium aims to minimize its free energy F. The free energy depends on the entropy, energy and temperature T (the temperature is measured in the absolute scale).

$$F = E - TS \tag{1.1}$$

The energy is determined by the interactions between the H_2O molecules,and it will be lowest in the ice phase, where the crystalline structure facilitates a close interaction. Entropy on the other hand is a measure of disorder in the system, it is the logarithm of the number of possible configurations g of a system: $S = k_B \log(g)$, where k_B is the Boltzmann constant. For water, the entropy represents all the possible states of the H_2O molecules. As the molecules in a liquid has more degrees of freedom than in the solid the entropy is greater in the water phase. For small temperatures the first term in the free energy will be dominant, this means that the free energy will be smallest in the ice phase. When the temperature rises the second term dominates and the free energy will be smallest in the liquid phase. The free energy of water and ice cross at 0°C where the phase transition takes place.
Phase transitions are divided into first and second order phase transitions. First-order phase transitions involve latent heat, the system either absorbs or releases an amount of energy. The temperature of the system will stay constant as heat is added. Because energy cannot be instantaneously transferred between the system and its environment,

some parts of the system have completed the transition while others have not. This is the case when boiling water, the water does not instantly turn into gas, but a mixture of water and water vapour bubbles are present simultaneously. Examples of second-order phase transitions are the ferromagnetic transition, superconductors and the super-fluid transition. Second order phase transitions can be described using Landau theory.

1.1.1 Second Order Phase Transitions

A second order phase, also called a continuous phase transition, can be characterized by parameters known as critical exponents. An important critical exponent is ν which describes the divergence of the correlation length approaching the critical temperature T_c. The correlation length ξ is a measure of how fluctuations in one region of space influence another region. If two points are separated by a distance r_{ij} larger than the correlation length they will each have fluctuations which are relatively independent, one say they are uncorrelated. This is expressed mathematically

$$\langle s_i^z s_j^z \rangle \propto e^{-r_{ij}/\xi} \tag{1.2}$$

where $\langle \ \rangle$ denotes the thermal average. As the temperature is decreased, thermal disordering decreases and at the critical point, the correlation length diverges (this is found experimentally).

$$\xi \propto \left(\frac{|T - T_c|}{T_c} \right)^{-\nu}. \tag{1.3}$$

The fact that the correlation length diverges at the critical point means that very far points become correlated.

1.2 Quantum Phase Transition

For thermal phase transitions the order present at lower temperatures is destroyed by thermal fluctuations. Another type of phase transition is the quantum phase transition (QPT) which takes place at zero temperature, where thermal fluctuations are completely suppressed. The quantum phase transition's change of system properties is thus not a consequence of a variation in temperature, but rather a non-thermal control parameter. This parameter can be, *e.g.*, pressure, magnetic field, or chemical doping. For QPTs the order is destroyed by quantum fluctuations which are rooted in the Heisenberg uncertainty principle. Heisenberg's uncertainty principle means that conjugate pairs of physical properties (like position and momentum as in the example below) cannot be known exactly.

$$\Delta x \, \Delta p \geq \frac{\hbar}{2} \tag{1.4}$$

Therefore a system even at zero temperature will display fluctuations. Features of the QPT can in principle be seen even at finite temperature, as long as the thermal fluctuations are smaller than the quantum fluctuations. These quantum fluctuations may be large enough to cause a phase transition which can cause a macroscopic change. [3, 40, 41, 49]

1.3 $LiHoF_4$

In this thesis, the work is based on the insulator lithium holmium fluoride. As a crystal, $LiHoF_4$ has a tetragonal structure, and at sufficiently low temperatures it only has its holmium spins as a magnetic degree of freedom. The holmium spins have an easy axis,

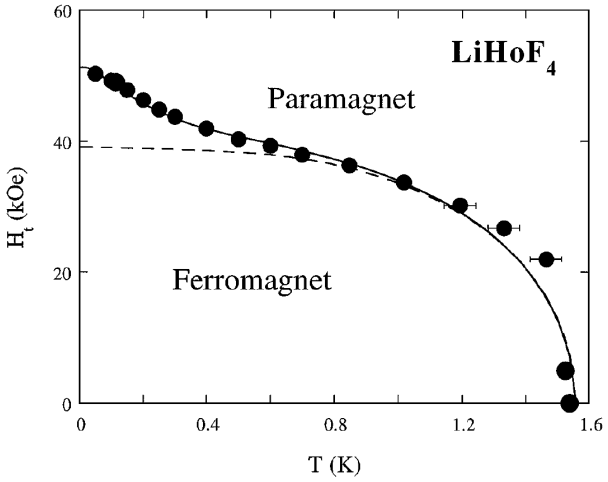

Figure 1.1: The magnetic phase diagram for $LiHoF_4$, obtained by Bitko *et al.* [4]. The figure shows the transition from the ordered (ferromagnetic) phase to the disordered (paramagnetic) phase. The ordered phase breaks down at the solid line, which terminates in the quantum critical point. The dashed line is a mean-field theory including only the electronic spin degrees of freedom, the solid line is a mean-field theory including the hyperfine coupling. The deviation between the full and dashed line is due to the nuclear spin.

i.e. they prefer to point up or down with respect to a certain crystallographic axis. This means that the system can be understood using the Ising model. The spins at the holmium atoms interact through the dipolar interaction and the ground state is a ferromagnet.

1.4 Motivation

The overall idea behind this project is to be able to measure the magnetization of $LiHoF_4$ in a transverse field while controlling the sample with an external "handle". This handle can be through nuclear magnetic resonance (NMR), where the response of nuclear spins to radio frequency fields is measured. The idea is to reverse the technique and manipulate the nuclear spins by NMR to gain indirect control of the electronic magnetism.
A setup which could measure the magnetization of $LiHoF_4$ at low temperatures was built. A cantilever, which could measure the torque caused by the sample when exposed to a magnetic field, was developed. When a strain gauge is deformed it changes its electrical resistance. Placing the strain gauge on one side of the cantilever and the sample on the other and connecting the strain gauge in a Wheatstone circuit made it possible to measure the torque via the change in voltage using a lock-in amplifier.

The second part of the original idea, *i.e.* controlling the nuclear spins by NMR, was unfortunately never commenced due to time constraints.

Chapter 2

Theoretical Background: The One-dimensional Ising Model

2.1 Quantum Phase Transitions

At low temperatures quantum fluctuations play the role of disorder just like temperature at non-zero temperature. If we first consider the case with no external magnetic field then the only factor to change the system is the temperature. Small thermal fluctuations will cause some of the spins to flip, *e.g.* if the crystal were in a ground state with all the spins pointing up, thermal fluctuations will cause some of them to point down. As the temperature increases, the number of spins pointing down increases, until there on average is an equal amount of spin up and spin down, where the order parameter $\boldsymbol{m}$ is zero. This is a conventional, second-order phase transition, driven solely by thermal fluctuations. At the Curie temperature, the material changes from a ferromagnetic state $\boldsymbol{m} > 0$ to a paramagnetic state $\boldsymbol{m} = 0$. With the insulator $LiHoF_4$ it is possible to destroy the ferromagnetic order even at zero temperature. Applying an external magnetic field perpendicular to the spin orientation, allows quantum tunnelling between the spin up and spin down states. If the magnetic field is larger than a critical field, H_c, the tunnelling events occur so often that the ground state becomes a quantum paramagnet. This actually means that a phase transition can take place, not driven by temperature but entirely by quantum fluctuations.
As opposed to the classical paramagnet one cannot think of the quantum paramagnetic state as having spins which are fluctuating between the up and down states. The "quantum" paramagnet ground state is rather a superposition of the spin up and spin down states. It should be noted that in the extreme limit, with very high fields, they point in the direction of the field [49].
Quantum phase transitions of second order can be characterized by an energy scale which characterizes some spectral density of fluctuations at zero temperature. This energy Δ could be the energy between the first excited state and the ground state. This energy gap will often go to zero as some, non-thermal tunable parameter g approaches its critical value g_c. This can be written as a power law

$$\Delta \sim J|g - g_c|^{z\nu} \tag{2.1}$$

where J is the energy scale of a characteristic microscopic coupling, *i.e.* the interaction of spins, and $z\nu$ is a critical exponent. The behaviour in equation (2.1) is valid both for $g < g_c$ and $g > g_c$ with the same value of the exponent $z\nu$, but with different non-universal proportionality constants. In addition to a vanishing energy scale, second order phase transition have a characteristic length scale ξ describing correlations between spins. This length diverges as

$$\xi^{-1} \sim \Lambda |g - g_c|^{\nu} \tag{2.2}$$

where ν is a critical exponent and Λ is an inverse length scale of the order of inverse lattice spacing.
The ratio of the exponents in (2.1) and (2.2) is z, the characteristic energy scale vanishes as the zth power of the characteristic inverse length scale

$$\Delta \sim \xi^{-z}. \tag{2.3}$$

[40]

2.2 The Transverse Field Ising Model

A simple model for the $LiHoF_4$ system is 1d the Ising model in a transverse magnetic field B. If the z-axis is chosen to be the easy spin axis the Hamiltonian has the form

$$\mathscr{H} = -\sum_{<ij>} J_{ij} S_i^z \cdot S_j^z - B \sum_i S_i^x \tag{2.4}$$

where S_i^x and S_j^z are the x and z components of holmium spin at lattice position i or j respectively. It should be noted that $g\mu_B$ from the Zeeman term equals one, and has thus been omitted in the above Hamiltonian. The first term describes the ferro-

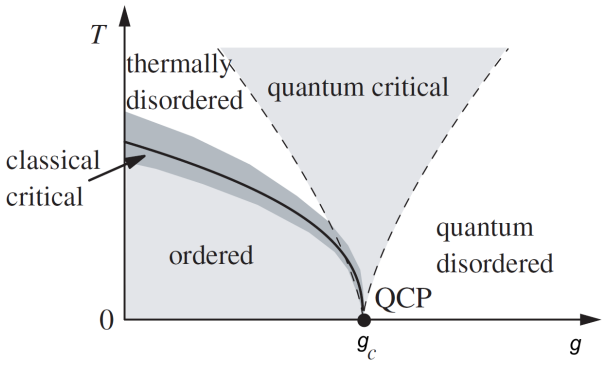

Figure 2.1: Generic phase diagram near the quantum critical point (QCP). g represents a non-thermal control parameter used to tune the system through the quantum phase transition - in our case the magnetic field B, figure adapted from [49].

or antiferromagnetic interaction between the spins, dependent on the sign of J. If J is positive the coupling is ferromagnetic, if J is negative the coupling is antiferromagnetic and if $J = 0$ the spins are non-interacting. The second term describes the effect of the

transverse field. Without an external magnetic field, *i.e.* $B = 0$, the model reduces to the standard Ising model. Increasing temperature will randomize the spins, thereby reducing the total magnetization, and above a critical temperature - 1.53 K for $LiHoF_4$ - the crystal becomes a paramagnet. To understand the effect of a transverse magnetic field the second part of the Hamiltonian can be rewritten, $B\sum_i S_i^x = \frac{1}{2}B\sum_i(S_i^+ + S_i^-)$, where S_i^+ and S_i^- are the spin flip operators at site i. From this expression it is clear that the transverse field will cause spin flipping. As the transverse magnetic field increases and crosses some critical value B_c these spin flips destroy the long-range ferromagnetic order, even at zero temperature. This is a quantum phase transition driven solely by quantum fluctuations. It has a phase diagram as illustrated in figure 2.1. [49, 26]

2.3 Calculation of the 1d Ising Model in a Transverse Magnetic Field

In this chapter the one-dimensional Ising model will be examined more thoroughly. The aim is to understand the Ising model in a transverse magnetic field, as this is the model to describe the $LiHoF_4$ system. The Ising model is the simplest model of ferromagnetism, it describes the transition between order and disorder. Ferromagnets are often anisotropic, which means the system has an easy axis. In this direction the energy is lower than the other directions. In the case of the Ising model this is exaggerated as it is assumed that the spin can only point along or against this direction. If we imagine a system of N spins residing on a lattice. The spins interact with their nearest neighbour through a coupling constant J. In this model the spins only interact with their nearest neighbour and the interaction is only along one axis, while the external magnetic field is applied perpendicular to this direction. This is described by the Hamiltonian

$$\mathscr{H} = -J\sum_n S_n^z S_{n+1}^z - Jg\sum_n S_n^x \tag{2.5}$$

with a constant external magnetic field B. The constant g in front of the Zeeman term is the dimensionless parameter $g = \frac{B}{J}$, that will show to tune the quantum phase transition. In the calculation to follow we will show that the 1d Ising model in a transverse field has two phases. [25].

2.3.1 Limiting Cases

Before performing the exact solution of the Ising model in a transverse magnetic field it can be useful to examine the limits of large $g = \frac{B}{J}$ and small $g = \frac{B}{J}$.

$g \gg 1$

If $g \gg 1$ the second part of (2.5) dominates

$$\begin{aligned}\mathscr{H} &= -Jg\sum_n S_n^x \\ &= -\frac{Jg}{2}\sum_n (S_n^+ S_n^-)\end{aligned} \tag{2.6}$$

In the ground state the S^z components are totally uncorrelated. To first order in $1/g$ the exchange part of the Hamiltonian starts to play a role, thus correlations in S^z will be induced. For g large enough these correlations are expected to remain short-ranged and fall of as $< 0|S_n^z S_{n+1}^z|0 > \sim \exp(\frac{|r_n - r_{n+1}|}{\xi})$ where ξ is the correlation length. This is known as a quantum paramagnet.

$g \ll 1$

If $g \ll 1$ the first part of (2.5), coupling neighbouring sites, dominates

$$\mathscr{H} = -J \sum_n S_n^z S_{n+1}^z. \tag{2.7}$$

Thus at $g = 0$ all the spins will point up or down, thus resulting in an ordered phase. If g is exactly zero, the ground state has the energy $2NJ$. The lowest excitation above the ground state is to flip half of the chain, hence only one bond is broken and thus costs JN. This first flipped spin point can move lattice position without costing additional energy, as there is still only one broken bond. The correlations of the S^z component are expected to be long-ranged.
In the limit of $g = \infty$, which corresponds to a strong applied magnetic field, there is only one ground state, the spin align along the field direction. The other phase, which is the weak field phase, has two ground states either the spin points up or down. Without an applied field these two states have the same energy and the system must choose one, resulting in a spontaneous breaking of symmetry. There must exist a point where the correlations change and this is the critical point. Calculating the exact solution to the Ising chain in a transverse field, as performed below, shows that the critical point is at $g_c = 1$. [40]

2.3.2 Jordan-Wigner Transformation: From Spins to Fermions

The Jordan-Wigner transformation maps the spin operators onto fermionic creation and annihilation operators. By the use of the Jordan-Wigner transformation it is possible to express the spins as a function of c_j, $c_j^\dagger$ and the number operator $n_j = c_j^\dagger c_j$ with eigenvalues 0 and 1. The number operator represents the number of fermions on site j. We define

$$S_j^- = c_j \exp\left(i\pi \sum_{r<j} \boldsymbol{n_r}\right), \tag{2.8}$$

$$S_j^+ = \left(S_j^-\right)^\dagger = \exp\left(i\pi \sum_{r<j} \boldsymbol{n_r}\right) (c_j)^\dagger \text{ and} \tag{2.9}$$

$$S_j^z = 2n_j - 1. \tag{2.10}$$

The fermionic operators fulfil the usual commutation relations

$$\{c_j, c_{j'}^\dagger\} = c_j c_{j'}^\dagger + c_{j'}^\dagger c_j = \delta_{jj'} \tag{2.11}$$

and

$$\{c_j, c_{j'}\} = \{c_j^\dagger, c_{j'}^\dagger\} = 0. \tag{2.12}$$

Consider the quadratic term

$$S_j^x S_{j+p}^x = \left(S_j^+ + S_j^-\right)\left(S_{j+p}^+ + S_{j+p}^-\right) = S_j^+ S_{j+p}^+ + S_j^+ S_{j+p}^- + H.c.,$$

where H.c. is the Hermitian conjugate, also indicated by the symbol †.
The quadratic form can be written in terms of the fermionic operators

$$\begin{aligned} S_j^+ S_{j+p}^- &= \exp\left(-i\pi \sum_{r<j} c_r^\dagger c_r\right) c_j^\dagger c_{j+p} \exp\left(i\pi \sum_{r<j+p} c_r^\dagger c_r\right) \\ &= c_j^\dagger \exp\left(-i\pi \sum_{r<j} c_r^\dagger c_r\right) c_{j+p} \exp\left(i\pi \sum_{r<j+p} c_r^\dagger c_r\right) \\ &= c_j^\dagger c_{j+\rho} \exp\left(-i\pi \sum_{r<j} n_r + i\pi \sum_{r<j} n_r + i\pi \sum_{j\le r<j+p} n_r\right) \\ &= c_j^\dagger c_{j+\rho} \exp\left(i\pi \sum_{j\le r<j+p} n_r\right). \end{aligned} \tag{2.13}$$

From the sum it is clear that r is never equal to j, hence $c_r c_j^\dagger = -c_j^\dagger c_r$ and $c_r^\dagger c_j^\dagger = -c_j^\dagger c_r^\dagger$

$$\begin{aligned} S_j^+ S_{j+p}^+ &= \exp\left(-i\pi \sum_{r<j} c_r^\dagger c_r\right) c_j^\dagger \exp\left(-i\pi \sum_{r<j+p} c_r^\dagger c_r\right) c_{j+p} \\ &= c_j^\dagger c_{j+p}^\dagger \exp\left(-i\pi \sum_{r<j} n_r - i\pi \sum_{r<j} n_r - i\pi \sum_{j\le r<j+p} n_r\right) \\ &= c_j^\dagger c_{j+p}^\dagger \exp\left(-i\pi \sum_{r<j} n_r + i\pi \sum_{r<j} n_r + i\pi \sum_{j\le r<j+p} n_r\right) \\ &= c_j^\dagger c_{j+p}^\dagger \exp\left(i\pi \sum_{j\le r<j+p} n_r\right), \end{aligned} \tag{2.14}$$

where it has been used that $e^{-in\pi} = e^{in\pi}$.
$e^{in\pi} = 1 - 2n_r$, since $n = 0$ or 1, $e^{in\pi}$ must be either 1 or -1.
The following identity is also useful:

$$c_r^\dagger e^{in_r\pi} = c_r^\dagger\left(1 - 2c_r^\dagger c_r\right) = c_r^\dagger \tag{2.15}$$

$$c_r e^{in_r\pi} = c_r\left(1 - 2c_r^\dagger c_r\right) = -c_r \tag{2.16}$$

For p=1, nearest neighbour coupling

$$S_j^+ S_{j+1}^- = c_j^\dagger c_{j+1} \tag{2.17}$$

2.3.3 Rotation of the Coordinate System

As seen from equation (2.5), the system Hamiltonian is quadratic in S_j^z. Since $S_j^z = 2c_j^\dagger c_j - 1$, the term $S_j^z S_{j+1}^z$ would give us four c's which is not considered here. Rotating

around the y-axis: $S_j^x \to -S_j^z$ and $S_j^z \to S_j^x$ we get the following Hamiltonian

$$\mathscr{H} = -J\sum_j S_j^x S_{j+1}^x + B\sum_j S_j^z \tag{2.18}$$

Applying the Jordan-Wigner transformation and using the relation of (2.17) one gets:

$$\mathscr{H} = -J\sum_j \left(c_j^\dagger c_{j+1}^\dagger + c_j^\dagger c_{j+1} + c_{j+1}^\dagger c_j + c_{j+1}c_j\right) + B\sum_j \left(2c_j^\dagger c_j - 1\right).$$

The Hamiltonian now contains bilinear terms only, which can be diagonalized in reciprocal space. It should be noted that in this derivation we have ignored end effects, *i.e.* the special points at $j = 1$ and $j = N$, and assumed periodic boundary conditions.

2.3.4 Fourier Transformation: from Real to Reciprocal Space

The next transformation performed is a Fourier transformation as the problem becomes much easier in reciprocal space. The transformation takes the form

$$c_n = \frac{1}{\sqrt{N}}\sum_k a_k e^{ikn} \tag{2.19}$$

$$c_n^\dagger = \frac{1}{\sqrt{N}}\sum_k a_k^\dagger e^{-ikn} \tag{2.20}$$

where the sums are performed over N reciprocal points in the interval $-\pi < k \leq \pi$. A new set of Fermi operators $a_k^\dagger$ and a_k have been introduced. Like the c's the a's also satisfy the fermion anti-commutation relations:

$$\{a_k^\dagger, a_{k'}^\dagger\} = \{a_k^{,} a_{k'}\} = 0 \text{ and} \tag{2.21}$$

$$\{a_k^\dagger, a_{k'}\} = \delta_{k,k'} \tag{2.22}$$

Applying the Fourier transformation the Hamiltonian becomes

$$\begin{aligned}
\mathscr{H} =& -\frac{J}{N}\sum_{jkk'}\Big(a_k^\dagger a_{k'}^\dagger e^{-ij(k+k')}e^{-ik'} + a_k^\dagger a_{k'}e^{-ij(k-k')}e^{ik'} + a_k a_{k'}e^{-ij(k-k')}e^{-ik} \\
&+ a_k a_{k'}e^{ij(k+k')}e^{ik}\Big) + \frac{2B}{N}\sum_{jkk'} a_k^\dagger a_{k'}e^{-ij(k-k')} - BN \\
=& -\frac{J}{N}\sum_{jkk'} e^{-ij(k-k')}\left(a_k^\dagger a_{k'}^\dagger e^{ik'} + a_k^\dagger a_{k'}e^{ik} + a_k^\dagger a_{k'}e^{-ik} + a_{-k}a_{k'}e^{-ik}\right) \\
&+ \frac{2B}{N}\sum_{jkk'} a_k^\dagger a_{k'}e^{-ij(k-k')} - BN.
\end{aligned} \tag{2.23}$$

Noting that $\frac{1}{N}\sum_j e^{i(k'-k)j} = \delta_{k,k'}$, the Hamiltonian can be written in a much simpler form:

$$\begin{aligned}
\mathscr{H} &= -J\sum_k\left[\left(a_k^\dagger a_{-k}^\dagger + a_k^\dagger a_k\right)e^{ik'} + \left(a_k^\dagger a_k + a_{-k}a_k\right)e^{-ik}\right] + 2B\sum_k a_k^\dagger a_k - BN \\
&= -J\sum_k\left[\left(e^{ik} + e^{-ik}\right)a_k^\dagger a_k + a_k^\dagger a_{-k}^\dagger e^{ik} + a_{-k}a_k e^{-ik}\right] + 2B\sum_k a_k^\dagger a_k - BN
\end{aligned} \tag{2.24}$$

To simplify this expression further we rewrite two of the terms by making the transformation $k \to -k$,

$$\begin{aligned}
a_k^\dagger a_{-k}^\dagger e^{ik} + a_{-k}a_k e^{-ik} &= \frac{1}{2}\left(a_k^\dagger a_{-k}^\dagger + a_k^\dagger a_{-k}^\dagger\right) e^{ik} + \frac{1}{2}\left(a_{-k}a_k + a_{-k}a_k\right) e^{-ik} \\
&= \frac{1}{2}a_k^\dagger a_{-k}^\dagger e^{ik} + \underbrace{\frac{1}{2}a_k^\dagger a_{-k}^\dagger e^{ik}}_{k\to -k} + \underbrace{\frac{1}{2}a_{-k}a_k e^{-ik}}_{k\to -k} + \frac{1}{2}a_{-k}a_k e^{-ik} \\
&= \frac{1}{2}(a_k^\dagger a_{-k}^\dagger + a_k a_{-k})e^{ik} + \frac{1}{2}(a_{-k}^\dagger a_k^\dagger + a_{-k}a_k)e^{-ik} \\
&= -\frac{1}{2}(a_{-k}^\dagger a_k^\dagger + a_{-k}a_k)e^{ik} + \frac{1}{2}(a_{-k}^\dagger a_k^\dagger + a_{-k}a_k)e^{-ik} \\
&= \frac{1}{2}(a_{-k}^\dagger a_k^\dagger + a_{-k}a_k)(e^{-ik} - e^{ik}) \\
&= -i(a_{-k}^\dagger a_k^\dagger + a_{-k}a_k)\sin(k). \qquad (2.25)
\end{aligned}$$

This mean the Hamiltonian becomes

$$\mathscr{H} = -J\sum_k \left[2\left(\cos(k) - g\right)a_k^\dagger a_k - i\sin(k)(a_{-k}^\dagger a_k^\dagger + a_{-k}a_k)\right] \qquad (2.26)$$

where we have introduced $g = \frac{B}{J}$. The Hamiltonian contains terms aa and $a^\dagger a^\dagger$ which means that the number of fermions is not conserved. This can be solved by the Bogoliubov transformation.

2.3.5 The Bogoliubov Transformation

The Bogoliubov transformation introduces a new set of fermionic operators γ_k whose number is conserved.

$$\gamma_k = u_k a_k - iv_k a_{-k}^\dagger, \qquad (2.27)$$

With the usual anticommutation relations:

$$\{\gamma_k, \gamma_k^\dagger\} = \delta_{k,k'} \qquad (2.28)$$

and

$$\{\gamma_k^\dagger, \gamma_{k'}^\dagger\} = \{\gamma_k, \gamma_{k'}\} = 0 \qquad (2.29)$$

where u_k and v_k are real numbers satisfying $u_k^2 + v_k^2 = 1, u_{-k} = u_k$, and $v_{-k} = -v_k$. The inverse Bogoliubov transformation has the form

$$a_k = u_k\gamma_k + iv_k\gamma_{-k}^\dagger \qquad (2.30)$$

$$a_k^\dagger = u_k\gamma_k^\dagger - iv_k\gamma_{-k} \qquad (2.31)$$

The next step is to use the inverse transformation on the two terms $a_k^\dagger a_k$ and $a_{-k}^\dagger a_k^\dagger + a_{-k}a_k$ in equation (2.26). The first term transforms to

$$a_k^\dagger a_k = u_k^2\gamma_k^\dagger\gamma_k + v_k^2\gamma_{-k}\gamma_{-k}^\dagger + iu_k v_k\gamma_k^\dagger\gamma_{-k}^\dagger - iu_k v_k\gamma_{-k}\gamma_k, \qquad (2.32)$$

and the second term is transformed to:

$$a^\dagger_{-k}a^\dagger_k + a_{-k}a_k = u_k^2\gamma^\dagger_{-k}\gamma^\dagger_k + v_k^2\gamma_k\gamma_{-k} - iu_kv_k\gamma^\dagger_{-k}\gamma_{-k} + iu_kv_k\gamma_{-k}\gamma^\dagger_k + u_k^2\gamma_{-k}\gamma_k + v_k^2\gamma^\dagger_k\gamma^\dagger_{-k} + iu_kv_k\gamma_{-k}\gamma^\dagger_{-k} - iu_kv_k\gamma^\dagger_k\gamma_k.$$

where we have used the anti-commutator relations and assumed $k \neq 0$.
Remember that the Hamiltonian may not contain any terms like $\gamma^\dagger_k\gamma^\dagger_k$ and $\gamma_k\gamma_k$ as this will violate the conservation of fermions. Hence any such terms should cancel out. This happens when,

$$\begin{aligned}
&(u_k^2\gamma^\dagger_{-k}\gamma^\dagger_k + v_k^2\gamma_k\gamma_{-k} + u_k^2\gamma_{-k}\gamma_k + v_k^2\gamma^\dagger_k\gamma^\dagger_{-k})i\sin(k) \\
&+ (iu_kv_k\gamma^\dagger_k\gamma^\dagger_{-k} - iu_kv_k\gamma_{-k}\gamma_k)2(\cos(k) - g) = 0 \\
&\quad\Downarrow \\
&(v_k^2 - u_k^2)(\gamma^\dagger_k\gamma^\dagger_{-k} + \gamma_k\gamma_{-k})i\sin(k) + iu_kv_k(\gamma^\dagger_k\gamma^\dagger_{-k} + \gamma_k\gamma_{-k})2(\cos(k) - g) = 0 \\
&\quad\Downarrow \\
&(v_k^2 - u_k^2)i\sin(k) + 2iu_kv_k = 0 \\
&\quad\Downarrow \\
&\frac{2u_kv_k}{v_k^2 - u_k^2} = -\frac{\sin(k)}{\cos(k) - g}.
\end{aligned} \tag{2.33}$$

The constants u_k and v_k can be chosen to ensure the conservation of fermions. If we choose $u_k = \cos(\frac{\theta}{2})$ and $v_k = \sin(\frac{\theta}{2})$ for some θ, a simple calculation shows that equation (2.33) is satisfied when

$$\frac{2u_kv_k}{v_k^2 - u_k^2} = \frac{2\sin(\frac{\theta}{2})\cos(\frac{\theta}{2})}{\sin^2(\frac{\theta}{2}) - \cos^2(\frac{\theta}{2})} = \frac{\sin(\theta)}{\cos(\theta)} = \tan(\theta)$$

$$\boxed{\tan(\theta) = \frac{\sin(k)}{\cos(k) - g}} \tag{2.34}$$

For this choice of u_k and v_k,

$$\begin{aligned}
a^\dagger_ka_k &= u_k^2\gamma^\dagger_k\gamma_k + v_k^2\gamma_{-k}\gamma^\dagger_{-k} = u_k^2\gamma^\dagger_k\gamma_k + v_k^2(1 - \gamma^\dagger_{-k}\gamma_{-k}) \\
a^\dagger_{-k}a^\dagger_k + a_{-k}a_k &= -iu_kv_k\gamma^\dagger_{-k}\gamma_{-k} + iu_kv_k(1 - \gamma^\dagger_k\gamma_k) + iu_kv_k(1 - \gamma^\dagger_{-k}\gamma_{-k}) - iu_kv_k\gamma^\dagger_k\gamma_k
\end{aligned}$$

This finally results in a transformed Hamiltonian

$$\begin{aligned}
\mathscr{H} &= -J\sum_k \Big[2\left(\cos(k) - g\right)a^\dagger_ka_k - i\sin(k)(a^\dagger_{-k}a^\dagger_k + a_{-k}a_k)\Big] - BN \\
&= -J\sum_k \Big[2\left(\cos(k) - g\right)\Big((u_k^2 - v_k^2)\gamma^\dagger_k\gamma_k + v_k^2\Big) - i\sin(k)\Big(-iu_kv_k\gamma^\dagger_{-k}\gamma_{-k} \\
&\qquad + iu_kv_k(1 - \gamma^\dagger_k\gamma_k) + iu_kv_k(1 - \gamma^\dagger_{-k}\gamma_k) - iu_kv_k\gamma^\dagger_{-k}\gamma_k\Big)\Big] - BN
\end{aligned} \tag{2.35}$$

where we have used that the sum is symmetric, *i.e.* $k \to -k$ and $\cos(k)$ is an even function. Reusing these facts for the other term results in

$$\begin{aligned}\mathscr{H} = -J\sum_k \Big[2\left(\cos(k)-g\right)\Big((u_k^2-v_k^2)\gamma_k^\dagger\gamma_k + v_k^2\Big) - i\sin(k)\Big(-iu_kv_k\gamma_k^\dagger\gamma_k \\ +iu_kv_k(1-\gamma_k^\dagger\gamma_k) + iu_kv_k(1-\gamma_k^\dagger\gamma_k) - iu_kv_k\gamma_k^\dagger\gamma_k\Big)\Big] - BN. \end{aligned} \tag{2.36}$$

Notice that $\sin(k)$ is an odd function and that $v_{-k} = -v_k$. This results in cancellation of signs

$$\begin{aligned}\mathscr{H} = -J\sum_k \Big[2\left(\cos(k)-g\right)\left((u_k^2-v_k^2)\,\gamma_k^\dagger\,\gamma_k + v_k^2\right) \\ +2u_kv_k\sin(k)\Big(1-2\gamma_k^\dagger\gamma_k\Big)\Big] - BN \end{aligned} \tag{2.37}$$

Writing up the Hamiltonian with a term $\gamma_k^\dagger\gamma_k$ and a constant:

$$\begin{aligned}\mathscr{H} = J\sum_k \Big[\underbrace{\left\{2(\cos(k)-g)(v_k^2-u_k^2)+4\sin(k)u_kv_k\right\}}_{\varepsilon_k}\gamma_k^\dagger\gamma_k \\ \underbrace{+\,2(\cos(k)-g)v_k^2 - 2\sin(k)u_kv_k\Big] - BN}_{\varepsilon_0} \end{aligned} \tag{2.38}$$

The ε_k prefactor can be simplified even further

$$\begin{aligned}\varepsilon_k =& 2(\cos(k)-g)(v_k^2-u_k^2) + 4\sin(k)u_kv_k \\ =& 2(\cos(k)-g)(v_k^2-u_k^2)\left(1+\frac{4\sin(k)u_kv_k}{2(\cos(k)-g)(v_k^2-u_k^2)}\right) \\ =& 2(\cos(k)-g)(v_k^2-u_k^2)\left(1+\frac{4u_k^2v_k^2}{(v_k^2-u_k^2)^2}\right) \\ =& 2(\cos(k)-g)\left(\frac{(u_k^2+v_k^2)^2}{(u_k^2-v_k^2)}\right) \\ =& 2(\cos(k)-g)\left(\frac{1}{(u_k^2-v_k^2)}\right). \end{aligned} \tag{2.39}$$

Here we have used equation (2.34) in the third step. The following relation can be used to find ε_k

$$u_k^2 - v_k^2 = -\sin^2\left(\frac{\theta}{2}\right) + \cos^2\left(\frac{\theta}{2}\right) = \frac{1}{\sqrt{1+\tan^2(\theta)}} \tag{2.40}$$

so

$$\begin{aligned}\varepsilon_k =& 2(\cos(k)-g)\sqrt{1+\tan^2\theta} \\ =& 2(\cos(k)-g)\sqrt{1+\frac{\sin^2(k)}{(\cos(k)-g)^2}} \\ =& 2\sqrt{g^2-2g\cos(k)+1}. \end{aligned} \tag{2.41}$$

The minimum energy occurs for $k = 0$

$$\begin{aligned}\varepsilon_{k=0} =& 2\sqrt{g^2 - 2g + 1} \\ =& 2\sqrt{(1-g)^2} \\ =& 2|1-g|. \end{aligned} \tag{2.42}$$

The energy at $k = 0$ is illustrated in figure 2.2. There is a critical point at $g = 1$ where the energy goes to zero. The system is in one phase for $g > 1$ and in another phase for $g < 1$. Thus the 1d Ising model in a transverse field undergoes a phase transition as the parameter g is tuned.

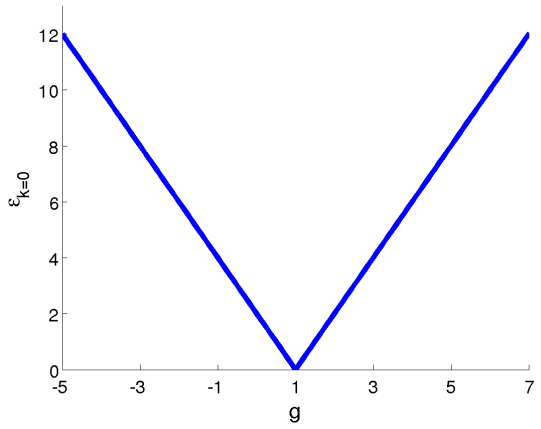

Figure 2.2: The minimum energy, which occurs at $k = 0$, the critical point is at $g = 1$.

One can also calculate $\varepsilon_{k=0}$, and then find the final Hamiltonian to be

$$\mathscr{H} = \sum_k \varepsilon_k \left(\gamma_k^\dagger \gamma_k - \frac{1}{2} \right) \tag{2.43}$$

This is the energy of each fermion which is infused to the system.
[26, 40, 8]

Chapter 3

Properties of the $LiHoF_4$ Crystal

This chapter will review some of the properties of $LiHoF_4$ and holmium (Ho). $LiHoF_4$ is a nearly ideal 3D Ising ferromagnet which undergoes a QPT in a transverse field of about 5 T.

3.1 The Crystal Structure

$LiHoF_4$ has a tetragonal Scheelite structure with lattice parameters: $a = b = 5.175$ Å and $c = 10.75$ Å [18]. In International Tables for Crystallography this is given by space

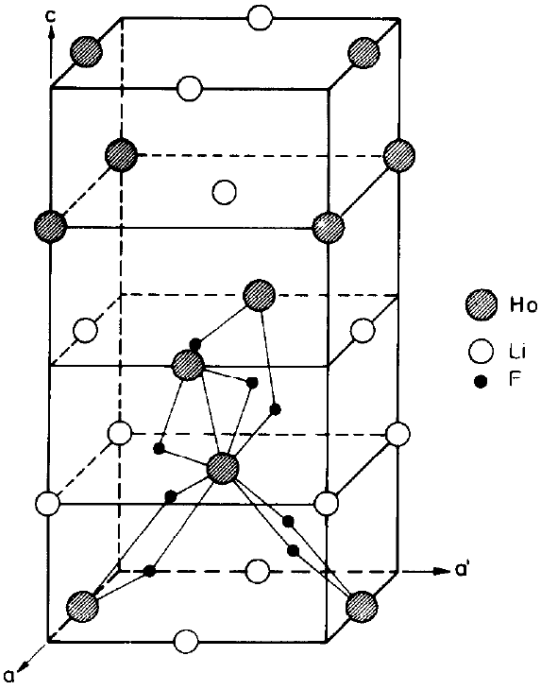

Figure 3.1: Structure of $LiHoF_4$ [27].

group $I4_1/a$ number 88 [12].

3.2 The Rare Earth Hamiltonian

The advantage of the $LiHoF_4$ system is that rare earth magnetic systems in general are well understood, see for example the book by Jensen and Mackintosh [17]. The unfilled shells of the $4f$ electrons couple according to Hund's rules, forming a total angular momentum J. Applying Hund's rules to Ho^{3+}, results in $J = 8$. It has $2J + 1 = 17$ magnetic states, split into four doublets and nine singlets. The lowest excited crystal-field level, which is a singlet, is placed about 11 K above the ground state doublet. This means that only the lowest crystal-field level is populated at low temperatures ($T < 4.2K$). The moments of Ho^{3+} are dipolar coupled. The total Hamiltonian includes the crystal-field, the hyperfine, the Zeeman, and the classical dipole-dipole interactions along with a nearest neighbour Heisenberg exchange interaction. From Rønnow *et al.* [39] the Hamiltonian has the form:

$$\mathscr{H} = \sum_i \mathscr{H}_{CF} + \sum_i A\boldsymbol{J_i} \cdot \boldsymbol{I_i} - \sum_i g\mu_B\mu_0 \boldsymbol{J_i} \cdot \boldsymbol{H} \tag{3.1}$$

$$- \sum_{i,j} \mathscr{H}_{Dip,i,j} - \frac{1}{2}\sum_{ij}^{nn} \mathscr{J}_{12}\boldsymbol{J_i} \cdot \boldsymbol{J_j} \tag{3.2}$$

where the z axis of the Hamiltonian is along the c axis of the crystal. These terms will be described in the following.

3.2.1 The Zeeman Energy

The Zeeman term describes the energy of a magnetic ion in a magnetic field. The magnetic field $\boldsymbol{H}$ interacts differently with electrons with different quantum numbers. States with the same energy, now have different energies - they have split up. According to the Wigner-Eckart theorem the matrix element of $\boldsymbol{L} + 2\boldsymbol{S}$ is proportional the the matrix elements of $\boldsymbol{J}$ and the Zeeman term can be written as

$$\mathscr{H}_{Zeeman} = -\mu_0\mu_B g\boldsymbol{H} \cdot \boldsymbol{J}. \tag{3.3}$$

The Landé g factor is the proportionality constant and is given by

$$g_L = \frac{1}{2}\frac{(3J(J+1) - L(L+1) + S(S+1))}{J(J+1)} \tag{3.4}$$

[25]

3.2.2 The Crystal Field

The crystal field Hamiltonian for one Ho^{3+} ion in its ground state $^5I_8$ can be written as

$$\begin{aligned}\mathscr{H}_{CF} =& B_2^0O_2^0 + B_4^0O_4^0 + B_6^0O_6^0 + B_4^4O_4^4 + B_4^{-4}O_4^{-4} \\ &+ B_6^4O_6^4 + B_6^{-4}O_6^{-4}\end{aligned} \tag{3.5}$$

where B_i^m are the crystal field parameters and O_i^m are the Stevens operators.

Following Hutchings [15] the Stevens operators are given by

$$\begin{aligned}
O_2^0 &= 3J_z^2 - J(J+1) \\
O_4^0 &= 35J_z^4 - (30J(J+1) - 25)J_z^2 \\
&\quad + 30(J(J+1))^2 - 6J(J+1) \\
O_4^4 &= \frac{1}{2}(J_+^4 + J_-^4) \\
O_6^0 &= 231J_z^6 - (315J(J+1) - 735)J_z^4 \\
&\quad + (105(J(J+1))^2 - 525J(J+1) + 294)J_z^2 \\
&\quad - 5(J(J+1))^3 + 40(J(J+1))^2 - J(J+1) \\
O_6^4(c) &= \frac{1}{4}(11J_z^2 - J(J+1) - 38)(J_+^4 + J_-^4) \\
&\quad + (J_+^4 + J_-^4)(11J_z^2 - J(J+1) - 38)) \\
O_6^4(s) &= \frac{1}{4i}(11J_z^2 - J(J+1) - 38)(J_+^4 - J_-^4) \\
&\quad + (J_+^4 - J_-^4)(11J_z^2 - J(J+1) - 38))
\end{aligned} \tag{3.6}$$

where $J_\pm = J_x \pm iJ_y$. The values of the B_i^m parameters are given in table 3.2.2

B_2^0 [meV]	B_4^0 [meV]	B_4^4 [meV]	B_6^0 [meV]	$B_6^4(s)$ [meV]	$B_6^4(c)$ [meV]
-0.06	0.35 10^{-3}	3.6 10^{-3}	0.04 10^{-5}	7.0 10^{-5}	$\pm$ 0.98 10^{-5}

Table 3.1: Crystal field parameters from [39].

3.2.3 The Hyperfine Coupling

The second term in the Hamiltonian describes the interaction between the electronic moments J and the nuclear spin $I = \frac{7}{2}$ of the ith holmium nuclei cause an additional splitting of the energy.

$$\mathscr{H}_{HF} = \sum_i A\boldsymbol{J_i} \cdot \boldsymbol{I_i} \tag{3.7}$$

Figure 3.2 shows the ground state doublet and the first excited state as a function of transverse magnetic field. The hyperfine splitting into $2I + 1 = 8$ equally spaced levels is shown for each state is shown. The hyperfine splitting is normally very small but has been shown to have a large effect on the behaviour around the quantum phase transition, from the neutron scattering data by Rønnow *et al.* [38]. Both heat capacity [27] measurements and hyperfine resonance [24] show that the coupling $A = 3.36$ μeV, which is identical for the case of the isolated ion. The splitting of the doublet at higher fields, seen in figure 3.2, is not caused by direct exchange between the doublet state, but by mixing of the doublet states with higher order states. Application of a transverse magnetic field mixes higher levels into the ground state, which split the doublet.

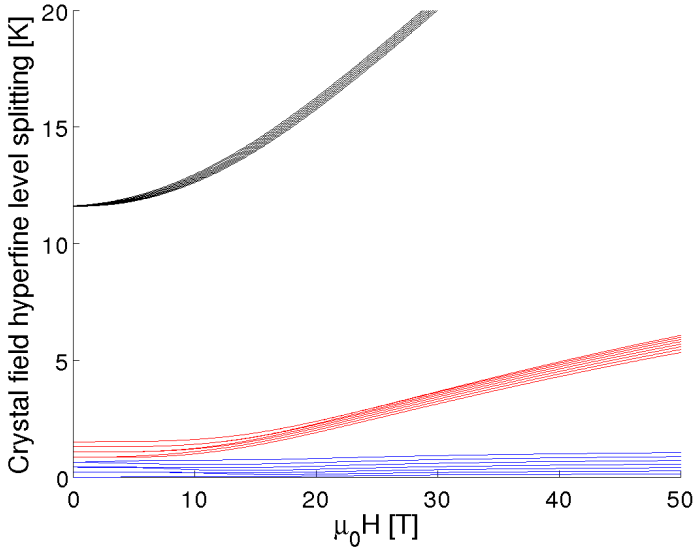

Figure 3.2: The three lowest crystal field levels for a sole Ho^{3+} ion. The two lowest levels (blue and red) and the first excited state (black) as a function of applied transverse magnetic field. The hyperfine interaction splits each state into $2I + 1 = 8$ equally spaced levels. The calculation, performed by Jens Jensen, contains both Zeeman, crystal field and hyperfine splitting.

3.2.4 The Classical Dipole-Dipole Interaction

The long ranging dipole-dipole coupling between the Ho ions is foremost responsible for the magnetic ordering in $LiHoF_4$. The interaction energy between two magnetic dipoles has the form

$$\sum_{i,j} \mathscr{H}_{Dip,i,j} = \frac{\mu_0}{4\pi} g_L^2 \mu_B^2 \sum_{i,j} \frac{\boldsymbol{J_i} \cdot \boldsymbol{J_j} - 3(\boldsymbol{J_i} \cdot \hat{\boldsymbol{r}}_{\boldsymbol{i}})(\boldsymbol{J_j} \cdot \hat{\boldsymbol{r}}_{\boldsymbol{j}})}{r_{ij}^3} \tag{3.8}$$

where $\boldsymbol{r_{ij}}$ is vector separating the two dipoles characterized by $\boldsymbol{J_i}$ and $\boldsymbol{J_j}$ [36]. There are $N = 1.389 \cdot 10^{22}$ cm^{-3} Ho ions per unit volume, and the dipole coupling strength is given by $\mathscr{J}_D = (g\mu_B)^2 N = 1.1654$ μeV.

3.2.5 Heisenberg Exchange Interaction

The nearest neighbour exchange coupling is also included, in the form of an isotropic Heisenberg.

$$\mathscr{H} = -\frac{1}{2} \sum_{ij}^{nn} \mathscr{J}_{12} \boldsymbol{J_i} \cdot \boldsymbol{J_j} \tag{3.9}$$

In the case of $LiHoF_4$ the exchange interaction is weak compared to the dipole coupling. The terms that dominate the magnetic properties of $LiHoF_4$ are the crystal field and the dipole-dipole interaction.

3.3 The Effective Ising Model

This section will argue why it is possible to use the simpler spin $\frac{1}{2}$ transverse-field Ising model, in the case of $LiHoF_4$, instead of the general Heisenberg model with a crystal field. If a strong anisotropy is present in a crystal, where the interaction is described as a Heisenberg system, the Hamiltonian can be changed to an effective Hamiltonian - in this case the Ising Hamiltonian. If we describe the system with a Heisenberg and a crystal field of the form O_2^0,the Hamiltonian has the form:

$$\mathscr{H} = -\sum_{<ij>} J_{ij} S_i S_j - D \sum_i (S_i^z)^2 \tag{3.10}$$

The ground state consists of two degenerate states - a doublet. We choose D such that

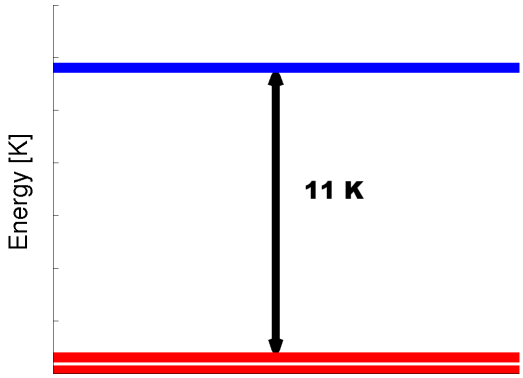

Figure 3.3: The three lowest crystal field levels. The doublet (red) and the first excited state (blue) corresponding to an energy of 11 K above the doublet.

the first excited state is 11 K above the doublet as in $LiHoF_4$. This means that at low temperatures ($T < 4.2K$) the only thermally accessible crystal state is the doublet. We can therefore allow ourselves to only look at the doublet states. If we apply the Hamiltonian on two spins and assumes that the interaction J is identical then the Hamiltonian will be

$$\begin{aligned}
\mathscr{H} =& J\boldsymbol{S_1}\cdot\boldsymbol{S_2} - D\left((S_1^z)^2 + (S_2^z)^2\right) \\
=& JS_1^zS_2^z + \frac{J}{2}\left(S_1^+S_2^- + S_1^-S_2^+\right) - D\left((S_1^z)^2 + (S_2^z)^2\right) \\
\simeq& JS_1^zS_2^z - D\left((S_1^z)^2 + (S_2^z)^2\right).
\end{aligned} \tag{3.11}$$

Where degenerate first order perturbation theory is used in the last step. The lowering and raising dagger on the states will be zero as the first excited state is too far away. Thus only the z component of the spins remain. Thus at low temperatures the behaviour is that of a transverse-field Ising model.
This can also be understood by looking at the longitudinal and transverse g-factors. The crystal field ground state is a doublet with a longitudinal g-factor $g_{\parallel} = 13.3$ - 14.1 (z direction) and a transverse g-factor $g_{\perp} \simeq 0$ [28] (both x and y direction). The transverse susceptibility is measured to be very low. As $g_{\perp} \simeq 0$, the transverse components of the interaction must also be zero.

If the known crystal parameters are used equation 3.5 can be solved in the basis of eigenstates $|m\rangle$ ($m = -8.....8$) of J_z. The g-factor is the proportionality constant between the magnetization and the angular momentum J, $\boldsymbol{m} = -g_J\mu_B\boldsymbol{J}$. If one assumes the particle has spin half the g-factor is the constant that multiplies the spin in order to get the right magnetization (if the particle is not spin half). The doublet states correspond to spin-$\frac{1}{2}$ eigenstates in equation (3.10) with a moment per Ho^{3+} spin of $\frac{g_\parallel}{2} \simeq 7\mu_B$. [38, 39, 14, 5]

3.4 Mean Field

The Hamiltonian describing collective spin phenomena is often to complicated to solve analytically. Thus the mean field approximation is widely used. The idea of mean field theory is to replace all interactions with an average or effective interaction. In the mean field approximation the fluctuations of the spin operator $< S >$ from its equilibrium position are considered small, *i.e.* $S - < S > \simeq 0$.

$$\boldsymbol{S_i} \cdot \boldsymbol{S_j} = (\boldsymbol{S_i} - < \boldsymbol{S_i} >) \cdot (\boldsymbol{S_j} - < \boldsymbol{S_j} >) + \boldsymbol{S_i} \cdot < \boldsymbol{S_j} > + \boldsymbol{S_j} \cdot < \boldsymbol{S_i} > - < \boldsymbol{S_i} > \cdot < \boldsymbol{S_j} > \tag{3.12}$$

The mean field approximation consist of neglecting the first term in equation (3.12). Mean field theories ignores correlations which become very important at the critical point. [2]

3.4.1 The Mean Field Program

A mean field based program has been used to calculate the electronic angular moment. Chapter 7 will show comparisons between our magnetization data and the mean field calculations, made by Bastian Dalla Piazza (EPFL) [34]. The program incorporates the the crystal field, the demagnetization field, the dipole interaction, the exchange interaction and the hyperfine interaction. The hyperfine interaction can be turned off, as this interaction slows down the calculations. In this work it was turned on at all times. The program incorporates the sample's shape, which is used for the demagnetization field. In our case the shape is that of a needle. In the mean field program it is possible to tune the exchange interaction in order to either obtain a correct critical temperature or field. In this work an exchange interaction of -0.54 μeV was used, resulting in the correct value for T_c, but not for the critical field. With this interaction the critical field is only 3 T, it is not possible to have correct value of both the critical temperature and field at the same time.
When running calculations either the field or temperature is held constant while scanning the other.

3.5 Existing Experimental Data on $LiHoF_4$

The magnetic properties of $LiHoF_4$ have been studied through a series of experimental techniques. Hansen *et al.* (1975) [14] measured the magnetization $\boldsymbol{m_s}$ and susceptibility χ at temperatures between 1.3 T and 300 T. From the susceptibility measurements $\chi_\parallel(T)$ and $\chi_\perp(T)$ were fitted and the the crystal field parameters B_n^m with

$(n, m) = (2, 0), (4, 0), (4, 4), (6, 0), (6, 4)$ were extracted. They found that the system or-

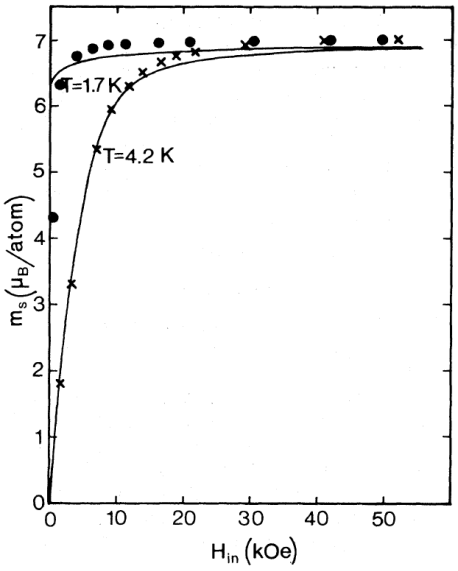

Figure 3.4: Magnetization as a function of inner magnetization $\boldsymbol{H_{in}}$ (they have compensated for the demagnetization field) at 1.3 K (circles) and 4.2 K (crosses), measured by Hansen *et al.* (1975) [14].

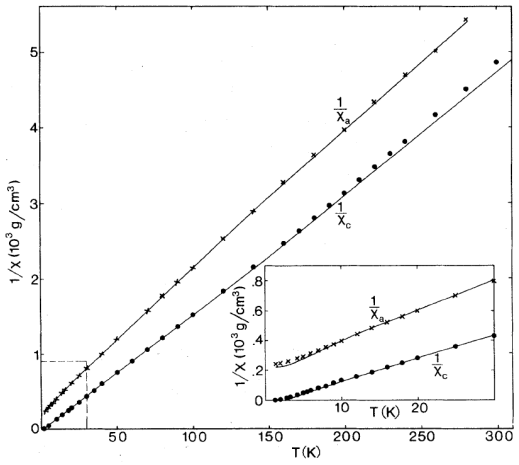

Figure 3.5: Susceptibility along the c axis (circles) and a axis (crosses) as a function of temperature, measured by Hansen *et al.* (1975) [14].

ders ferromagnetically at $T_c = 1.30 \pm 0.05$ K with saturation moments of 6.98 μ_B along the c axis. The critical temperature T_c found by Hansen *et al.* is somewhat lower than the value found in newer articles. Christensen *et al.* recorded the polarized light absorption spectra at 2 K in the spectra interval $4000 - 26000\ \mathrm{cm}^{-1}$, thereby having a direct measurement of the crystal field parameters. These parameters were roughly consistent with the parameters found by Hansen *et al.*. Electron spin resonance performed by Magariño *et al.* [24] revealed a hyperfine structure due to the coupling to the eight states of the $I = \frac{7}{2}$ nuclear states. They measured the coupling to be $A = 47.4 \pm 1.0$ mT corresponding to $47.4\ \mathrm{mT} \cdot \mu_B/k_B = 32$ mK. Mennenga *et al.* (1983) [27, 28] studied $LiHoF_4$ through heat capacity at temperatures between 0.06 and 7 K. They applied a longitudinal field parallel to the easy c-axis. Their measurements confirmed the value of the coupling $A = 3.36$ μeV.

In 1996 Bitko, Rosenbaum and Aeppli [4] measured the magnetic properties of $LiHoF_4$ in a magnetic field perpendicular to the spin direction. They measured the magnetic susceptibility as a function of temperature and magnetic field, and were then able to determine a (H, T) phase diagram, which is shown in figure 3.6. These measurements made it possible to find the critical exponent of the susceptibility $\chi \propto (T - T_c)^{-\gamma}$ [6]. The determined value of $\gamma = 1$ equals that of the mean field prediction, both at the classical phase transition with zero field and at the quantum phase transition at zero temperature.

Rønnow *et al.* (2005) [38] measured the excitation spectrum with the use of neutron spectroscopy, as the crystal was tuned to its quantum critical point by the use of a transverse magnetic field at 0.31 K. Thus it was possible to study the dynamics with neutron scattering and tune the quantum phase transition with a transverse field, the measure-

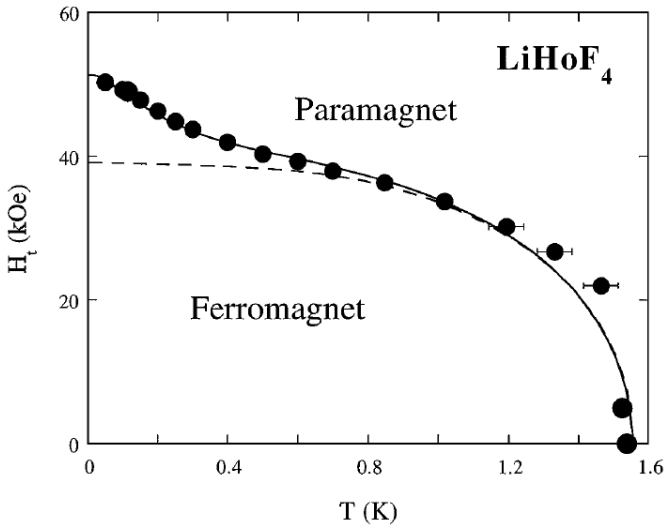

Figure 3.6: Phase diagram obtained through susceptibility (circles) by Bitko *et al.* [4] showing the transition from ferromagnet to paramagnet as a function of temperature and transverse field. The dashed line is a mean field theory including only the electronic spin degree of freedom, whereas the dotted line is a full mean field theory which also incorporates the hyperfine interaction.

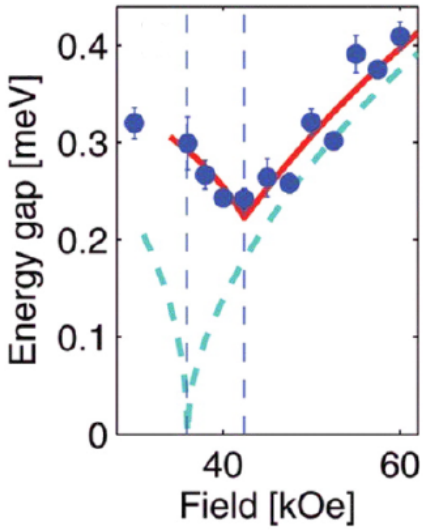

Figure 3.7: Field dependence of the lowest excitation in $LiHoF_4$ at T = 0.31 K (blue circles). The lines are calculated energies with (red solid) and without (blue dashed) hyperfine coupling. The electronic coupling to the nuclei prevents the expected mode softening, and thus a perfect phase transition.

ments are presented in figure 3.7. The electronic mode was expected to go soft (approach zero energy) at the quantum phase transition, but was prevented by the hyperfine coupling to the nuclear spins. This is consistent with calculation, as shown in figure 3.7, where calculations with hyperfine interactions very nicely follow the measurements. The calculation without the hyperfine coupling has the mode soften as expected, thus making it clear that the hyperfine coupling prevents a perfect phase transition.

Chapter 4

Low Temperature Techniques

In order to perform the desired experiments, the sample needs to be at low temperatures and it is furthermore important to be able to control this temperature.

4.1 Dilution Refrigerator

To be able to achieve a temperature down to ∼40 mK a dilution refrigerator was used. Figure 4.1 shows the principles of a dilution refrigerator. It uses a mixture of ^{3}He and ^{4}He which have boiling points of respectively 3.19 K and 4.23 K. The basic idea is to cool the two isotopes below ∼800 mK, where they will separate into two liquid phases, divided by a phase boundary. The ^{3}He rich phase is called the concentrated phase because it contains mostly ^{3}He. The other phase is called the diluted phase and will always contain 6 - 7 % ^{3}He. In a dilution refrigerator the atoms are continuously crossing the phase boundary. The ^{3}He / ^{4}He mix is liquefied in the condenser, which is connected to the ^{3}He-rich phase of the mixing chamber through a pipe with an impedance. In the mixing chamber the ^{3}He atoms migrate across the phase boundary into the ^{4}He-rich phase. At these temperatures the ^{4}He is superfluid and acts like an "inert superfluid background", it contributes to the volume of the liquid but has negligible heat capacity. The ^{3}He atoms need energy in order to cross the phase boundary thus resulting in cooling of the surrounding system. After the mixing chamber the ^{3}He is pumped away from the mixing chamber and into pipes that lead to the still where the liquid ^{3}He evaporates. Outside the refrigerator, this gas is pumped up to a higher pressure and returned to the condenser to start the cycle again.
The mixing chamber, which is placed on a Cu plate, is the coldest place in a dilution refrigerator and it is to this plate that the setup is connected. This is also were the thermometer which is used to know the sample temperature is placed. The dilution refrigerator used in this experiment was an Oxford Kelvinox 25, with a cooling power of 100 μW at 100 mK, placed at EPFL in Switzerland. [10, 13, 35]

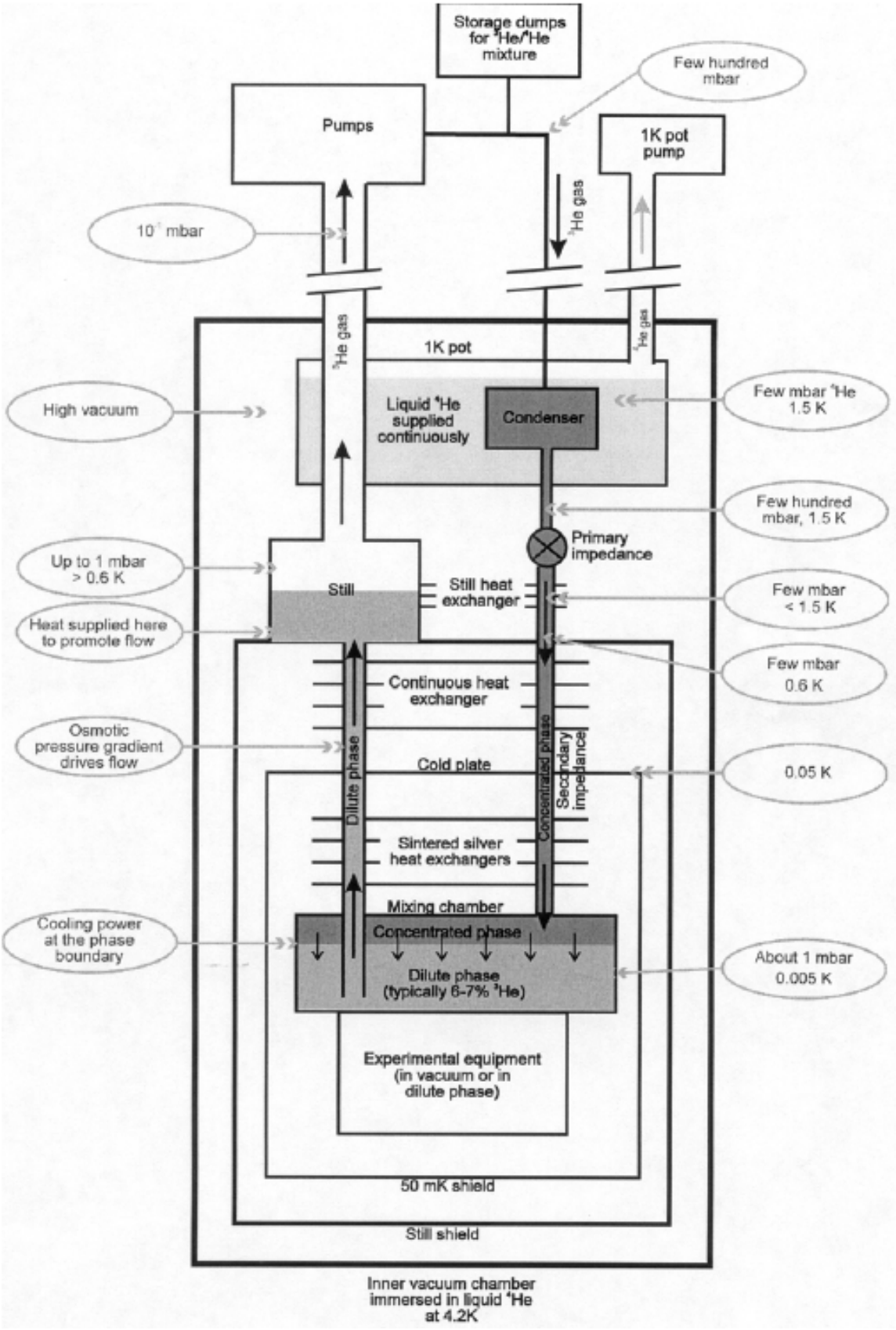

Figure 4.1: Principle of dilution refrigerator, picture taken from [10].

4.1.1 The Magnet

The magnet is a superconducting solenoid placed in liquid ^{4}He. It is run with a maximum current of about 100 A. The windings and the long internal power cables are also superconducting. When the solenoid field has reached the desired value, it is useful to

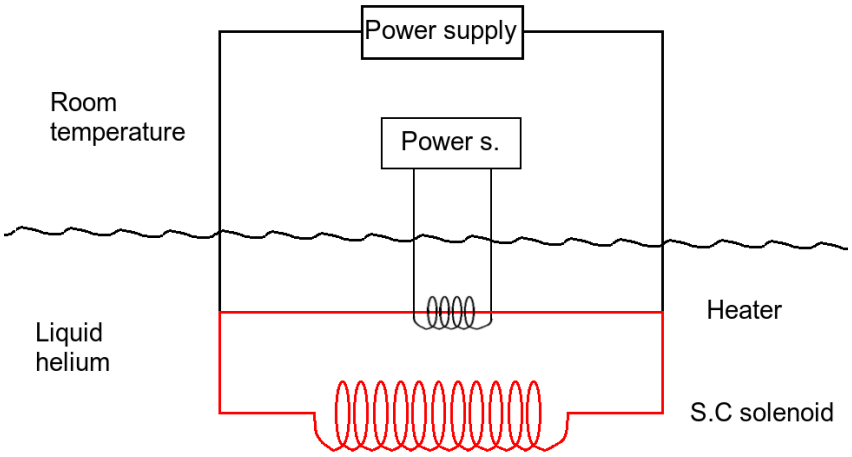

Figure 4.2: Wiring for a superconducting solenoid magnet to be operated in the persistent mode. The red lines indicate the superconducting wire of the magnet.

have the current running in the solenoid without the use of the power supply, see figure 4.2. This is done by connecting the windings with a superconductor wire, thereby the windings become a closed superconducting loop. The power supply can now be turned off, and the persistent currents can flow for months. If one wishes to change the field the heating element on the wire in the He bath can be turned on. The current now runs on the wires out of the He bath, thereby making it possible to change the current and thus the magnetic field. The heating element can again be turned off and the long wire is once again superconducting. The power supply can be switched off and the current will move around in the loop. [35, 43]

Chapter 5

Experimental Setup and Calibration

This chapter describes the construction of the setup. It contains the test setups and calibration. The idea was to build a setup that made it possible to measure the magnetization $\boldsymbol{m}$ of $LiHoF_4$ at low temperatures.

5.1 Introduction to Torque Magnetometer

The magnetization is measured indirectly as the torque $\boldsymbol{\tau}$ is the quantity measured

$$\boldsymbol{\tau} = \boldsymbol{r} \times \boldsymbol{F} \tag{5.1}$$

where $\boldsymbol{r}$ is the displacement vector, along the cantilever. The torque, magnetization and magnetic field $\boldsymbol{H}$ have the following relation

$$\boldsymbol{\tau} = \boldsymbol{m} \times \boldsymbol{H}. \tag{5.2}$$

The experiments are to be performed in a dilution refrigerator, therefore Cu was used as

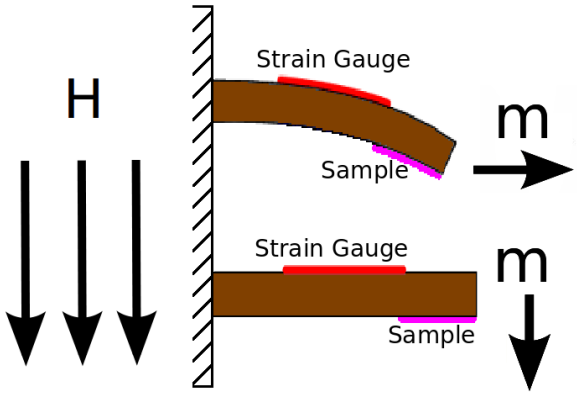

Figure 5.1: The setup idea, the top picture illustrates the regime below the critical field H_C and the lower illustrates the high field regime where the spins have aligned in the direction of the magnetic field.

it has a very high thermal conductivity at low temperatures. The experimental setup is

therefore made of copper whenever possible. In order to reduce heat load at the crystals, the Wheatstone bridges are moved away from the cantilevers. The samples and the Wheatstone bridges are connected by Cu wires. The wires from the four cantilevers are thermally connected to the Cu plate by using GE vanish.

5.2 Cantilever with Strain Gauge

The cantilever was made of a flat piece of copper with a size of approximately 30 times 5 mm and a thickness of 0.50 mm, figure 5.22 shows a cantilever with a strain gauge. An industrial manufactured strain gauge, as described below, was glued with GE varnish on one side of the cantilever. GE vanish is a thermally conductive varnish which can be used as glue for low temperature applications. One of GE varnish's strength is that it does not de-gas significantly in vacuum [16]. The $LiHoF_4$ sample was placed on the opposite side of the cantilever using GE varnish.

5.2.1 Strain Gauge

A strain gauge is designed to measure a change in strain for a given material, see figure 5.2. As the strain gauge is affected by a stress the geometry of the resistor changes. A

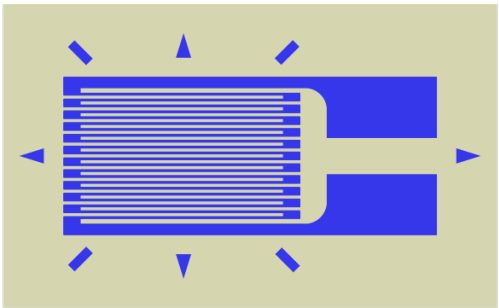

Figure 5.2: Strain gauge [50].

strain gauge has a gauge factor G:

$$\frac{\Delta R}{R} = G\varepsilon + \alpha\Delta T \tag{5.3}$$

which is the relative change in electrical resistance due to the mechanical strain ε and temperature change ΔT. When an electrical conductor is stretched it becomes narrower and longer which will increase its electrical resistance, whereas if it is compressed it becomes shorter and thicker which will decrease the resistance. This resistance change can *e.g.* be measured by a Wheatstone bridge circuit, as described below [35].

5.2.2 Wheatstone Bridge

In order to be able to measure small changes in resistance one can use a Wheatstone bridge. The Wheatstone bridge consists of four resistances which has an external voltage

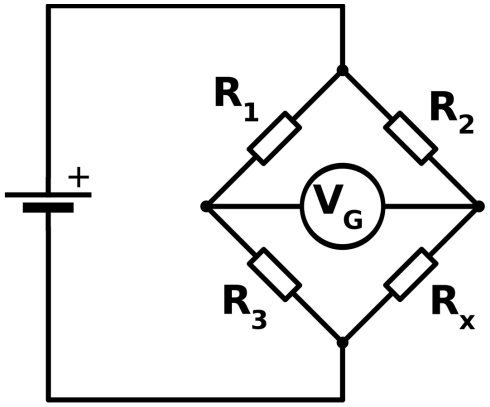

Figure 5.3: Wheatstone bridge, where R_x is the resistance of the strain gauge, picture taken from [50].

applied across the bridge, see figure, 5.3. If the bridge is not balanced there will be an offset, which will decrease the resolution of the setup, this is described in more detail in section 5.2.3. The temperature is assumed to be constant and from equation 5.3 one can see that the change in resistance is proportional to the strain applied to the strain gauge. The strain gauge is connected into a Wheatstone Bridge circuit. In the case of a quarter bridge, as shown in figure 5.3, there is a single strain gauge with the resistance R_x. When the bridge is balanced the resistance of the strain gauge has the nominal value

$$R_x = \frac{R_2 R_3}{R_1}. \tag{5.4}$$

If all the resistors and the excitation voltage V_s are known, one can find the voltage across the bridge V_G, using Kirchhoff's rules

$$V_G = \left(\frac{R_x}{R_3 + R_x} - \frac{R_2}{R_1 + R_2} \right) V_s. \tag{5.5}$$

If the resistance of the strain gauge is assumed to only vary a little bit then R_x can be written as $R_x = R + \Delta R$. In our setup the three other resistors have the same value: $R_1 = R_2 = R_3$, this makes it possible to simplify the expression for V_G

$$V_G = \left(\frac{R + \Delta R}{2R + \Delta R} - \frac{1}{2} \right) V_s \simeq \left(\frac{\frac{\Delta R}{2}}{2(R + \Delta R)} \right) V_s \simeq \frac{1}{4} \Delta R \cdot V_s \tag{5.6}$$

to the first order in ΔR. It is thus clear that the measured signal V_G is proportional to the change in the resistance of the strain gauge. Applying a larger excitation voltage makes it easier to detect the signal, but as the measurements are performed in a dilution refrigerator with a cooling power of 100 μW there is a limit of large a signal can be put into the bridge. We applied a constant current of 10 μA corresponding to an excitation of 3.5 mV. This results in an effect of 70 nW, which is fine for the dilution refrigerator. Detecting a signal with a small excitation voltage is possible by using a lock-in amplifier. We show below that the signal V_G can be measured to high precision by using a lock-in amplifier. In order to have the same field and temperature dependence, and as small an offset as possible, both Wheatstone bridges were constructed of identical strain gauges. A high offset will decrease the resolution of the lock-in amplifier.

5.2.3 Lock-in Amplifier

Lock-in amplifiers are used to detect and measure very small voltage signals - down to a few nV. They make it possible to perform accurate measurements even tough the noise is thousands of times larger than the signal. Lock-in amplifiers use a technique called phase-sensitive detection (PSD) to find the signal component at a specific frequency and phase. The experiment is excited with at a fixed frequency, either provided from the internal oscillator or an external source - in our case the internal oscillator is used. The lock-in amplifier detects the response of the excitation frequency from the experiment at the reference frequency. The noise at frequencies other than the reference frequency ω_{ref} does not affect the measurement.
The measured signal is $V_{sig}\sin(\omega_{sig}t - \theta_{sig})$ where V_{sig} is the signal amplitude. ω_{sig} is the signal frequency, θ_{sig} the signal's phase and t the time. This gives the PSD output of the lock-in by multiplication of the reference signal and the measurement signal

$$\begin{aligned} V_{PSD} =& V_{sig}V_{ref}\sin(\omega_{sig}t - \theta_{sig})\sin(\omega_{ref}t - \theta_{ref}) && (5.7)\\ =& \frac{1}{2}V_{sig}V_{ref}\cos([\omega_{ref} - \omega_{sig}]t + \theta_{sig} - \theta_{ref}) \\ & -\frac{1}{2}V_{sig}V_{ref}\cos([\omega_{ref} + \omega_{sig}]t + \theta_{sig} + \theta_{ref}). && (5.8)\end{aligned}$$

Thus the output signal is two AC signals, one at the difference frequency $\omega_{ref} - \omega_{sig}$ and one at the sum frequency $\omega_{ref} + \omega_{sig}$. If the PSD output is passed through a filter the AC signals can be removed. If $\omega_{ref} = \omega_{sig}$ the difference signal component will be a DC signal, thus the filtered PSD output is

$$V_{PSD} = \frac{1}{2}V_{sig}V_{ref}\cos(\theta_{sig} - \theta_{ref}). \quad (5.9)$$

The PSD signal is proportional to the measurement signal's amplitude.
The lock-in amplifier takes the input signal, multiplies it by the reference signal , and integrates it over a specified time, usually on the order of milliseconds to a few seconds. Therefore the time used to measure should be larger than the period of the signal, which is not a problem with our setup. [45]

5.3 Test Setup

We first discuss the dimensions of the setup. A sample of 1 mm^3 $LiHoF_4$ weighs approximately 9 mg, which is a reasonable minimum size for a sample. The unit cell of $LiHoF_4$ is 288 Å^3. Each cell contains 4 Ho atoms, each with a significant magnetic moment. Trivalent holmium Ho^{3+} has the largest magnetic moment of any naturally occurring element, *i.e.* 10.6 μ_B [6]. A crystal of 1 mm^3 will contain $4 \cdot \frac{(1\cdot 10^{-3})^3}{(288\cdot 10^{-10})^3} = 13.9 \cdot 10^{18}$ holmium atoms. The magnetic moment of the crystal will be $\mu = 13.9 \cdot 10^{18}$ 10.60 $\mu_B = 1.37 \cdot 10^{-3}\frac{Nm}{T}$. The torque near the critical field at 5 T will be $\tau = 2.74 \cdot 10^{-4}$ Nm. The setup was tested at room temperature, in liquid nitrogen and in liquid helium. In order to learn whether or not the cantilevers were able to tolerate the large torque from the sample a test setup was used, as illustrated in figure 5.4. The torque is related

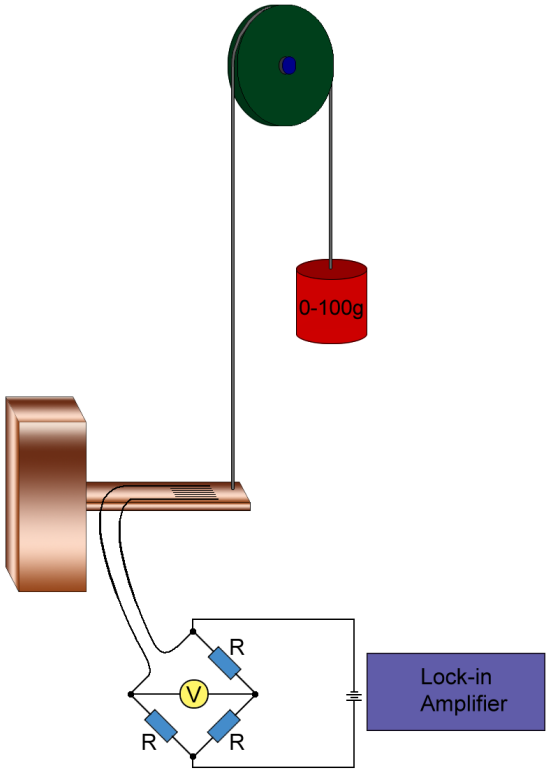

Figure 5.4: The test setup consisting of a cantilever with a strain gauge in a Wheatstone circuit. A weight and pulley is used in order to produce a torque. The change in signal is measured by a lock-in amplifier. The setup was designed in order to investigate the resolution of the system and to calibrate Wheatstone circuit.

with the force and the length of the lever arm through equation (5.1). With $\boldsymbol{F}$ and $\boldsymbol{r}$ perpendicular, we have : $F = \frac{\tau}{r} = m \cdot g$ where $r = 17$ mm and $g = 9.8\ \frac{\mathrm{m}}{\mathrm{s}^2}$ is the gravitational acceleration. This means a $LiHoF_4$ crystal of 1 mm^3 will correspond to a weight of approximately 9 g. With this in mind the test setup could be started. A weight corresponding to the torque of the sample and a pulley was used. In figure 5.6 the voltage output can be seen for different weights from 0 to 100 g along with a linear fit. The error bars are the standard deviation of the mean, as will be discussed in the following chapter in section 6.1.1. The signal as a function of different weights looks very linear up until 60 g and fits rather nicely to a straight line as can be seen in figure 5.6, where the last two points have been omitted. The fit has the form

$$\tau = (-0.0550 \pm 0.00088) \cdot m\frac{\mathrm{V}}{\mathrm{g}} + (3.25 \pm 0.023)\mathrm{V}. \tag{5.10}$$

Within a reasonable regime the signal is linear and the setup can measure the signal corresponding to the torque signal from the sample. With a weight larger than about 60 g the signal no longer seems to be linear . This corresponds with equation (5.6) where we learned that the measured signal is only proportional to the change in resistance when the change in resistance ΔR is not too large. This is not a problem for the setup since we have estimated the torque from the sample to correspond to about 9 g of mass. As

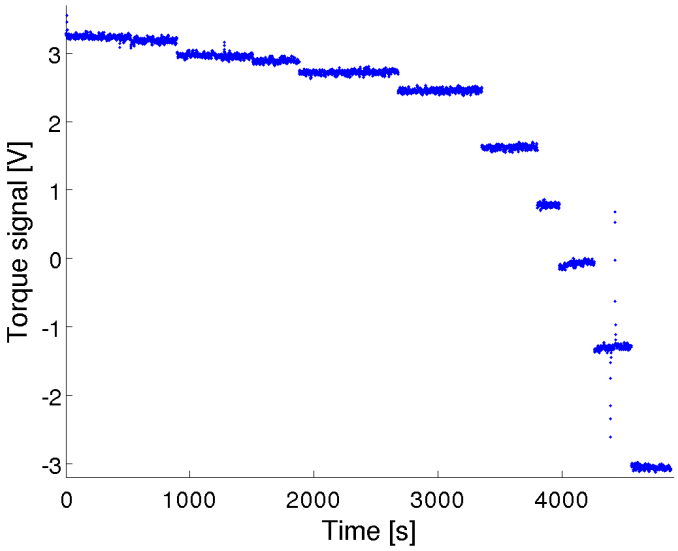

Figure 5.5: The strain measured as a voltage for different weights at room temperature, with an excitation voltage of $V_s = 10\,\mathrm{mV}$. As time goes the weights are changed from 0 g to 1.4 g, 4.6 g, 5 g, 6.4 g, 10 g, 15 g, 30 g, 45 g, 60 g, 80 g and 100g. The signal is constant in time, thus no deformation of the cantilever seems to be present.

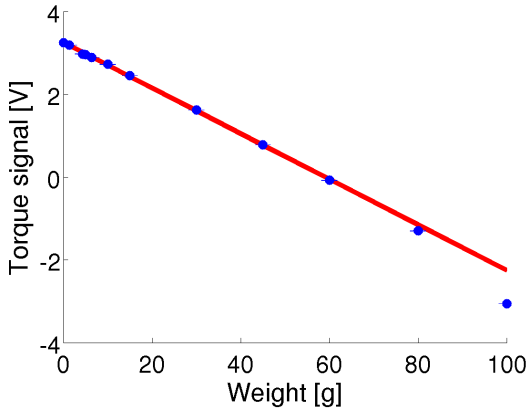

Figure 5.6: The strain measured as a voltage for different weights at room temperature. The signal from figure 5.5 has been averaged in order to get the single points represented here. These point are fitted to the straight (blue) line.

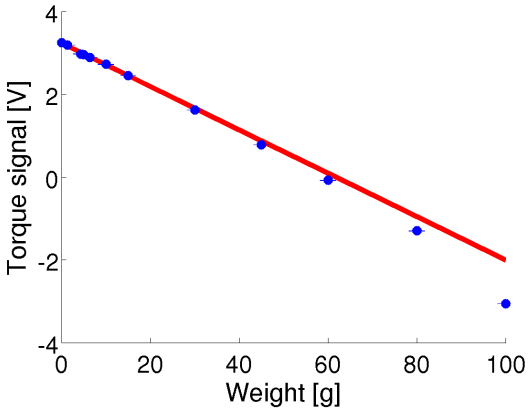

Figure 5.7: The strain measured as a voltage for different weights at room temperature. Here only the first seven points, up to 15 g, have been fitted to a straight line.

the signal looks more linear in the regime with smaller weights, a fit for the first seven point, *i.e.* up to 15 g, has also been fitted. This results in the fit

$$\tau = (-0.0524 \pm 0.0041) \cdot m\frac{\mathrm{V}}{\mathrm{g}} + (3.23 \pm 0.032)\mathrm{V}. \tag{5.11}$$

Omitting points in the non-linear regime does not result in a better fit, but maybe one could fit these data to another function if one needed information on the behaviour of the setup for large torques/weights. As this is not necessary in this setup it will not be done. On this basis it was concluded that using the copper cantilevers with strain gauges in a Wheatstone bridge would make it possible to measure the magnetization of $LiHoF_4$ and that the signal would be proportional to the torque in the desired regime.

5.4 Building the Setup

The original idea was to measure on four cantilevers at the same time, by the use of four lock-in amplifiers. The Wheatstone circuit was first built as to minimize the amount of resistors, thereby minimizing the heat input into the dilution fridge. Two resistors were re-used in all four circuits, making it possible to have four cantilevers with strain gauges by the use of totally ten resistors in stead of sixteen. The original idea was to only use

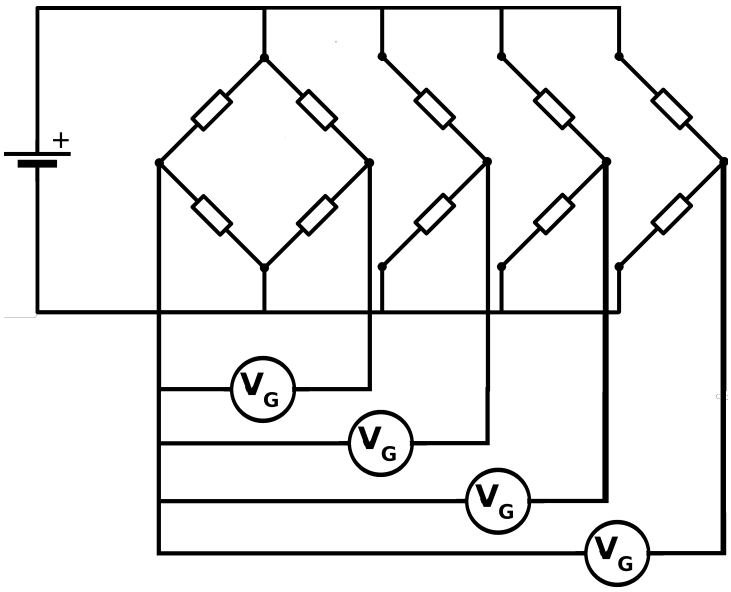

Figure 5.8: A circuit enabling measurements of four cantilevers simultaneously. Two of the resistors - the two to the left, have been reused in order to minimize heat input into the cryostat.

strain gauges on the cantilevers and ordinary ceramic resistors elsewhere. This caused some problems balancing the circuit. The different resistors of nominally 120 Ω, varied from 122.6 Ω to 123.5 Ω. The strain gauges and the resistors reacted differently when cooled down. The strain gauges changed from 122.0 Ω at room temperature to 119.9 Ω at 77 K where one of the resistors changed from 121.5 Ω to 120.6 Ω. Having different resistances in the Wheatstone circuit resulted in a rather large offset, and this would make the desired resolution unattainable, see equation 5.5.

In order to solve this problem a potentiometer was connected parallel with resistor R_1. The resistors corresponding to the position of resistor R_2 were also exchanged with dummy strain gauges. These strain gauges were not used to measure but were purely used as resistors. The idea was that they would change in the same way as the strain gauges

Figure 5.9: The setup with four cantilevers and dummy strain gauges as resistors. To the left one can see the four blue potentiometers, next to them are the four dummy strain gauges glued on an little copper plate. To the right the four cantilevers with strain gauges and - on some of them samples - are placed.

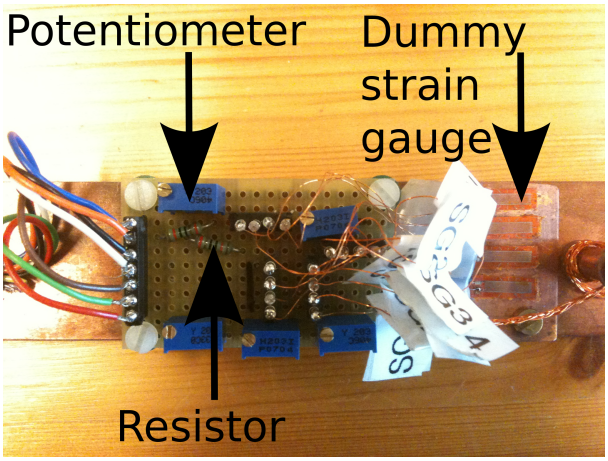

Figure 5.10: A zoom of the setup showing the potentiometer, dummy strain gauges and ordinary resistors.

which was used to measure the torque, thereby resulting in a small offset even at different temperatures. Unfortunately the offset was still too large to enable the desired resolution. Applying four potentiometers, one to each of the dummy strain gauges, made it possible to use the potentiometer, at resistor R_1, as a master tuner and the potentiometers at the four dummy strain gauges could be used to fine-tune the individual strain gauges. A photo of this setup is shown in figure 5.9. The cantilevers are in such a way that they should all be within the homogeneity of the magnetic field. To test whether the setup would work in a dilution refrigerator it was first tested in a He container. The setup showed suitable offsets for this temperatures regime. With this in mind one could hope that the offsets would remain constant for temperatures below 4 K. This idea of setup was later rejected when it became necessary to perform the measurements at EPFL. Here there was only access to one lock-in amplifier as opposed to the four lock-in amplifiers used in this method of setup. The setup was then changed to consist of two individual Wheatstone bridges where the resistors were all dummy strain gauges. This resulted in a very small offset of about 20 µV with an excitation voltage of $V_G = 20$ mV. The final setup is described in section 5.5.5, and is shown in figure 5.22.

5.5 Calibration of Strain Gauges

5.5.1 Calibration of copper-nickel alloy Strain Gauges alone

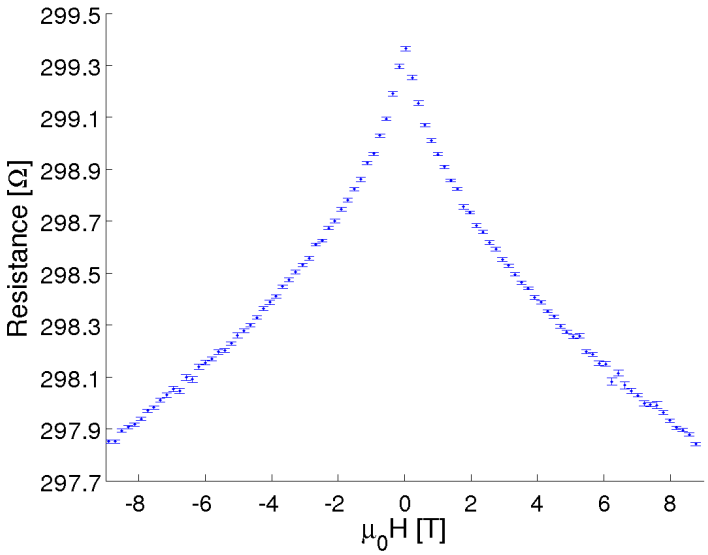

Figure 5.11: The change of the resistance of a single Cu-Ni strain gauge as a function of magnetic field from -9 to 9 T at about 50 mK. Every 50 points have been averaged to one and the standard deviation of the mean been used as error bars.

The first setup was made with strain gauges that consisted of a copper-nickel alloy - this material is also known as constantan, usually consisting of 55 % copper and 45 % nickel. The advantage of constantan is that the resistivity ρ is constant over a wide temperature range. Performing a 2-point measurement on the single Cu-Ni strain gauge, enabled determination of the field and temperature dependence of its resistance. A current of 0.100 μA was applied to the strain gauge which had a resistance of 120 Ω at room temperature and zero magnetic field. The voltage signal V_G was measured with a lock-in amplifier in order to achieve a good resolution. Figure 5.11 shows the field dependence of the resistance of a strain gauge. As it is only a two point measurement the resistance of the wires must also be considered. A resistance of about 300 Ω thus seems reasonable. It is clear that a large magnetoresistance is present. The strain gauge changes with 1.7 Ω from zero field to ± 9 T, corresponding to 1.5 % of the 120 Ω resistance. As we shall see in section 5.5.3 there is no magnetoresistance of the Cu wires.

5.5.2 Calibration of copper-nickel alloy strain gauges in a Wheatstone circuit

Four cantilevers, with constantan strain gauges, placed in Wheatstone bridges were all measured in a dilution refrigerator. Three of the cantilevers had a long thin sample of $LiHoF_4$ mounted, and the last cantilever did not have a sample. Figure 5.12 shows a field scan of the cantilever without the sample, while figures 5.13, 5.14 and 5.15 shows field scans of the cantilevers with samples. The cantilever SG1 in figure 5.15 for some reason

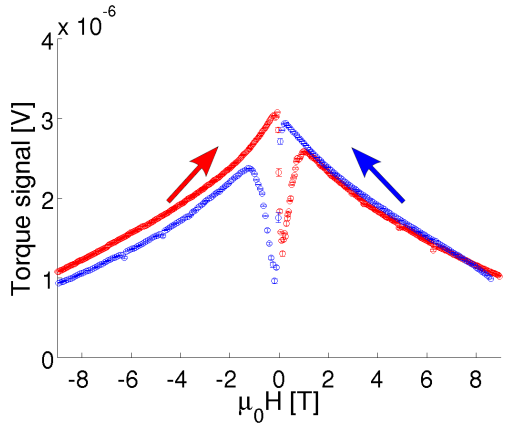

Figure 5.12: Field scan of Cu-Ni strain gauge setup (NSG) without a sample of $LiHoF_4$. Every 20 points have been averaged and the standard deviation of the mean used as error bar. The arrows point in the direction of the change in magnetic field, *i.e.* red increasing and blue decreasing.

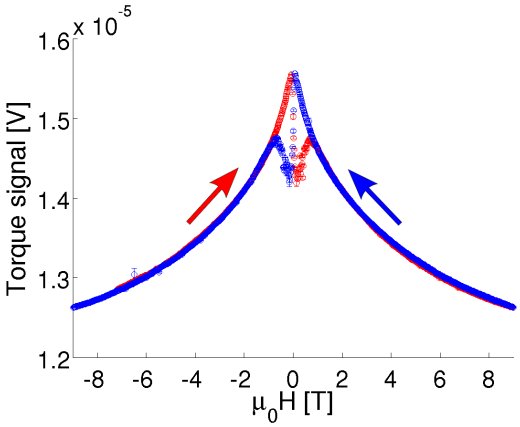

Figure 5.13: Field scan of Cu-Ni strain gauge setup (SG2) with $LiHoF_4$. Every 20 points have been averaged and the standard deviation of the mean used as error bars.

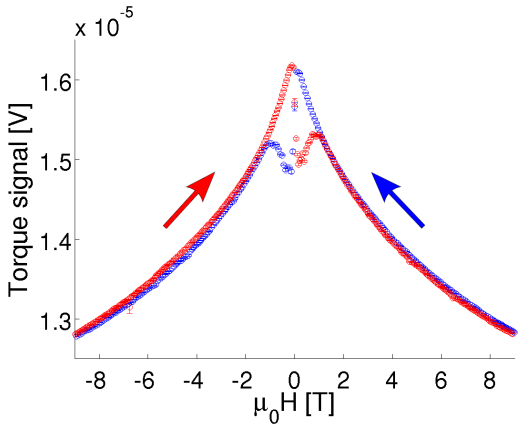

Figure 5.14: Field scan of Cu-Ni strain gauge setup (SG3) with $LiHoF_4$. Every 20 points have been averaged and the standard deviation of the mean used as error bars.

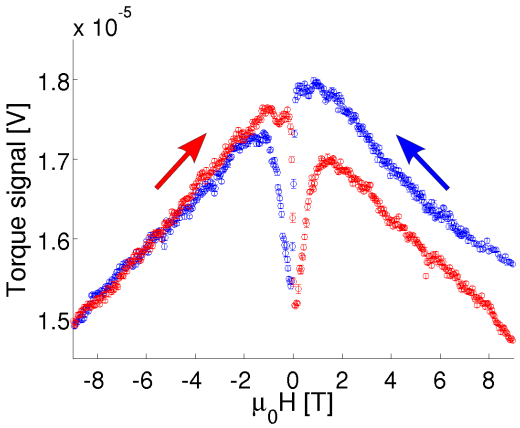

Figure 5.15: Field scan of Cu-Ni strain gauge setup (SG1) with $LiHoF_4$. Every 20 points have been averaged and the standard deviation of the mean used as error bars. This setup had considerable more noise.

had considerable more noise, this could be due to a bad connection. Unfortunately the behaviour of the samples with and without sample look similar. This must be because the behaviour seen is due to the setup and not the sample. The field response of the $LiHoF_4$ sample must still be present, but it is presumably much smaller than the field dependence of the Cu-Ni alloy in a Wheatstone bridge. It is interesting that the Cu-Ni strain gauges behave differently in the Wheatstone bridge than alone. Maybe the bridge

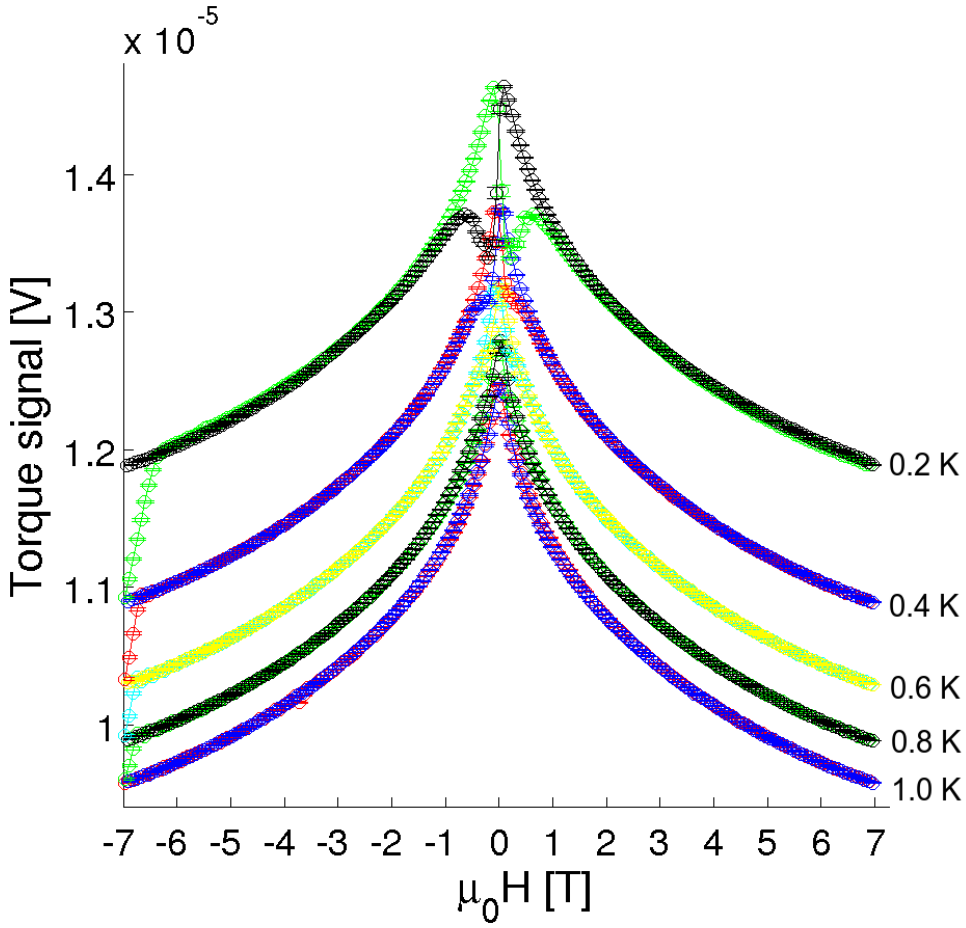

Figure 5.16: Field scan of the same cantilever (SG2) as in figure 5.13 at different temperatures. Increasing fields : red, green and cyan. Decreasing fields : blue, black and yellow. Below 0.4 K there is a significantly difference between going up and down in field around ±1 T.

somehow amplify the signal, or it could be due to the fact that the strain gauges in a bridge are placed differently with respect to the magnetic field, both in direction and in distance, as can be seen on the setup photo in figure 5.9. Figure 5.16 shows data on the SG2 cantilever (also with sample) as in figure 5.13 but at different temperatures. Below ±1 T there is a large difference in the signal depending on whether the magnetic field is increasing or decreasing. Figure 5.17 shows also field scans of the same cantilever as in figure 5.13 at different temperatures: 1 K, 0.6 K, 0.4 K and 0.2 K. Below 0.4 K one can see a significant difference between the increasing and decreasing field around ±1 T. One could think that this hysteresis is due to $LiHoF_4$, but since the cantilevers without a sample also display a hysteresis, this is not the case. This behaviour of the Cu-Ni strain gauges in Wheatstone bridges have similarities to that of a spin glass. Nickel is ferromagnetic at room temperature and copper is not, in this way Cu only works as a diluter.

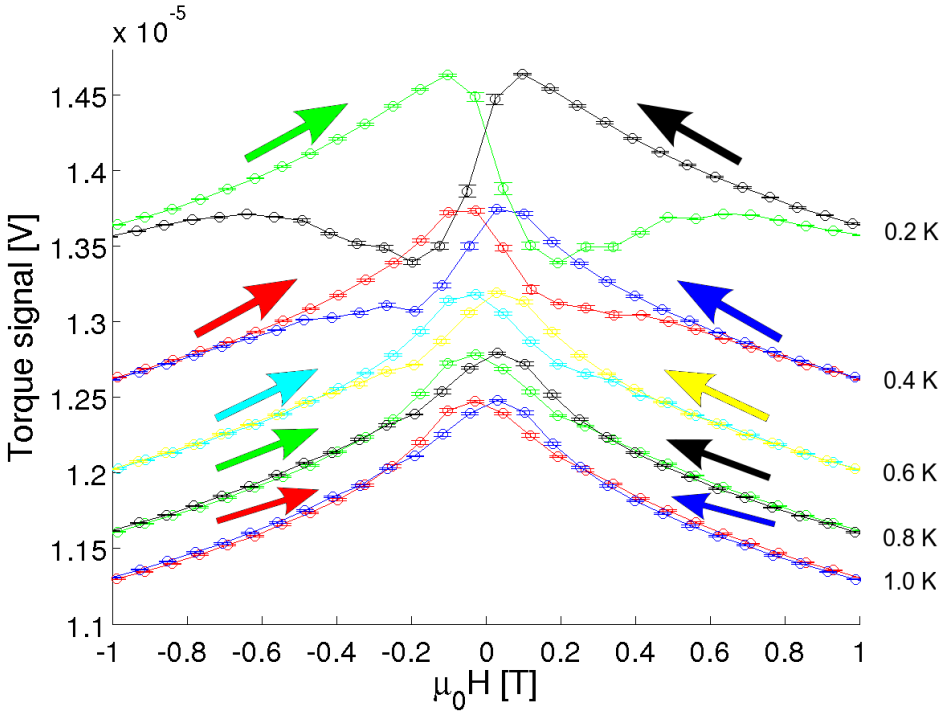

Figure 5.17: Zoom of figure 5.16, field scan of SG2 at different temperatures.

5.5.3 Measurements of platinum-tungsten alloy strain gauges alone

To solve the problem with the rather large magnetoresistance in the Cu-Ni strain gauges a new set, made of a Pt-W, were purchased. They have a resistance at room temperature and zero field of 350 Ω. Strain gauges made of platinum and tungsten have previously been tested at room temperature, 4 and 77 K by Bower [7] with a magnetic field up to 1 T. Bower in his article found that the resistance changed from 350.2 Ω at room temperature to 328.9 Ω at 77 K and 324.8 Ω at 4 K. The magnetoresistance was very small at all temperatures. This led us to think that Pt-W strain gauges could be used in the setup. Strain gauges from Vishay [48], made of platinum and tungsten, were tested in liquid helium from -2 to 2 T. To achieve a constant current, a voltage of 1 V was send through a resistor of 100 kΩ, thus resulting in a current of 10 μA. In order to learn whether the Pt-W strain gauge would show magnetoresistance a four-point measurement was conducted while the external magnetic field was varied. The current was applied to the strain gauge, which had a resistance of 350 Ω at room temperature and zero field. Figure 5.18 shows a field scan from 9 to -4 T at temperatures around 60 - 80 mK. The steps or jumps in resistance is caused by the discrete resolution of the ADC (analog-to-digital converter). The lock-in amplifier is analog and therefore would show a continuous noise. Each of the jumps are 10 mΩ corresponding to a voltage of 100 nV. At low temperatures the resistance has dropped to around 226 Ω but does not seem to change as a function of field. This is in agreement with Bower's [7] measurement of very similar strain gauges.

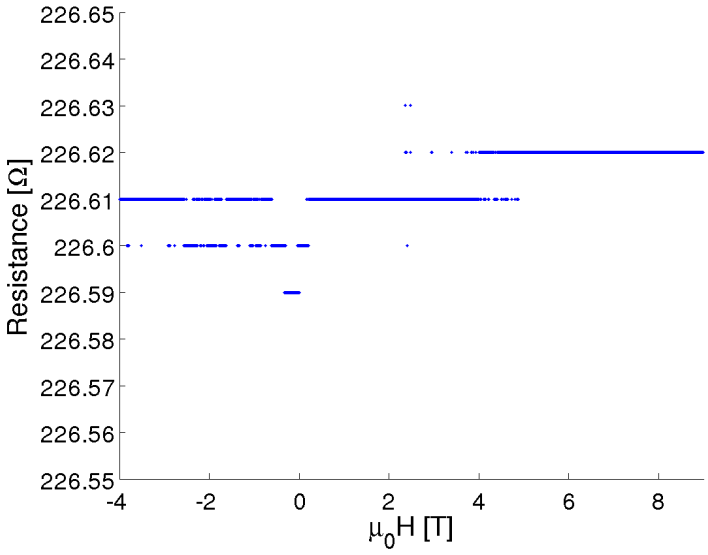

Figure 5.18: Raw data of the field scan of the Pt-W strain gauge alone at approximately 80 mK.

5.5.4 Measurements of platinum-tungsten alloy strain gauges in a Wheatstone circuit

The strain gauges were also tested in a Wheatstone circuit. The measurements were performed at both 65 mK and 2 K and can be seen in figure 5.19. The resistances for the two different temperatures have the same field dependence, therefore it is concluded that there is no temperature dependence in the desired regime. The resistance has been measured both when increasing and decreasing magnetic field and there is no difference. In figure 5.20 the circuit is measured at respectively 0 T and 9 T. The temperature is changed from base temperature to about 3.5 K. This plot shows how the resistance fluctuate, as opposed to the plot of the single strain gauge in figure 5.18 the circuit is balanced, which makes it possible to see smaller fluctuations. One can see the noise is of the order 10 nV, which is a tenth of the noise from before (strain gauge alone). As already seen in figure 5.19 the resistance shows a field dependence, but the temperature scans in figure 5.19 indicate that it does not depend upon temperature. Therefore it was concluded that these Pt-W strain gauges could be used as a part of the setup in a dilution refrigerator. Section 6.1 will show that the field dependence is relatively easy to fit, thereby enabling a subtraction of the field dependence from the actual measurements.

5.5.5 The Final Setup

Figure 5.22 shows a cantilever with a Pt-W strain gauge. The left part of figure 5.23 shows one of the two cantilevers with the Pt-W strain gauge mounted on the setup. One of the cantilevers has a sample mounted and the other does not. To the right the figure shows the six dummy strain gauges, and a Cu rod which is used to thermally connect the wires.

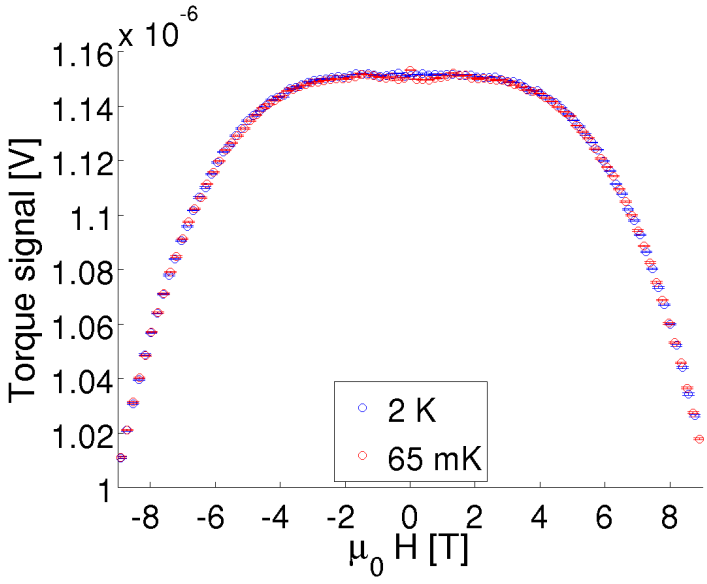

Figure 5.19: Field scan of the Wheatstone circuit without sample from -9 to 9 T at 65 mK (blue) and 2 K (red).

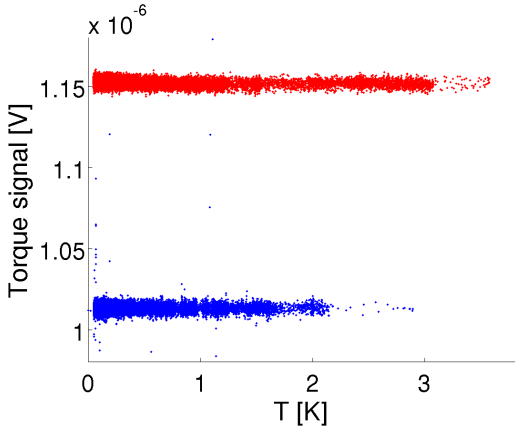

Figure 5.20: Temperature scan of the Wheatstone circuit without sample from 50 mK to 3.5 K at 9 T (blue) and 0 T (red).

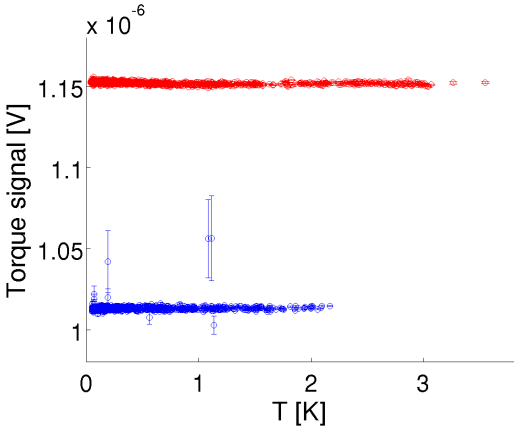

Figure 5.21: Temperature scan of the Wheatstone circuit without sample from 50 mK to 3.5 K at 9 T (blue) and 0 T (red). Every 20 points have been averaged and the standard deviation of the mean used as error bars.

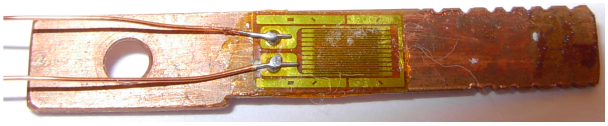

Figure 5.22: The Cu cantilever with a Pt-W strain gauge, the sample is mounted on the opposite side at the end of the cantilever. The hole is for mounting of the cantilever.

Figure 5.23: The final setup. To the left the cantilever with strain gauge, to the right the six dummy strain gauges needed in order to have two cantilevers with two Wheatstone circuits.

5.6 Aligning the Crystal

In order to cut the crystal in the c axis' direction, it was necessary to align the crystal with X-rays. The measurements were performed using the Laue backscattering technique at Risø-DTU. A broad spectrum of X-rays hit the sample and are scattered from the crystal whenever Bragg's law

$$n\lambda = 2d\sin(\theta) \tag{5.12}$$

is fulfilled.
The technique is shown in figure 5.24, but in transmission mode instead of backscattering as used in the setup at Risø-DTU [1]. As shown in the Laue picture in figure 5.25 the

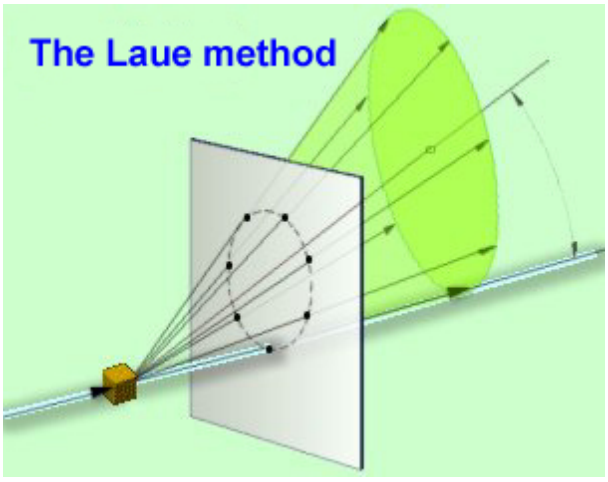

Figure 5.24: The Laue method in transmission mode, scattered X-rays from a broad spectrum source are recorded, figure taken from [44]

c-axis points vertically upwards and is tilted a few degrees out of the plane, causing the small displacement between the central black and white point. The c-axis was found to be along the edge of the crystal.
After finishing the measurements at EPFL the setup alignment was checked with a Laue camera at EPFL, the sample showed to be 4°of.

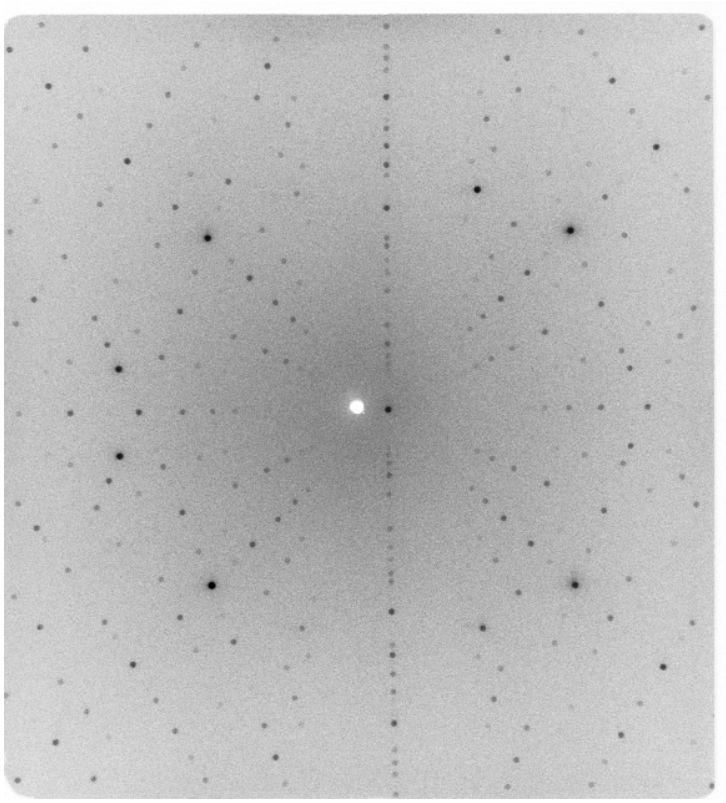

Figure 5.25: A diffraction pattern of $LiHoF_4$ obtained by the Laue backscattering technique. The c-axis is vertical.

Chapter 6

Results

All the measurements were performed at Ecole Polytechnique Fédérale de Lausanne (EPFL) in the group of, Laboratory for Quantum Magnetism. The measurements were performed at an Oxford dilution refrigerator. The base temperature was about 45 mK, but obtaining 30 mK should be possible if one waited longer. The magnetic field was varied from -9 to 9 T using a superconducting solenoid.

6.1 Background Signal - Cantilever without $LiHoF_4$

The setup without sample consisted of two Wheatstone bridges each with a copper cantilever, one with a $LiHoF_4$ sample placed on the cantilever and one without. To make sure that the measurements showed the behaviour of the sample and not the setup, measurements were performed with both cantilevers.

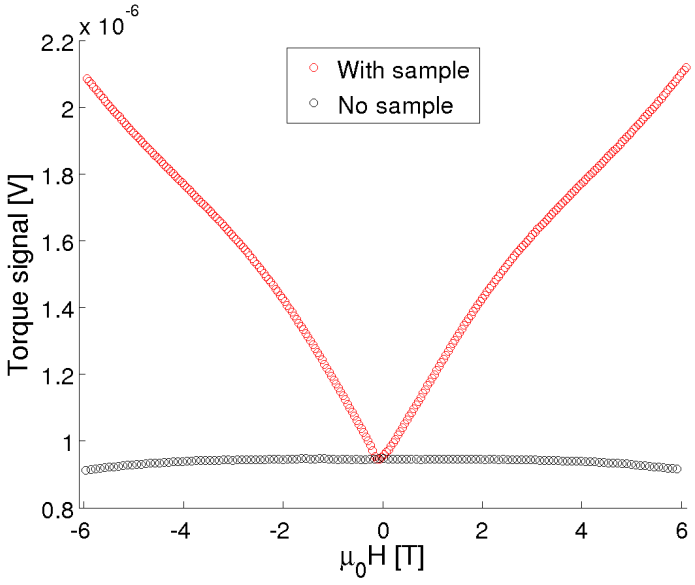

Figure 6.1: Data showing the voltage over the Wheatstone bridge as a function of field, both for the sample (red) and the background (black) at 50 mK.

6.1.1 Field Dependence

The setup shows some field dependence, the effect grows significantly above ∼4 T. But as can be seen in figure 6.1 the effect is still significantly smaller than the effect of the sample. The sample responds much more strongly to the changing field than the cantilever alone. This is reassuring as this means the setup can actually be used to measure the magnetization of the sample.
Figure 6.2 shows field scans of the setup without sample at 65 mK and 2 K. Every 100 points have been averaged, out of totally 16150 data points for the sample and 6500 data points without the sample. The standard deviation of the mean

$$\sigma_{mean} = \frac{\sigma_x}{\sqrt{N}} = \frac{1}{\sqrt{N}}\sqrt{\frac{1}{N}\Sigma_{i=1}^{N}(x_i - \overline{x})^2} \tag{6.1}$$

has been used as error bars, where σ_x is the standard deviation and $\overline{x} = \frac{x_1+x_2+\cdots+x_N}{N}$ is the best estimate of x [46]. In the formula for the standard deviation, σ_x, one often uses $N-1$ instead of N, but which one is used makes no difference as N is a relatively large number. The difference between 65 mK and 2 K is of the order $1 \cdot 10^{-9}$ V whereas

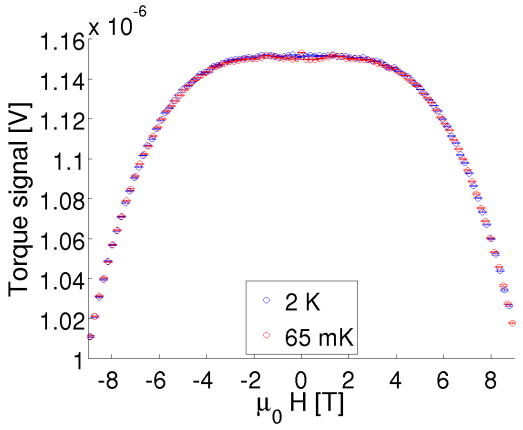

Figure 6.2: Field scan of the cantilever without sample from -9 to 9 T at 65 mK (red) and 2 K (blue). The data show only minor difference between the two temperatures. Every 50 points have been averaged.

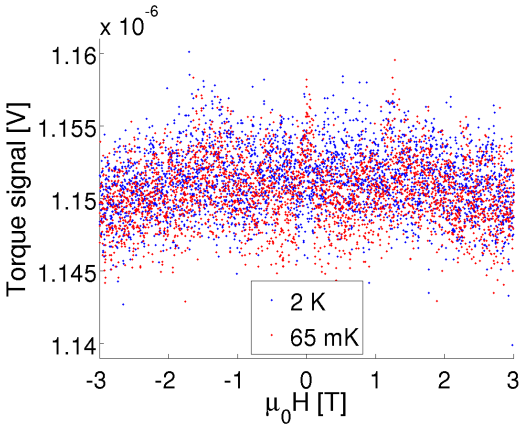

Figure 6.3: Zoom of the raw data of the field scan of the cantilever without sample from -9 to 9 T at 65 mK (red) and 2 K (blue).

the signal is of the order $1 \cdot 10^{-7}$ V . As the temperature influence on the background is small compared to the field influence the temperature dependence has been ignored. As there is no significant difference between the two data sets they have been combined, in order to gain data points. This results in one background data set, illustrated in figure 6.4 along with a fit. A constant has been subtracted in order to have zero signal at zero field. The background data from these field scans fit well to a 4th order polynomial. Performing a polynomial fit in Matlab results in the following expression

$$\begin{aligned} &-19.0 \pm 0.1 \cdot 10^{-12} \cdot H^4 + 4.89 \pm 0.48 \cdot 10^{-12} \cdot H^3 \\ &-249 \pm 7.7 \cdot 10^{-12} \cdot H^2 - 31.7 \pm 25.5 \cdot 10^{-12} \cdot H. \end{aligned} \tag{6.2}$$

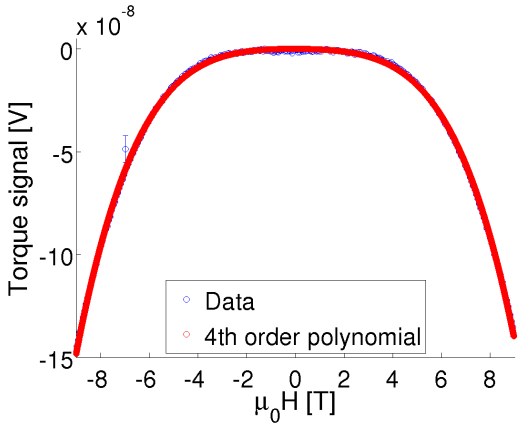

Figure 6.4: Field scan of the cantilever without sample from -9 to 9 T (blue). This will be used as background, and fits nicely to a 4th order polynomial (red).

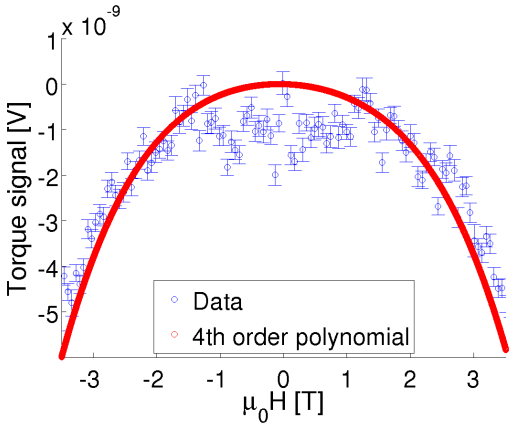

Figure 6.5: Zoom of figure 6.4, field scan of the cantilever without sample from -9 to 9 T (blue) and a 4th order polynomial (red).

When processing the data, we want to obtain the magnetization *i.e.*, $\boldsymbol{m} = \frac{\tau}{H}$, as seen in equation (5.2). Therefore the measured signal - and thus also the background corrections - will be divided by the field in order to get the magnetization. Around zero field where the signal is divided by very small fields, the noise in the data diverge due to the $frac1H$ factor. From the plot of the torque signal in figure 6.4 it is clear that the points lie close to

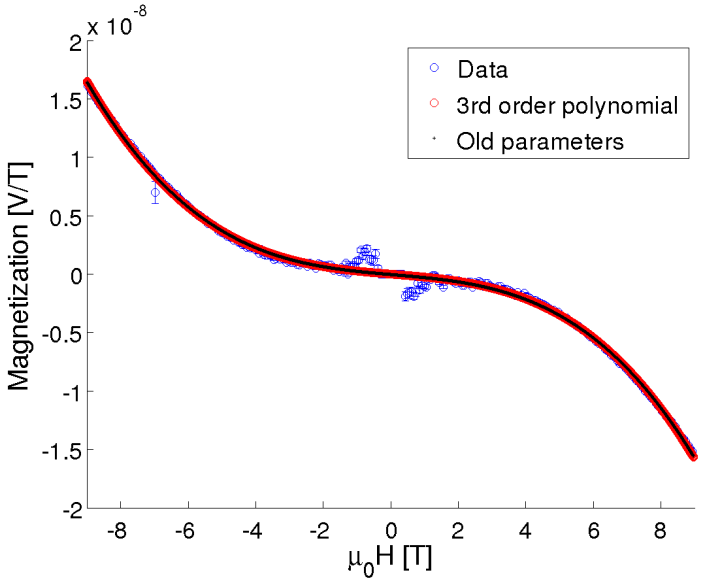

Figure 6.6: Torque signal divided by H (blue) and a 3rd order polynomial fit (red). The torque signal has been manually set to zero at $\pm$ 0.5 T to avoid the points from blowing up. The black curve is the 3rd order polynomial with the parameters from the 4th order fit.

each other and do not suddenly change, therefore the torque signal has been manually set

to zero at $\pm$ 0.5 T to avoid the problem of points blowing up. The fit has the expression

$$\begin{aligned} &-19.2 \pm 0.14 \cdot 10^{-12} \cdot H^3 - 4.21 \pm 0.63 \cdot 10^{-12} \cdot H^2 \\ &-238 \pm 7.3 \cdot 10^{-12} \cdot H + 1.47 \pm 19.6. \end{aligned} \tag{6.3}$$

which is in agreement with the fourth order polynomial, except for the constant which is very uncertain. Figure 6.6 shows the magnetization background fitted to a 3rd order polynomial, both with the data (blue), the new fitting parameters (red) and parameters from the "old" fit (black) from the fourth order polynomial. The new an old parameters are clearly in fine agreement.

6.1.2 Temperature Dependence

The temperature dependence of the setup is also important as both field and temperature sweeps have been performed. Figure 6.7 and 6.8 show the torque signal from the empty cantilever as the temperature varies from 50 mK to 2-3 K at respectively 0 and 9 T. The

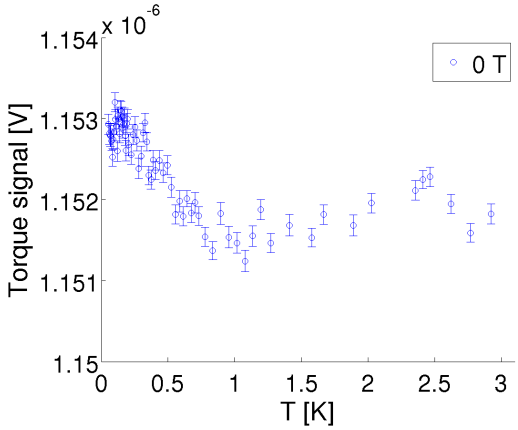

Figure 6.7: Torque signal from the empty cantilever, as the temperature has been varied from 50 mK to 3 K at zero field. Every 300 points have been averaged to one point.

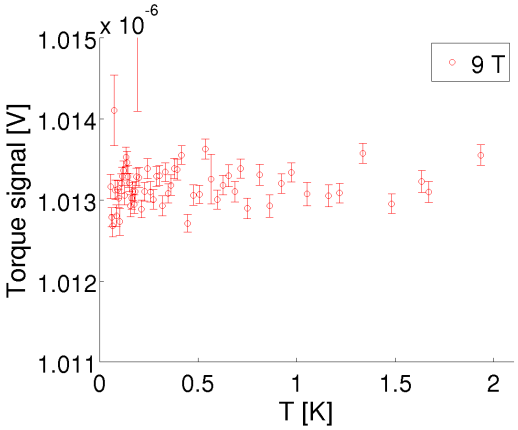

Figure 6.8: Torque signal from the empty cantilever, as the temperature has been varied from 50 mK to 2 K at 9 T. Every 300 points have been averaged to one point.

torque signal at 9 T is constant as a function of magnetic field. The data at zero field show a deviation of the order $1 \cdot 10^{-9}$ V.

6.1.3 Conclusion on Background

The setup shows a negligible temperature dependence, but has some field dependence. The temperature scans are therefore assumed to only contain information about the behaviour of the sample and not the setup. On the basis of the field scan made without the sample, the field scans with the sample contain both information on the setup and the sample. The data without the sample are therefore regarded as background and will be subtracted from all the field scans.

6.2 Signal from the $LiHoF_4$ Sample

We now turn to the measurements of the $LiHoF_4$ sample. A current of 10 μA was applied to the Pt-W strain gauge which has a resistance of 350 Ω at room temperature and zero field. All the conducted measurements can be seen in table A.1.1, a list of the data without the sample can be seen in table A.2.1.

6.2.1 Measurements of Strain Gauge with $LiHoF_4$ Sample

Field Dependence

Looking at the torque data, for example at 100 mK, as in figure 6.10, it has sort of a s-shape on each side of zero field. As we saw in figure 6.6 the setup shows field dependence after approximately 2 T. In section 6.1 the cantilever without $LiHoF_4$ was measured and subtracted as background from the measurements with sample. The Wheatstone circuit used with the sample and the Wheatstone circuit used as background were balanced differently, *i.e.* they had different offset. Therefore the background data could not just be subtracted, but it was necessary to use a scaling factor. The magnetization of a ferromagnet is expected to reach a maximum when all the moments are aligned with the applied field [6]. This is verified by the mean-field, where the magnetization saturates at 5-6 T, as will be shown in section 7.2.1. This could be used to find the scaling factor for the background. A temperature of 1 K, which is well below T_c, was chosen to find the scaling factor. This resulted in a factor of 2 which seems reasonable. The result

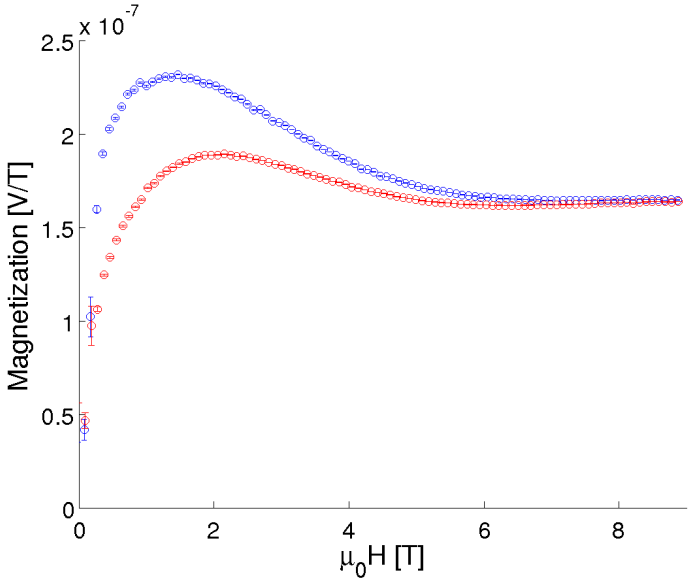

Figure 6.9: The magnetization at $T_c = 1.53$ K (red) and 1 K (blue). Both of them become straight at higher fields.

is illustrated in figure 6.9 where the magnetization for 1.53 K (red) and 1 K (blue) are illustrated as a function of positive magnetic fields.

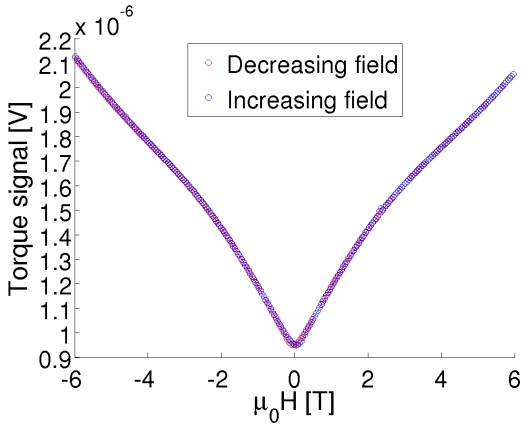

Figure 6.10: Field scan with sample from -6 to 6 T (blue) and 6 to -6 T (red) at 100 mK. Every 50 points have been averaged to one point.

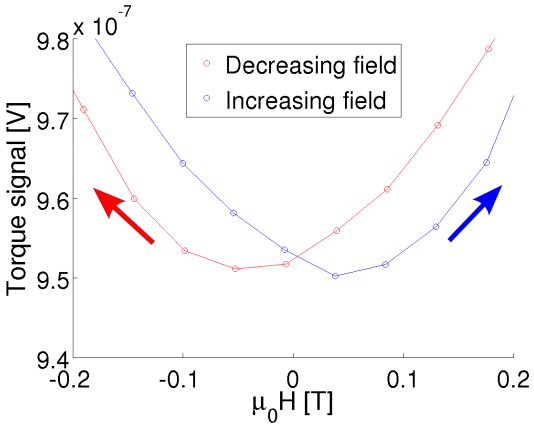

Figure 6.11: Zoom of previous figure in the zero-field region. One can see a displacement around zero field.

6.2.2 How to obtain the Magnetization Curve

The measured signal can be written as $U - U_0$, where U_0 is the minimum torque signal. The data from the measurements are plotted in order to find the minimum signal U_0.

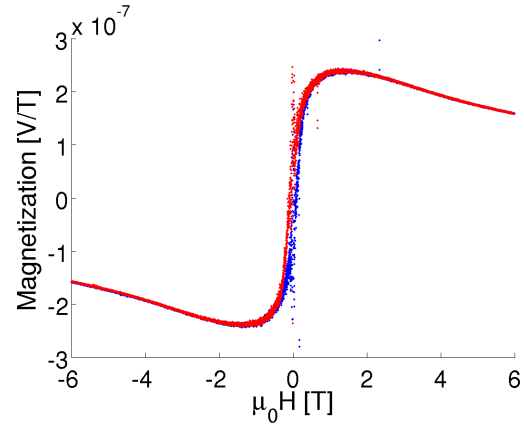

Figure 6.12: Data of the magnetization of $LiHoF_4$ at 100 mK. Increasing field (blue) and decreasing field (red), both scanned at 50 mT/min

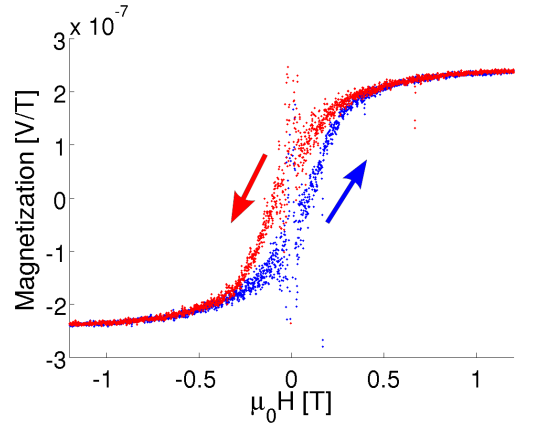

Figure 6.13: Zoom of previous figure in order to be able to better see the hysteresis.

Figure 6.10 shows the data from a scan at 100 mK. The temperature has been constant while the field has been varied. In the case of the 100 mK measurement, the signal corresponding to zero torque is $U_0 = 9.5 \cdot 10^{-7}$ V. The value of U_0 is used in order to find the magnetization, which is $m = \frac{\tau}{H} \propto \frac{U-U_0}{H}$. The field scan is performed with both increasing and decreasing field. These two data series are then transformed in Matlab by first dividing the signal with the field. This gives the magnetization which can be plotted and for the case of 100 mK the result is a plot of the magnetization as a function of the

applied field or a hysteresis curve as can be seen in figure 6.12. For higher temperatures, 400 mK and above, there is no difference in scanning up or down. in order to be able to see the hysteresis more clearly figure 6.13 shows a zoom. In order to get a more smooth curve every 50 points are averaged and the standard deviations of the mean, see equation (6.1), are used as error bars, the result can be seen in figure 6.14 It should be noted that

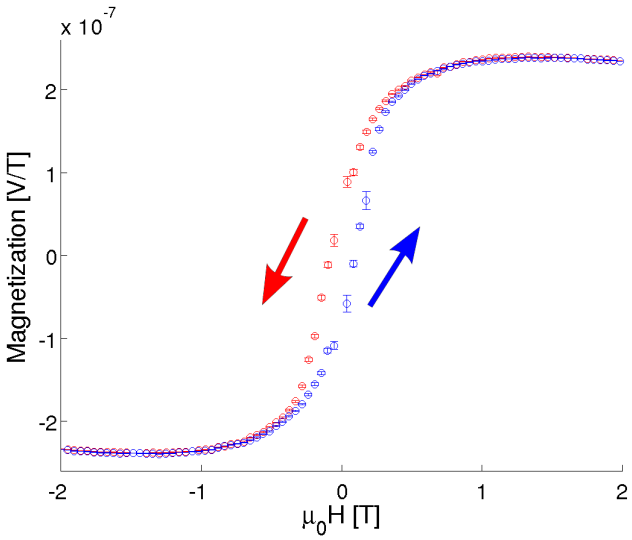

Figure 6.14: Magnetization curve of $LiHoF_4$ at 100 mK, every point consists of 50 measurements averaged, the standard deviation is used as uncertainty.

the setup had some misalignment. After the measurements were finished the cantilever with sample was measured with a Laue setup in order to check the alignment, as described in section 5.6. The sample was 4° off, which means that it is not possible to measure the entire magnetization.

6.2.3 Low Temperature Hysteresis of $LiHoF_4$

Figure 6.15 shows the hysteresis curve measured for $LiHoF_4$ at around 50 mK. Every 50 points have been averaged and the standard deviation σ has been used as error bars. The hysteresis curve, depicted by the blue and red point, looks like a normal magnetic hysteresis curve for a ferromagnet, but the black curve from origin exceeds the hysteresis curve which is unexpected. When measuring the black curve the magnetic field has been turned off for about 2.5 hours (for filling He). Thereafter the blue and red curves have been measured. The sweep rate of 0.02 T/min was identical for all three measurements. A hysteresis curve was also measured at 100 mK, represented in figure 6.14 and a zoom in figure 6.17. For 50 mK the coercive field was found to be about 0.18 T, at 65 mK it is about 0.15 T and for 100 mK about 0.10 T. At 400 mK the measurement has only been performed with decreasing magnetic field, but it is clear from that measurement, illustrated in figures 6.18 and 6.19, that there is no hysteresis in these data as the displacement from zero is very small. Figure 6.20 shows the magnetization curve at 400 mK with a decreasing field. This means that the hysteresis seems to have disappeared at some temperature between 100 and 400 mK.

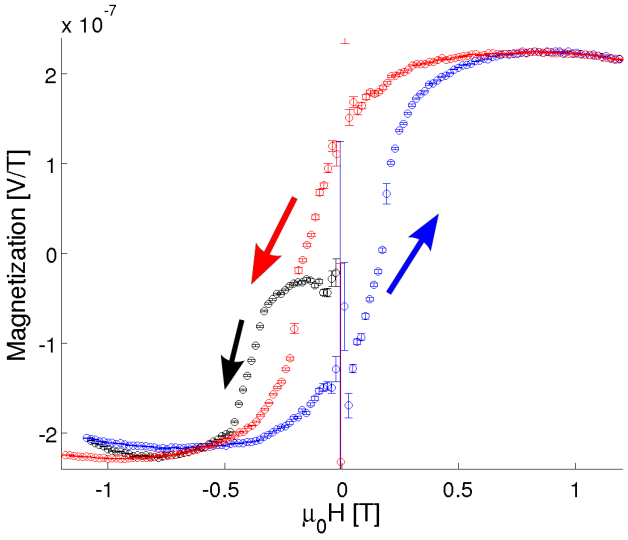

Figure 6.15: Magnetization curve of $LiHoF_4$ at 50 mK, increasing field (blue) and decreasing field (red). The black curve was measured after the magnetic field had been turned off for about 2.5 hours.

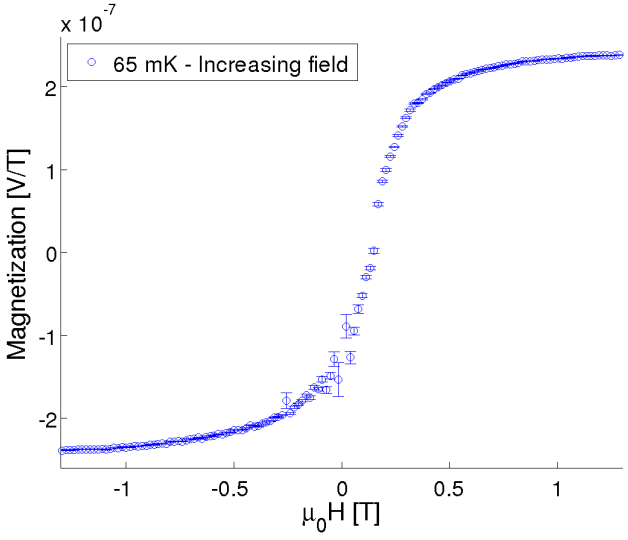

Figure 6.16: Magnetization curve of $LiHoF_4$ at 65 mK with increasing field.

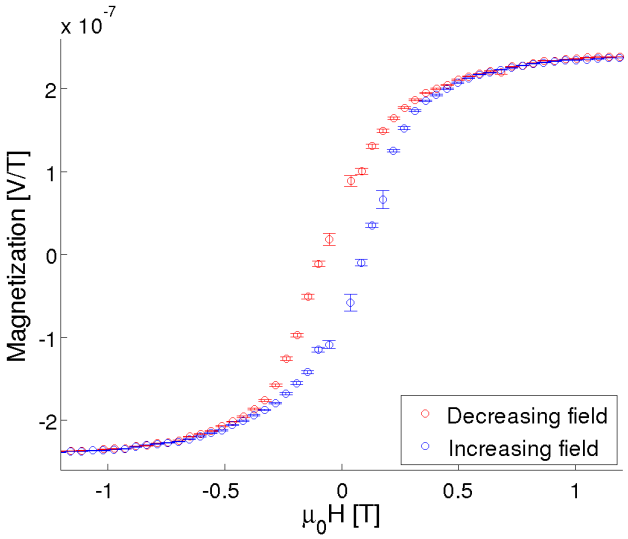

Figure 6.17: Magnetization curve of $LiHoF_4$ at 100 mK, increasing field (blue) and decreasing field (red).

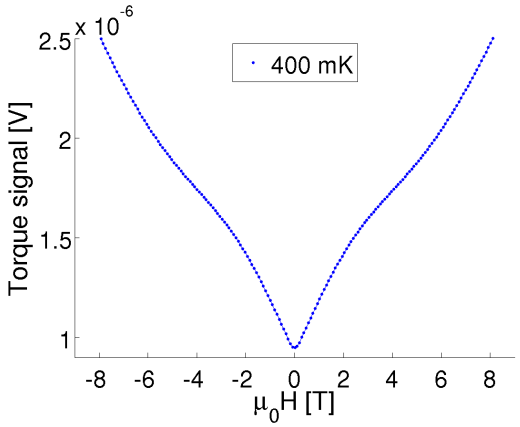

Figure 6.18: Torque signal of the sample in a field scan from 9 to -9 T at 400 mK.

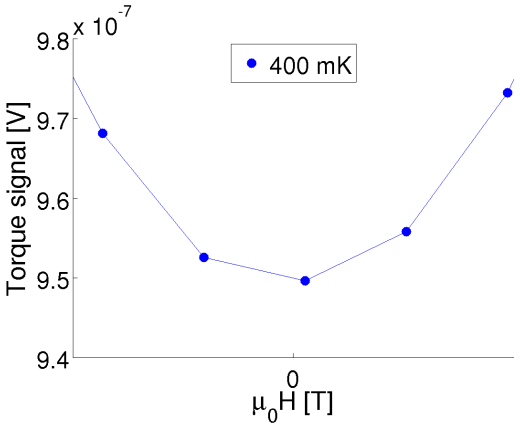

Figure 6.19: Zoom of the previous figure, the displacement is smaller here than in the case of 100 mK in figure 6.11.

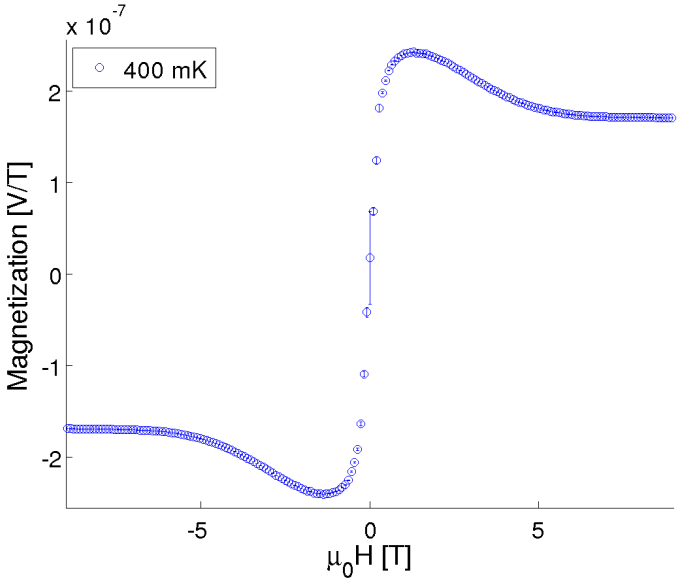

Figure 6.20: Magnetization of $LiHoF_4$ at 400 mK.

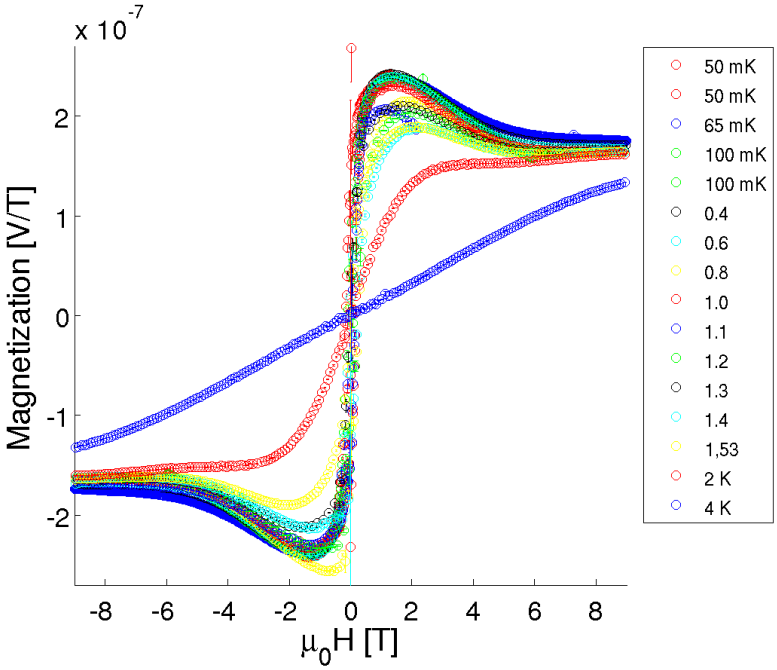

Figure 6.21: Magnetization curves for all the different temperatures.

6.2.4 Fitting of Data at 4 K of $LiHoF_4$

The magnetization curves for all the different temperatures between 50 mK and 4 K, is illustrated in figure 6.21. It seems that the data at 4 K and 2 K might be in the paramagnetic phase, as their signals are less curved than the data at lower temperatures. Since $T_C = 1.53$ K they are both above the temperature for the ordered phase, see also section 6.2.5 where all the temperature scans are shown. The data obtained at 4 K was

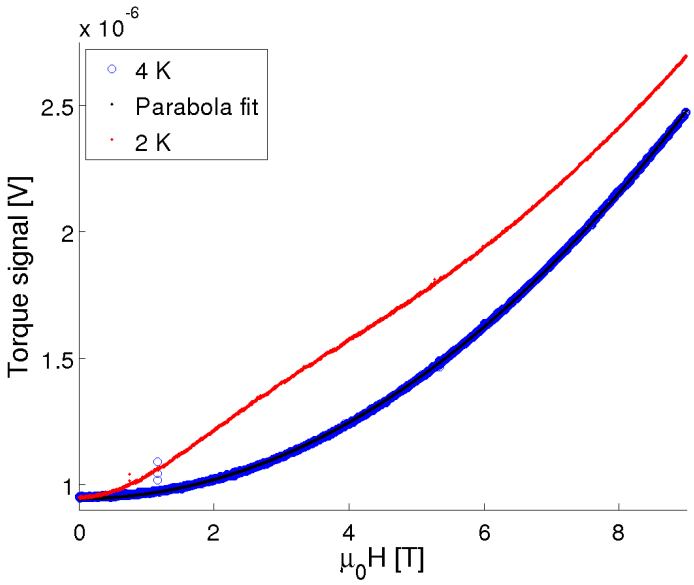

Figure 6.22: Fieldscan of $LiHoF_4$ at 2 K (red) and 4 K (blue). The 4 K data is fitted to a polynomial of second order (black). The 2 K data only fitted well to a polynomial of 12th order.

found to have a quadratic dependence on H, as shown in figure 6.22, but the torque at 2 K did not fit well to a second order polynomial. One could imagine that at temperatures up to ~ 30 % above the critical temperature, *i.e.* 2 K, critical phenomena of some kind still takes place. The quadratic dependence on H is en agreement with the theory for a paramagnet, which is predicted to behave like the Brillouin function. At low fields, the Brillouin function is linear and the magnetization is thus proportional to the applied field.

6.2.5 Temperature Scans

In the following scans the temperature has been scanned with a fixed magnetic field. In figure 6.23 we show temperature scans for fields of 0.05 T , 0.1 T and 0.2 T. For 0.1 T and 0.2 T every 200 points - 300 for 0.05 T - have been averaged to one, and the standard deviation of the mean used as error bars. The temperature scans at 0.1 T and 0.2 T seem to show two phase transitions, the expected transition at the critical temperature at 1.5 K and another one at approximately 0.17 K. The temperature scan at 0.05 T shows signs of a transition but not very clearly. At such a small field the signal is almost to small for the setup to be able to measure the torque. The low temperature transition will be discussed in section 3.2.3. The magnetization for four of the higher fields is shown in

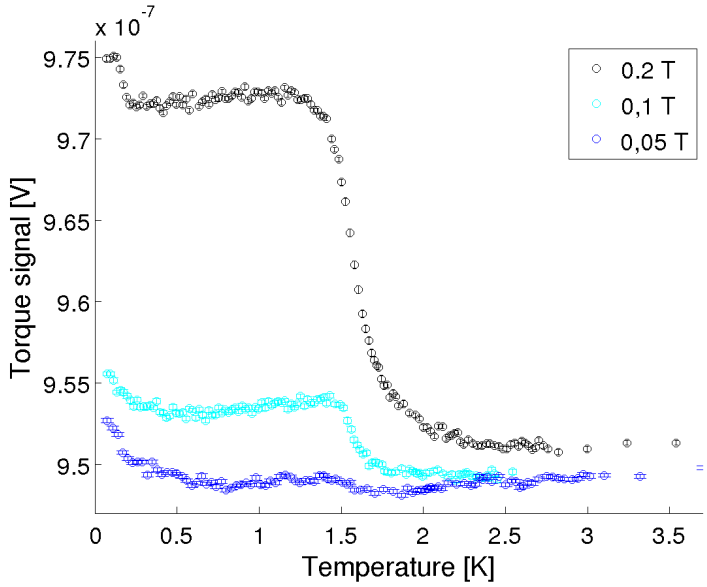

Figure 6.23: Temperature scan of $LiHoF_4$ at 0.2 T (black), 0.1 T (cyan) and 0.05 T (blue). The phase transition from a ferromagnet to a paramagnet is present at the critical temperature T_c.

figure 6.24. Figure 6.26 shows the torque as a function of temperature at all the different fields between 0.05 T and 4.95 T.

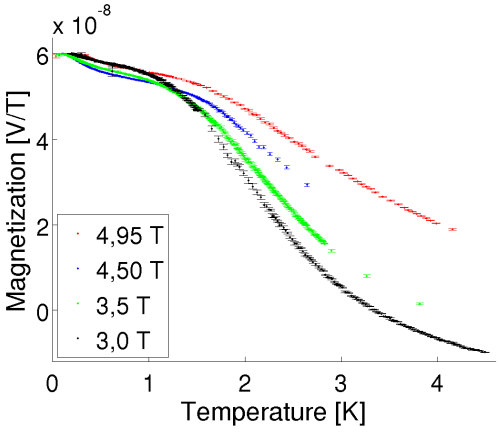

Figure 6.24: Magnetization for different fields from 3.0 T to 4.95 T.

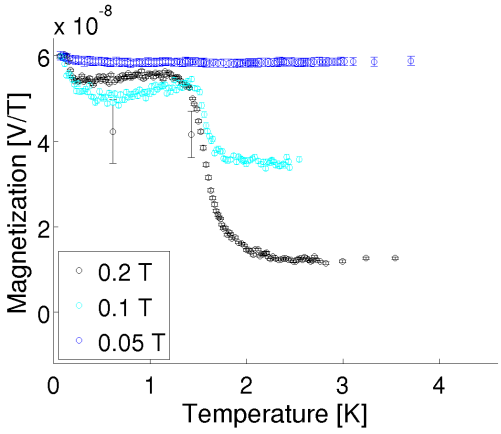

Figure 6.25: Magnetization for different fields from 0.05 T to 0.2 T.

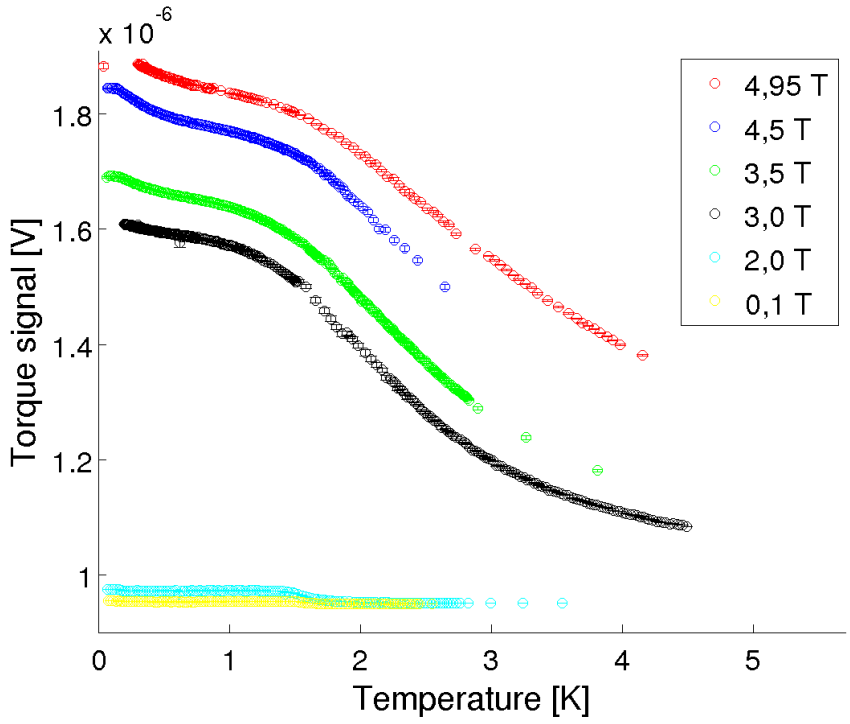

Figure 6.26: The torque as a function of temperature at fields from 0.05 T to 0.2 T.

Chapter 7

Discussion

7.1 Angle Dependence of the Phase Transition

The magnetization as a function of applied magnetic field is illustrated in figure 6.21. It did not show any quantum phase transition, which was somewhat of a surprise. After finishing the measurements at EPFL the sample's alignment, with respect to the cantilever, was checked using Laue diffraction. It was found to be 4 °off, as mentioned in

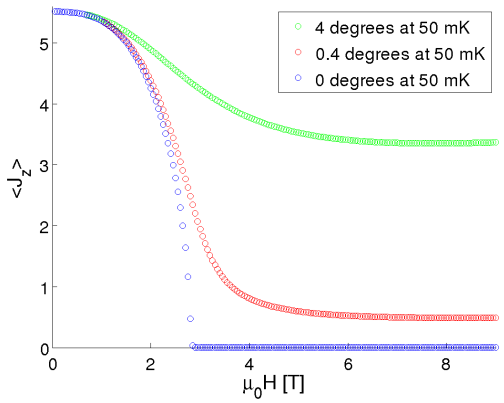

Figure 7.1: Angle dependence for the phase transition at 50 mK.

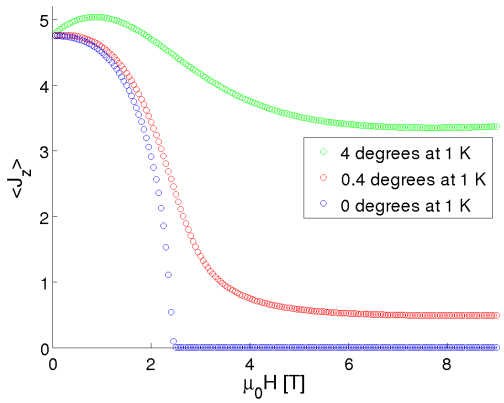

Figure 7.2: Angle dependence for the phase transition at 1 K.

section 5.6. This deviation seems small at first sight, but if one tries to make a mean field calculation of the quantum phase transition, with a small angular offset to the magnetic field, it shows to have a significant effect. The mean field program used is the one already discussed in section 3.4.1. Figures 7.1 and 7.2 shows the calculated mean magnetic moment in the z direction $< J_z >$ as a function of three different angles at respectively 50 mK and 1 K. $< J_z >$ has a lower value at 1 K compared to 50 mK, this is due to the thermal disorder. The calculation is performed for offsets of 0°, 0.4° and 4°. It is clear that an angle of 4° smears the measurements in such an extent that the transition is no longer visible. This explains why it was not possible to see the quantum phase transition as a function of applied field. The magnetic field induces a moment along the field in the x direction which destroys the phase transition.

At 1 K and a 4° offset, $< J_z >$ increases around $1 - 1.5$ T, this could be because the z component of the field induces a magnetic moment, but as the applied field increases the transverse field has a larger effect and the magnetization drops again.
Similarly the mean field calculation is performed for temperature scans at 0.1 T and 2 T at figures 7.3 and 7.4. It is clear from the figures that the phase transition is much more

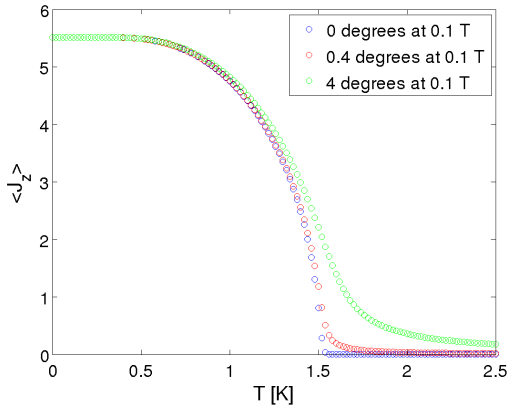

Figure 7.3: Angle dependence for the phase transition at 0.1 T.

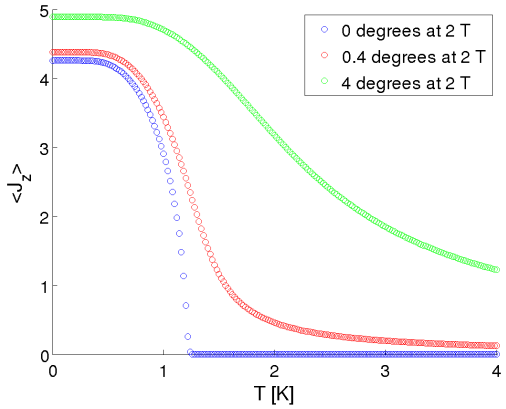

Figure 7.4: Angle dependence for the phase transition at 2 T.

smeared at 2 T compared to 0.1 T, this is probably because the absolute field component in the z-direction is smaller as the field is smaller. The phase transition is more clear in the temperature scans compared to the field scans, thus the field has a smaller effect here.

7.2 Comparison between Mean Field Program and Measurements

We now continue with a comparison between the measurements and the mean-field program, both for the temperature scans and field scans. The angle has been set to 4° since a) this was the angle measured with Laue diffraction and b) it agrees with the mean field calculations. The axes have been scaled in such a way that the theory and measurements overlap. There are an axis for both measurements (blue, left) and theory (green, right).

7.2.1 Field Scans

The magnetization curves as function of magnetic fields at different temperatures are illustrated in figure 6.21. A comparison of the measurements to the results of mean field program are presented, at selected temperatures. In figures 7.5 to 7.12 a comparison between the data from the mean field program and the measurements are illustrated.
All the figures show that the measurements are slightly below the mean field calculations at low field. The mean field calculations does not incorporate domain effects and thus no hysteresis is present. The domains within the sample will make it harder to magnetize as some of them will be opposed to the field. Thus could explain that the measurements

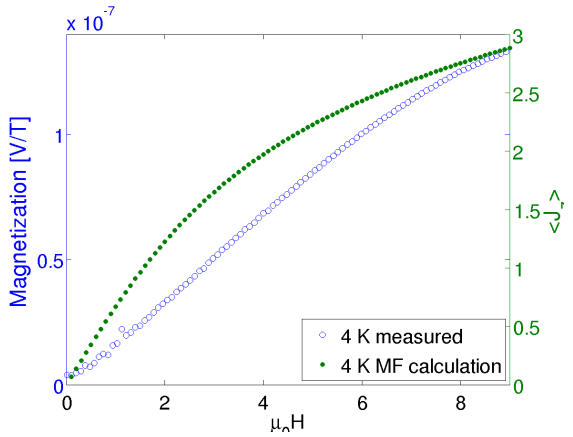

Figure 7.5: Comparison between the mean field calculated $< J_z >$ and the measured magnetization at 4 K.

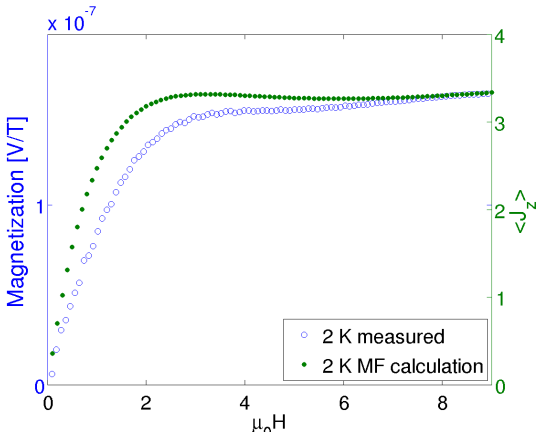

Figure 7.6: Comparison between the mean field calculated $< J_z >$ and the measured magnetization at 2 K.

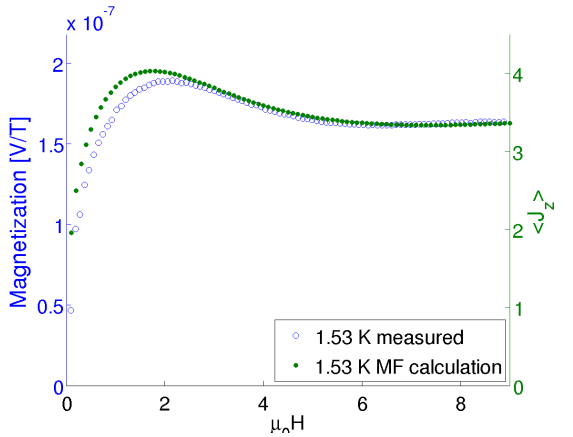

Figure 7.7: Comparison between the mean field calculated $< J_z >$ and the measured magnetization at 1.53 K.

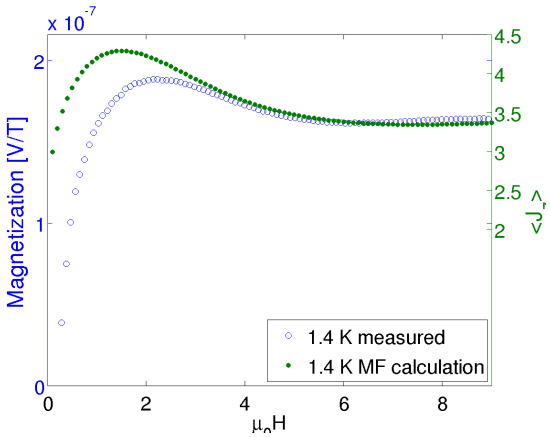

Figure 7.8: Comparison between the mean field calculated $< J_z >$ and the measured magnetization at 1.4 K.

are somewhat below the calculated values.
It is interesting that the measurements at 2 K and especially at 4 K deviate from the mean field calculations. The measurements should be consistent with the mean field program in the paramagnetic phase. This could imply that interactions are important. Interactions are more dominant in the ordered phase, here the theory and measurement were in better agreement than in the paramagnetic phase. Another factor for this discrepancy could be the misalignment in angle. To investigate this further, mean-field calculations must be run for many offset angles, this was beyond the scope of this thesis.

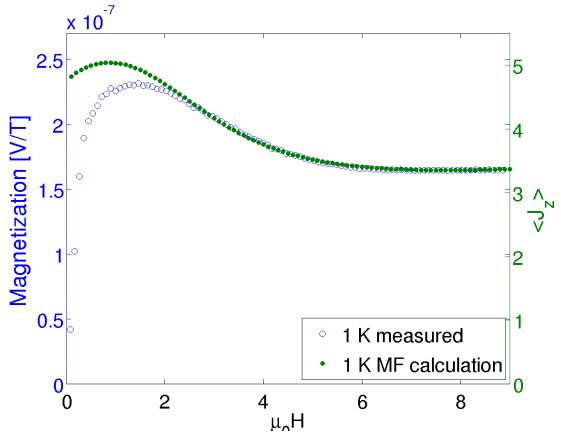

Figure 7.9: Comparison between the mean field calculated $< J_z >$ and the measured magnetization at 1 K.

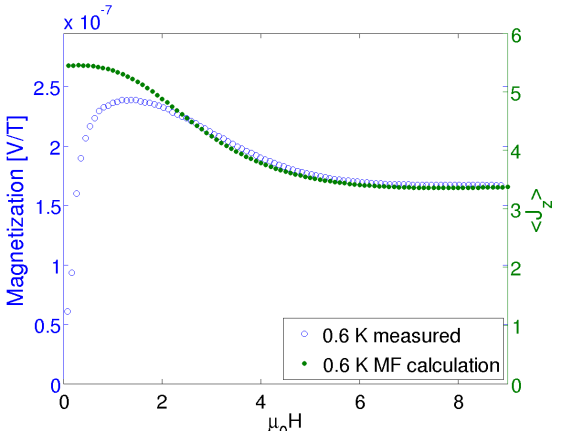

Figure 7.10: Comparison between the mean field calculated $< J_z >$ and the measured magnetization at 600 mK.

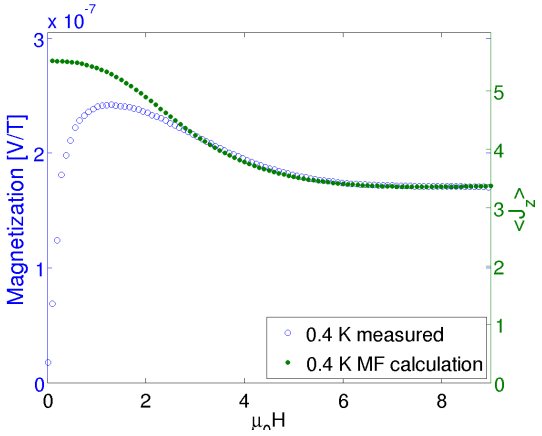

Figure 7.11: Comparison between the mean field calculated $< J_z >$ and the measured magnetization at 400 mK.

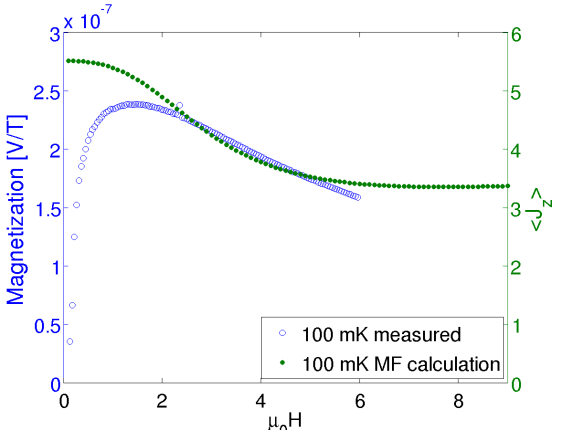

Figure 7.12: Comparison between the mean field calculated $< J_z >$ and the measured magnetization at 100 mK.

7.2.2 Temperature Scans

We continue with a comparison of the measured temperature scans to the calculated ones from the mean field program. The temperature scans at 0.1 T, 0.2 T and 3 T

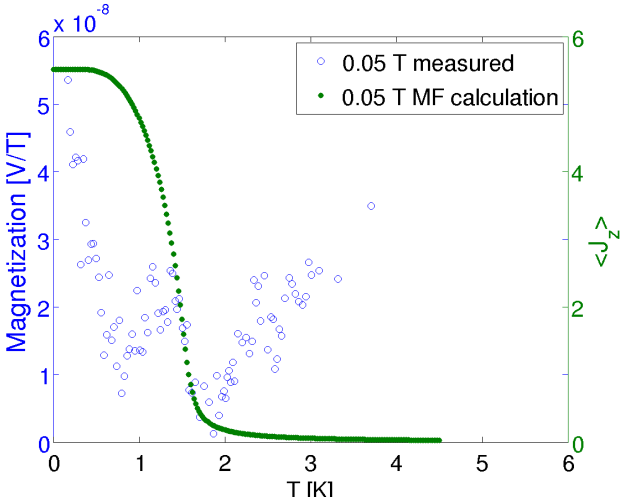

Figure 7.13: Comparison between the mean field calculated $< J_z >$ and the measured magnetization at 0.05 T.

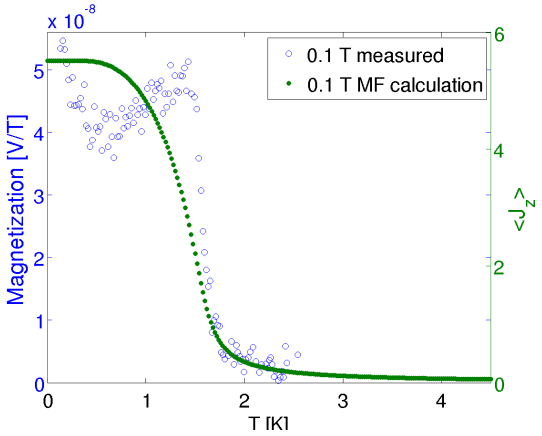

Figure 7.14: Comparison between the mean field calculated $< J_z >$ and the measured magnetization at 0.1 T.

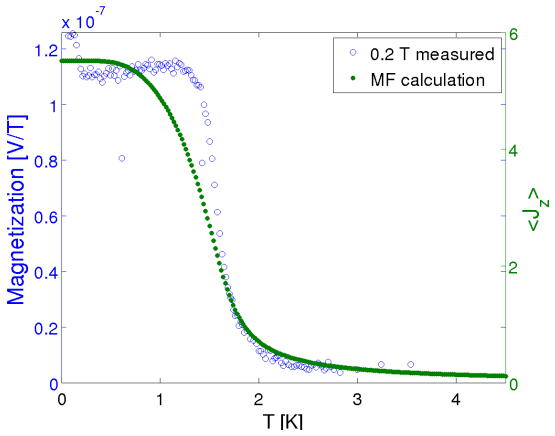

Figure 7.15: Comparison between the mean field calculated $< J_z >$ and the measured magnetization at 0.2 T.

respectively in figures 7.14, 7.15 and 7.16 are in more or less agreement with the theory. The temperature scan at 0.05 T in figure 7.13 does not agree very well with theory, this is probably due to the fact that the measurement at 0.05 T is on the limit of how small signals we can measure. A small field results in a small signal which makes it difficult for the setup to measure the magnetization. The scan at 3 T is in fine agreement with the mean field calculation, but at higher fields the comparison is no longer good. One could think that this is due to the high fields, which could be difficult to measure for the setup, but we do not see this problem in the field scans, making it implausible. Another solution

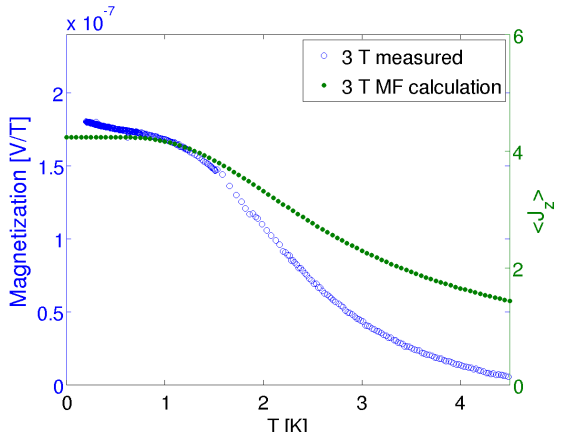

Figure 7.16: Comparison between the mean field calculated $< J_z >$ and the measured magnetization at 3 T.

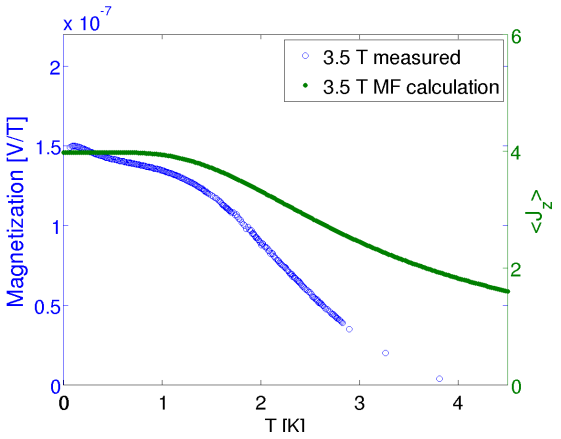

Figure 7.17: Comparison between the mean field calculated $< J_z >$ and the measured magnetization at 3.5 T.

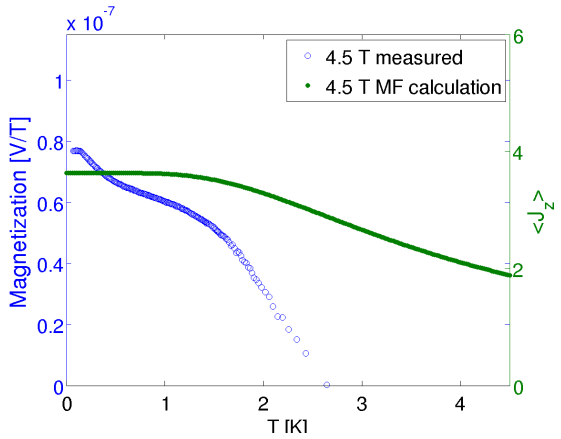

Figure 7.18: Comparison between the mean field calculated $< J_z >$ and the measured magnetization at 4.5 T.

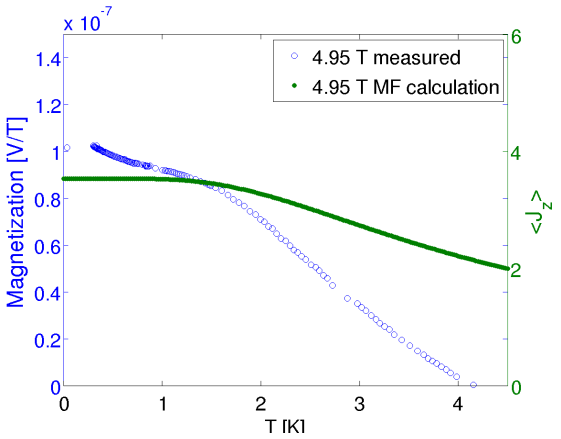

Figure 7.19: Comparison between the mean field calculated $< J_z >$ and the measured magnetization at 4.95 T.

could be to change the coupling in the mean field program, hoping this would make the curve more steep. Unfortunately tuning the exchange coupling does almost nothing but displacing the curve up or down in stead of effecting the slope.
The slope is more steep for the measurements than for the mean-field calculations, thus the the critical exponent β is larger for the measurements. The fact that mean-field does not predict the right value is normal, it will always predict $\beta = \frac{1}{2}$. A 3 dimensional Ising system has $\beta \sim \frac{1}{3}$, thus displays a sharper phase transition.

7.3 The Phase Diagram

Previous work on $LiHoF_4$ was the foundation for the experiments made with this setup. The phase diagram in figure 7.20 is obtained both through neutron scattering by Henrik Rønnow *et al.* [38] and susceptibility by Bitko, Rosenbaum and Aeppli [4]. Figure 7.21

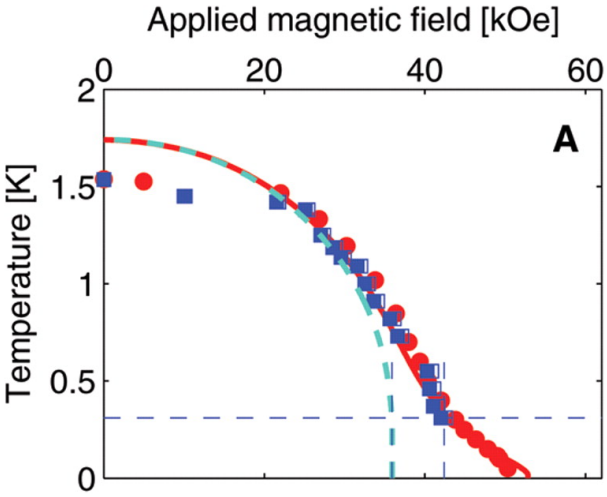

Figure 7.20: Phase diagram obtained through susceptibility (red) [4] and neutron scattering (blue) [38]. The lines represent calculations with (solid) and without (dashed) hyperfine interaction, figure taken from [38].

illustrates the temperature scan at 0.2 T. One way to obtain T_c, for these data where the magnetization does not clearly go to zero, is to choose T_c to be the point halfway through the phase transition. This is done by first drawing a horizontal line through the data in the ferromagnetic and paramagnetic phase. A line through the phase transition region is also made, and the temperature found half way through is taken to be the critical temperature. This results in a critical temperature of 1.58 K with a magnetic field of 0.2 T which corresponds nicely with the existing phase diagram. The critical temperature for 0.1 T is also found to be 1.58 K, this seem reasonable as the change of T_c is small as a function of applied fields, up to ~ 0.2 T.
As we saw in the previous section the field scans did not reveal a phase transition, and the temperature scan had a somewhat smeared transition. We also saw that the mean field calculations and the field scan measurements agree very well, therefore the mean field calculations can be used to obtain the critical temperature. With the angle set to zero the calculations can be run, thereby making it possible to obtain the critical temperature we would have measured if the alignment had been better. Figure 7.22 illustrates how this is done for the temperature scan at 0.2 T. Thus two methods of determining the critical temperature has been applied, resulting in a critical temperature of 1.55 or 1.58 K at 2 T. The critical temperature for two different methods agree very well.

7.4 Low Temperature Hysteresis

In figures 6.15, 6.16 and 6.17 we saw a hysteresis at temperatures of respectively 50 mK, 65 mK and 100 mK. Figure 7.23 shows the coercive field for three different temperatures

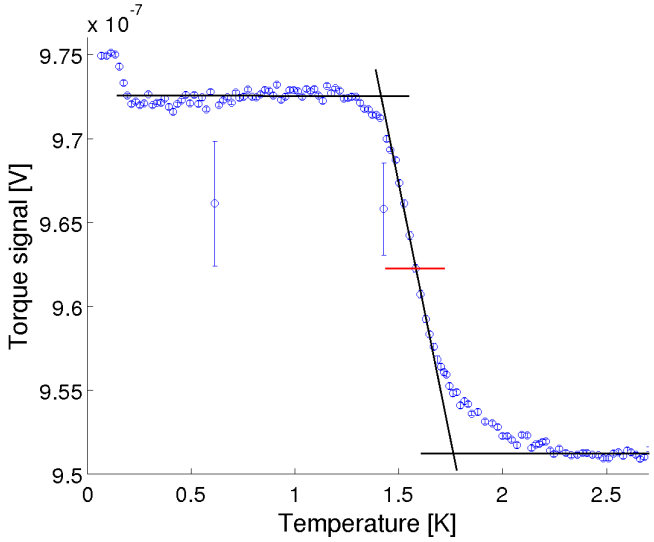

Figure 7.21: Temperature scan at 0.2 T, the horizontal line is the background level. Another line is drawn through the phase transition, half way through is the critical temperature.

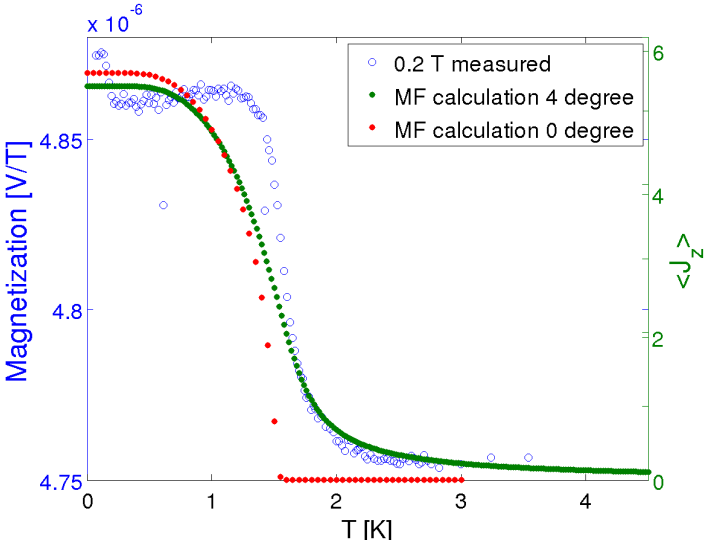

Figure 7.22: By comparing the measurement with the mean field calculation at 4°, $T_c = 1.55$ K can be obtained through the mean field calculation at 0°.

along with a linear fit of these points. If we assume that the coercive field is linear as a function of temperature, the field would disappear at 150 mK. The low temperature hysteresis seems to have disappeared in figure 6.19 at 400 mK as the displacement of the minimum from zero is very small. This could mean that a low temperature hysteresis is present, which diminishes with increasing temperature. The coercive field seems to have a linear behaviour, if one made a line of the three points it would reach zero at about 150 mK.

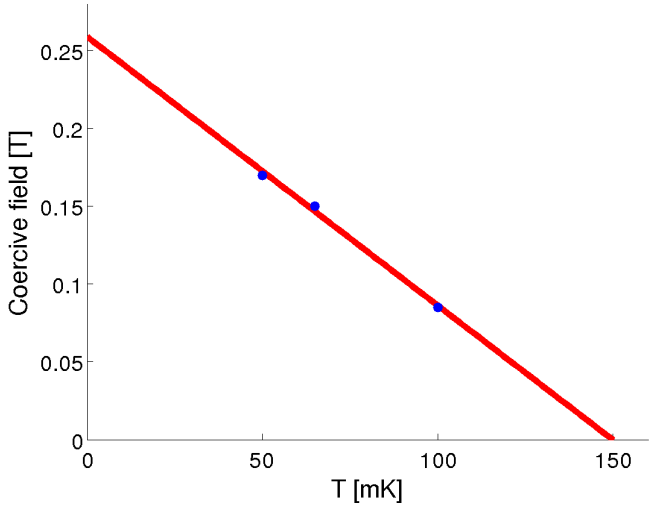

Figure 7.23: The coercive field of the low temperature hysteresis as a function of temperature, along with a linear fit (red line).

7.4.1 Coupling to the Nuclear Spins

The origin of the hysteresis shown in figure 7.21 is not clear, but previous work on $LiHoF_4$ could give an idea. Rønnow *et al.* [38] measured that below 310 mK the hyperfine coupling plays a role for the magnetic excitation spectrum, as shown in figure 3.7. The low temperature hysteresis presented here could be caused by the contribution from the nuclear spins. As mentioned previously the hyperfine coupling to the nuclear spins normally has a vanishing influence on the properties of the electronic magnetic moments. Converting the hyperfine Hamiltonian into an effective magnetic field, we find

$$\mathscr{H} = A\boldsymbol{I}\cdot\boldsymbol{J_z} = g\mu_B H_{hf}\cdot J_z \tag{7.1}$$

$$\mu_0 H_{hf} = \frac{\mu_0 AI}{g\mu_B} = 0.16\ \mathrm{T} \tag{7.2}$$

at T = 0, where $A = 3.36$ μeV as discussed in section 3.2.3. This value corresponds almost exactly to the to the coercive field of 0.17 T measured at 50 mK Figure 7.24 shows a mean field calculation, performed by Jens Jensen, of the hyperfine field as a function of field. This program is similar to the one described in section . The figure shows that the hyperfine field disappear at the critical temperature, which is in contradiction to our measurements where the hyperfine was vanishing already at 400 mK. Thus the hyperfine can give the right size of the coercive field at low temperatures but not explain why it disappears at 400 mK.

7.4.2 Nuclear Relaxation Effects

Figure 6.15 showed a hysteresis curve measured when the field had been turned off for 2,5 hours. The sample was now more difficult to magnetize. This could be caused by the fact that the sample had made domains, therefore half of the magnetic moments pointed against the applied field thus making the sample more difficult to magnetize.

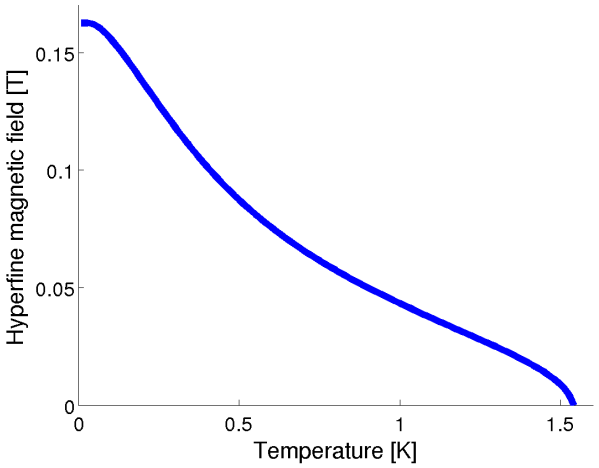

Figure 7.24: Hyperfine magnetic field as a function of temperature, determined through mean field calculations by Jens Jensen. The hyperfine field vanishes at the critical temperature.

In any case nuclear relaxation in insulators can easily be of that order at low temperatures [35]. With this setup a measurements is taken approximately every second, therefore the relaxation must take between 1 s and 2.5 hours.
The Ho atoms order in the z direction, but whether they order in the $+z$ or $-z$ direction can be determined by the nuclei. The Ho atoms will flip at the latest when $H_{HF} > H_{applied,z}$, at low temperatures, but they can also flip before. Nuclei are very heavy, which means they have a smaller magnetic moment, as its size scales with the inverse of the mass. In the case of a magnetic field, the nucleus reacts rather slowly, because it primarily feels the field from the electrons as this field is normally larger than the applied field [17]. Maybe this slow relaxation could explain the black curve.

7.5 The extra Phase Transition at Low Temperatures

The temperature scans performed at 0.05 T, 0.1 T and 0.2 T illustrated in figure 6.23 showed the expected phase transition at approximately 1.58 K. In addition to this, the scans also displayed an abrupt change in magnetization at temperatures from 140 mK to 200 mK. This change could look like an extra phase transition. This measurement was performed after the sample had been up and down in field several times, with a maximum of ± 9 T. The measurement was performed with an increasing temperature. the measurement before was also a temperature scan at 0.2 T. As the measurement is performed with increasing temperature, the extra phase cannot be caused by domains. This phase could be caused by the hyperfine interaction, but this effect seems to to small to be the sole explanation.
Another possibility is that this is simply an artefact of the measurement setup. In section 6.1.2 the field dependence for an empty cantilever was examined. Figure 6.7 showed that at zero field there is a temperature dependence of $\sim 2 \cdot 10^{-10}$ V, but this background is only $\frac{1}{3}$ of the change in signal we see for the low temperature transition.

7.6 Precision and Measurement Setup

As the calibration and the measurements were performed in different laboratories and thus different lock-in amplifiers were used it was not possible to get the magnetization in absolute units, *e.g.* in units of the Bohr magneton μ_B. However a calibration was still possible as the comparison of the measurements with the mean field program showed to be successful. Plotting the data and calculated mean field magnetization $< J_z >$ reveals the correspondence to be $1 \frac{\mathrm{V}}{\mathrm{T}} = 1.7 \cdot 10^7 < J_z >$ The noise of the magnetization measurements can be determined from the error bars and the smallest found are approximately $1 \cdot 10^{-10} \frac{\mathrm{V}}{\mathrm{T}}$ corresponding to $2 \cdot 10^{-3} < J_z >$ at 0.1 T. From the calibration performed in section 5.3 we know that this corresponds to 13.7 Nm at 0.1 T. The smallest signal measured is the temperature scan at 0.1 T in figure 6.23. The figure shows the phase transition, and the difference in signal of the two phases is $\sim 5 \cdot 10^{-9}$ V.
Another issue which needs to be addressed is the fact that the angle between the field and the sample is changed during the measurement as the cantilever bends a little under torque. There is no easy solution to this, but as long as the sample is not to large it is a minor problem.

Chapter 8

Neutron Scattering on $CoCl_2 \cdot 2D_2O$

While doing my master's thesis I had the possibility to perform neutron scattering experiments on another Ising-like system, $CoCl_2 \cdot 2D_2O$.

8.1 Neutron Scattering

Neutron scattering is a powerful tool to investigate both structures and dynamics in solid state physics. It is especially useful when exploring magnetic properties. As the neutron has spin half ($s = \frac{1}{2}$) it can interact with the magnetic moments of the unpaired electrons in the crystal. Neutrons are scattered from interaction with the nucleus as opposed to X-rays which interact with the electron cloud. Therefore the ability to scatter neutrons is not proportional to the element's atomic number. The neutron has zero net charge which allows it to penetrate deep into a crystal, thereby making it possible to perform bulk measurements instead of surface measurements, and possible to have the sample in different environments such as cryostats, magnets or pressure cells. The downside of neutron scattering are the rather low intensities compared to X-rays. This requires long measurement times.
Neutrons can be produced either by spallation or by fission. Producing neutrons by spallation is done by first producing highly accelerated protons with energies of the order GeV. These protons will hit and split heavy nuclei with a large surplus of neutrons hereby creating free neutrons in the process. Fission processes in a nuclear reactor use neutrons to maintain a chain reaction, a surplus of neutrons can then be used for scattering experiments. The neutrons emerging from the source have a spectrum of energies, depending on the temperature of the moderator. Moderators are generally used to slow down the neutrons and thus produce wavelengths that are comparable to the atomic spacing in solids and liquids, and energies that are comparable to those of dynamic processes in materials. The neutron facility used for the experiments in this thesis is a reactor.

8.1.1 Scattering from a single Nucleus

In a neutron scattering experiment, a beam of neutrons hits a sample and an interaction takes place. If a monochromator is used the initial neutron have a narrow wavelength

distribution *i.e.* a single wavelength and can be described as a plane wave

$$\psi_i(\boldsymbol{r}) = \frac{1}{\sqrt{Y}} \exp\left(i\boldsymbol{k}_i \cdot \boldsymbol{r}\right) \tag{8.1}$$

where Y is a normalization constant. The neutrons are scattered by the nucleus by the strong nuclear force. Scattering from a single nucleus is isotropic as the range of the strong nuclear force is much smaller than the wavelength of the neutron. The range of the strong nuclear force is of the order fm whereas the wavelength of the neutron is of the order Å *i.e.* much larger. If we assume that the nucleus has a fixed position $\boldsymbol{r_j}$, and that we are far away from the nucleus (*i.e.* $|\boldsymbol{r} - \boldsymbol{r_j}| \gg b$), where b_j is the scattering length, then the scattered neutron can be described as a spherical wave

$$\psi_f(\boldsymbol{r}) = \psi_i(\boldsymbol{r_j}) \frac{-b_j}{|\boldsymbol{r} - \boldsymbol{r_j}|} \exp\left(ik_f|\boldsymbol{r} - \boldsymbol{r_j}|\right) \tag{8.2}$$

The scattering length is a measure of the size of the nucleus, which is unique for each isotope. As the nucleus is fixed in position the energy of the neutron is conserved $E_i = E_f$ and $k_i = k_f$, this is known as elastic scattering.

8.1.2 Scattering from a Crystal

In a crystal the incoming beam of neutrons are scattered by the lattice planes through a scattering angle of 2θ. The scattered neutrons produce Bragg reflections when the scattering vector $\boldsymbol{q}$ equals a reciprocal lattice vector $\boldsymbol{\tau}, |\boldsymbol{\tau}| = \frac{2\pi}{|d|}$. This condition can be expressed by Bragg's law

$$n\lambda = 2d\sin(\theta) \tag{8.3}$$

where n is a positive integer, θ is the angle between the incident neutron beam and the lattice scattering planes and a lattice spacing d.

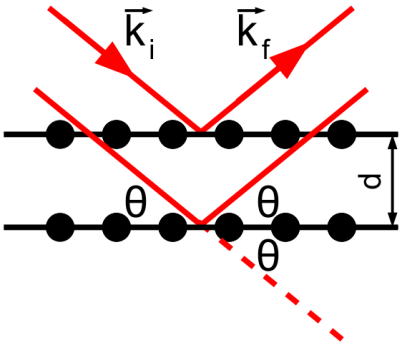

Figure 8.1: Neutrons with wave vector $\boldsymbol{k_i}$ are scattered 2θ to $\boldsymbol{k_f}$ by the crystal planes, figure taken from [21].

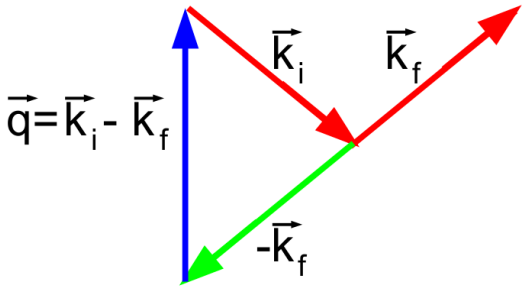

Figure 8.2: The scattered neutrons obtain constructive interference when the scattering vector $\boldsymbol{q} = \boldsymbol{k_i} - \boldsymbol{k_f} = \boldsymbol{G}$, where $|\boldsymbol{G}| = \frac{2\pi}{d}$ when $\boldsymbol{q} = \boldsymbol{G}$, where d is the spacing between the planes in the atomic lattice, figure taken from [21].

8.1.3 Inelastic Scattering

For inelastic scattering, the energy of the incoming neutron is no longer equal to the energy of the outgoing neutron. The neutron either delivers or absorbs energy from the sample. The neutron has created an excitation in the sample with energy $E = \hbar\omega$ and wave vector $\boldsymbol{q}$. Conservation of energy and momentum give the following equations:

$$E_i = E_f + \hbar\omega \tag{8.4}$$

$$\boldsymbol{k_i} = \boldsymbol{k_f} + \boldsymbol{q} + \boldsymbol{G} \tag{8.5}$$

Measuring $\boldsymbol{k_i}$ and $\boldsymbol{k_f}$ makes it possible to determine ω and $\boldsymbol{q}$. Quasiparticles within the sample (such as magnons or phonons) often have similar energies as that of $\hbar\omega$ and can therefore be measured using inelastic neutron scattering [23].

8.2 The Triple-axis Spectrometer

A triple-axis spectrometer (TAS) is an instrument used for inelastic neutron scattering. It allows determination of how much a sample scatters as a function of $\boldsymbol{q}$ and $\hbar\omega$.The neutron energy transfer is determined by selecting E_i and scanning E_f, or vice versa. Figure 8.3 illustrates the principle of the triple-axis spectrometer. The TAS instrument is placed

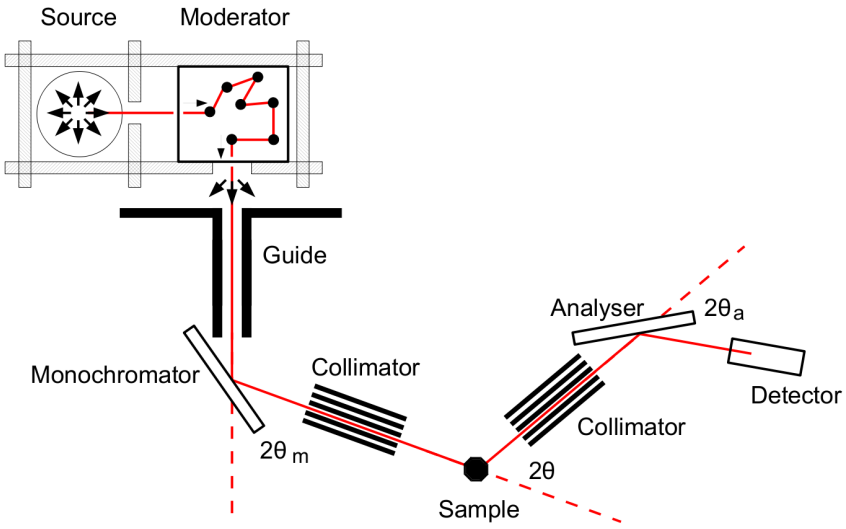

Figure 8.3: Schematics of a triple-axis spectrometer, figure taken from [21].

after a long guide, in order to minimize background. The triple-axis spectrometer consists of three independently controlled axes of rotation for the sample, monochromator, and analyzer crystals. The collimator is a device capable of collimating the neutron beam. It consist of a narrow tube, thus only neutrons travelling parallel to the tube axis can traverse the entire length. The initial beam is Bragg scattered by an angle $2\theta_m$ on a monochromator crystal making it possible to choose the desired E_i. The beam of neutrons continue to the sample where it is scattered by an angle of 2θ. Finally the beam is scattered by the analyzer crystal by an angle $2\theta_a$ and detected in the position sensitive detector. By selecting the three scattering angles $2\theta_m$, 2θ, $2\theta_a$ and sample rotation ω,

the spectrometer can be tuned to any scattering vector $\boldsymbol{q}$ and energy transfer $\hbar\omega$ allowed by equation (8.4) and 8.5. A monitor is placed between the collimator and the sample in order to measure the number of incoming neutrons. [42]

8.3 Properties of $CoCl_2 \cdot 2D_2O$

$CoCl_2 \cdot 2D_2O$ has a monoclinic crystal structure, with room temperature lattice parameters $a = 7.256$Å, $b = 8.575$Å, $c = 3.554$Å and $\beta = 97.60°$. Narath *et al.* [31] measured that $CoCl_2 \cdot 2D_2O$ undergoes a phase transition at $T_N = 17.5$ K, from a paramagnet at high temperatures to an antiferromagnet below T_N. This was confirmed by Cox *et al.* [9] and it was also determined that the spins point along the b axis. This made it possible to find the magnetic Bragg reflections, of which the first five are listed in table 8.1. Inside

Table 8.1: Nuclear and magnetic Bragg reflections for $CoCl_2 \cdot 2D_2O$, conducted by Jacob Larsen [21].

h	k	l	$\lvert\boldsymbol{q}\rvert$ [Å^{-1}]	$\lvert F_N\rvert^2$ [10^{-28}cm^2]	$\lvert F_M\rvert^2$
1	1	0	1.139	0.425	-
0	2	0	1.478	3.621	-
1	1	$\overline{1}$	2.014	7.943	-
1	1	1	2.206	2.255	-
2	0	$\overline{1}$	2.315	127.646	-
2	0	1	2.642	18.728	-
0	1	0	0.739	-	4
0	3	0	2.198	-	4
0	5	0	3.663	-	4
2	1	1	2.744	-	4
2	3	1	3.450	-	4

the chains the spins order ferromagnetically while the chains order antiferromagnetic with respect to each other. The system is overall considered to be a 1d Ising system as the interchain coupling is very large relative to the intrachain coupling. The Ising order of the system will disappear at the same time as the antiferromagnetic order since 1d magnetism does not exist at $T > 0$, according to the Mermin–Wagner theorem [6]. Cobalt (Co^{2+}) is a transition metal and has an unfilled outer shell which gives rise to magnetic properties. The unfilled shell is a $3d^7$ shell with L = 3 and S = $\frac{3}{2}$.
Jens Jensen has made a program which makes it possible to calculate the excitations. It uses a cluster model with three Co ions, which is illustrated in figure 8.4. On can get improved results by using larger clusters, *i.e.* more Co ions, but three is sufficiently to get good results. The chains couple antiferromagnetically via J_{1c} and J_1. Inside a chain the spins couple ferromagnetically via the exchange constant J_0, and the ferromagnetic coupling is described by J_2. The exchange coupling parameters for $CoCl_2 \cdot D_2O$ are $J_0 = 0.6$ meV, $J_1 = -0.27$ meV, $J_{1c} = -0.135$ meV and $J_2 = -0.05$ meV. Figure 8.15 shows the calculated excitations of the soft and the hard mode along with the measure-

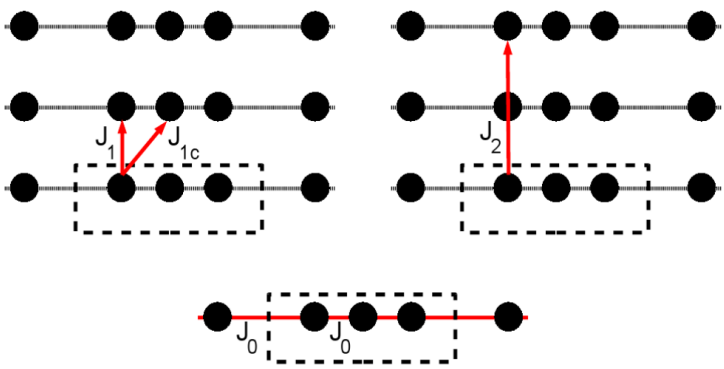

Figure 8.4: How the spins couple to their surroundings. J_0 is the coupling of the spins along the chain, J_{1c} couples the adjacent chains antiferromagnetically and J_2 is a ferromagnetic coupling, figure taken from [21].

ments which will be discussed in section 8.4.4. The easy axis of a crystal is the axis which is the energetically favourable direction of the spins. Therefore it is desirable to measure the spins component along this direction. In order to get the magnetic field perpendicular to the easy axis, the crystal was mounted on a sample holder. The configuration can be seen on figure 8.6. In this way [010] and [201] were in the scattering plane. Figure 8.7

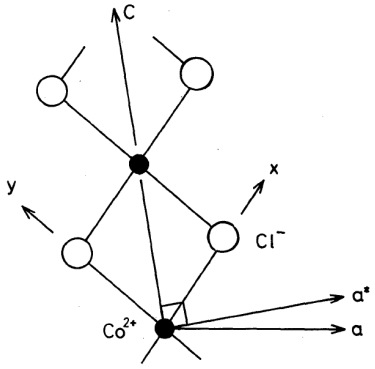

Figure 8.5: Axes of $CoCl_2 \cdot 2D_2O$. The a^* axis is in reciprocal space, a is not parallel with a^* because the crystal is not cubic. x and y are respectively the magnetic easy and hard axis [30].

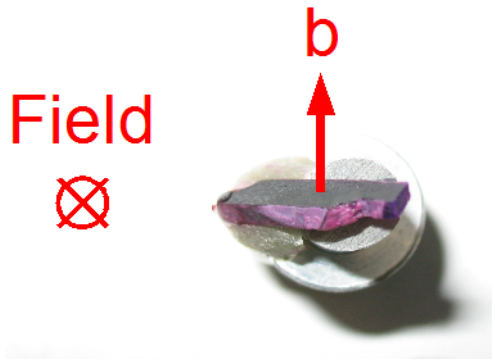

Figure 8.6: The $CoCl_2 \cdot D_2O$ sample with the crystallographic b-axis pointing up and the magnetic field going into the plane. With this configuration the easy axis of the sample should be along the direction of the magnetic field, figure taken from [21].

shows the magnetization of $CoCl_2 \cdot 2D_2O$, measured by Mollymoto *et al.* [30], when a magnetic field is applied along different crystallographic axes. Along the c axis, there are two phase transitions, as can be seen by the sudden change in magnetization at $H_{c1} = 32$ kOe and $H_{c2} = 46$ kOe. For a transverse magnetic field, the x axis is the easy axis (for a longitudinal field it is the z axis). The quantum phase transition where $H_c \parallel x$ occurs at 162 kOe. The phase transition with $H \parallel y$ is not so clear from the magnetization curves, but is clear from $\frac{dM}{dt}$ that the transition is present [30]. We will be looking for the phase transition at $H_c \parallel x$.

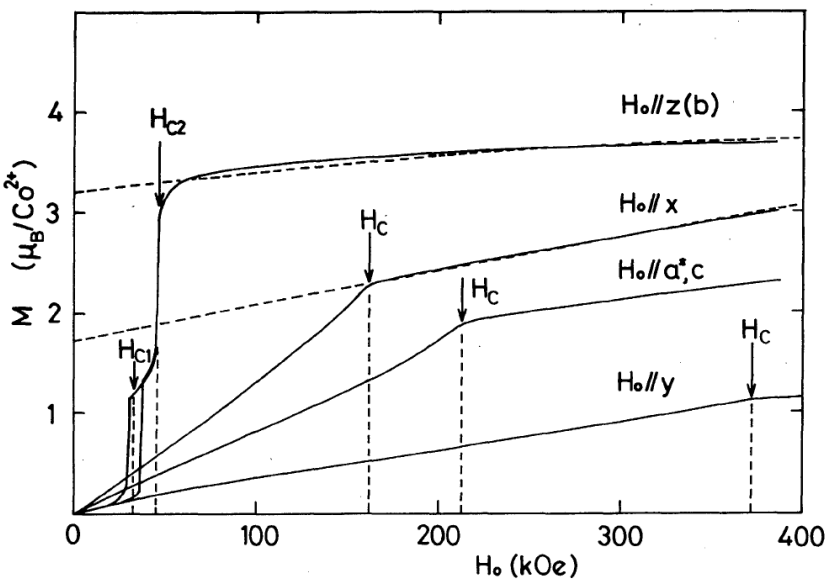

Figure 8.7: Magnetization curves of $CoCl_2 \cdot 2D_2O$ for each of the axes at 1.3 K measured by Mollymoto [30]. The transition from antiferromagnet to paramagnet at H_c for different directions is indicated with arrows.

8.4 Measurements at The Berlin Neutron Scattering Center on FLEX

8.4.1 FLEX

The neutron scattering experiments were performed on V2 also known as FLEX at The Berlin Neutron Scattering Center (BENSC). The FLEX instrument is a triple-axis spec-

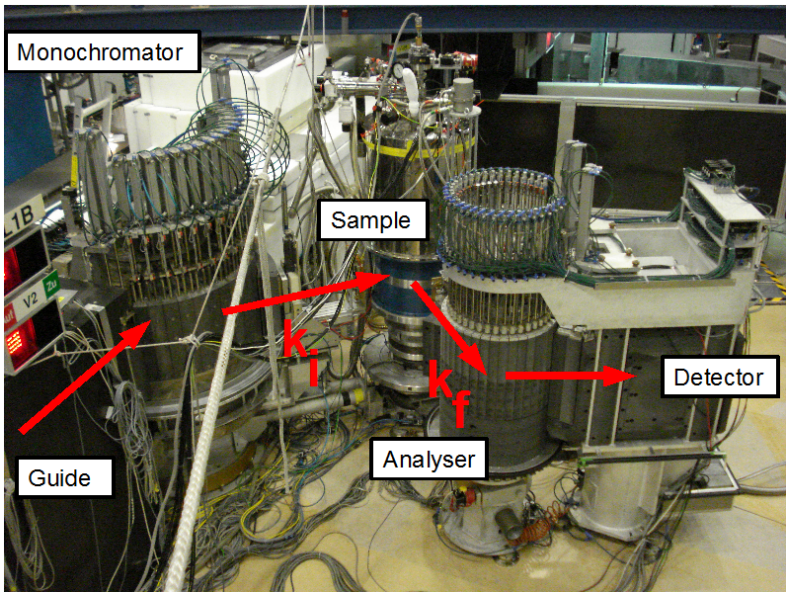

Figure 8.8: The FLEX instrument at HZB in Berlin, figure taken from [21].

trometer which uses cold neutrons with wavelengths between 1.7 Å and 6.5 Å corresponding to energies between 1.9 meV and 27 meV [47]. Figure 8.8 shows a picture of FLEX. The instrument has the possibility to use a superconducting magnet and a cryostat. The superconducting magnet can deliver up to 15 T, but it is possible to have an extra 2.5 T by using two dysprosium rods, making a field up to 17.5 T possible. This is the largest available magnetic field for a neutron scattering experiment worldwide.

8.4.2 Elastic Measurements

The aim was to determine the exact critical field and find the critical exponent β. This

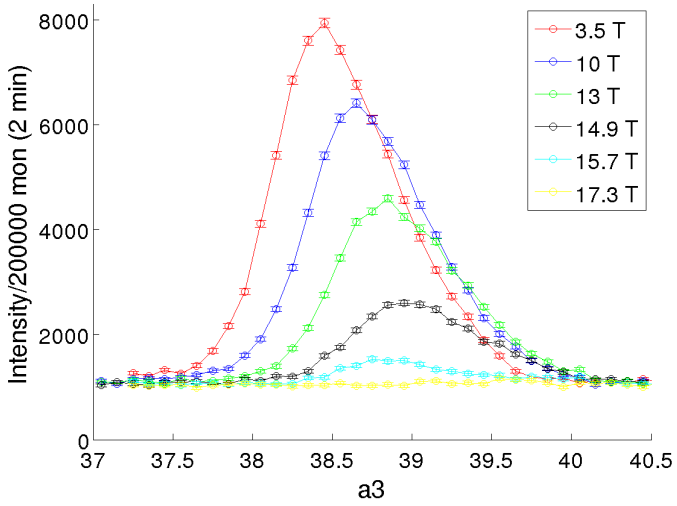

Figure 8.9: A selection of elastic data from FLEX at the [2 1 1] Bragg top. a3 scans performed at different magnetic fields from 3.5 T to 17.3 T - all at 1.5 K.

can be done by measuring how the order parameter decreases as the field increases.The critical exponent β depends on the critical field H_c. It depends on the dimensionality of the system, both the spatial dimension, d and the spin dimension D - such as Ising, X-Y or Heisenberg [32]. β can be measured using neutron scattering, as the square of the order parameter (the magnetization) is proportional to the intensity

$$I \propto m^2 \propto \left(\frac{H_c - H}{H_c}\right)^{2\beta} \tag{8.6}$$

The elastic scans shown in figure 8.9 were performed at a constant temperature of 1.5 K, some of them are shown in figure 8.9. We rotate the a3 motor, the motor rotating the sample around a horizontal axis. Each scan point is measured until a certain number of neutrons have gone through the monitor. The elastic signals have been fitted to two gauss functions because of the mosaicity of the crystal. Having fitted each a3 scan it is possible to fit the maximum intensity as a function of magnetic field to a power law, see equation (8.6). Figure 8.10 shows the maximum intensity for each magnetic field, each point corresponds to an a3 scan. With this information it is possible to fit the data and find β and the exact critical field T_c. They are found to be $\beta = 0.403 \pm 0.009$ and $\mu_0 H_c = 15.97 \pm 0.015$.

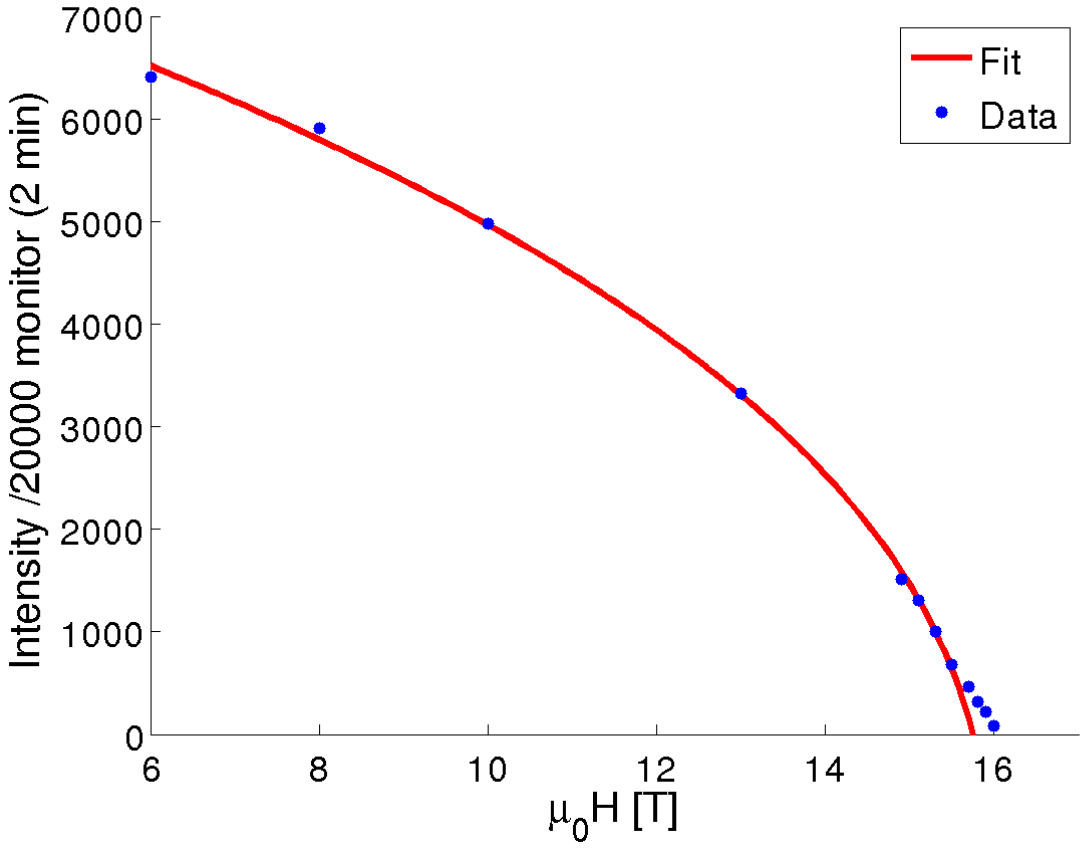

Figure 8.10: The intensity as a function of applied field, making it possible to find the order parameter β [22].

8.4.3 Phase Diagram

Figure 8.11 shows the experimentally determined phase diagram for $CoCl_2 \cdot D_2O$. Data up to 14.9 T were taken at the another triple-axis spectrometer at the Paul Scherrer Institute (PSI), RITA II. The measurements at FLEX contributed the last point at 15.98 T.

8.4.4 Inelastic Measurements

According to Jens Jensen's program $CoCl_2 \cdot 2D_2O$ should have two excitation modes. At lower transverse fields the two modes are at the same energy, one being much stronger than the other. Therefore only one mode is visible, but at higher fields they move away from each other, making them both visible. One mode softens (goes to zero) and the other mode stays around the initial value of the energy of about 3 meV, as illustrated in figure 8.15. When the measurements were performed the final energy E_f was kept constant, while the incoming energy E_i was varied. Figure 8.12 and Figure 8.13 shows previous measurements of the modes. Here one mode can be seen at 4 T, and both the hard and soft mode at 14.9 T. Figure 8.14 shows the single inelastic scan performed at FLEX at 15.2 T, here only the soft mode is present. The hard mode should be present at about 3 meV but this energy is not within the range of this scan. Figure 8.15 shows

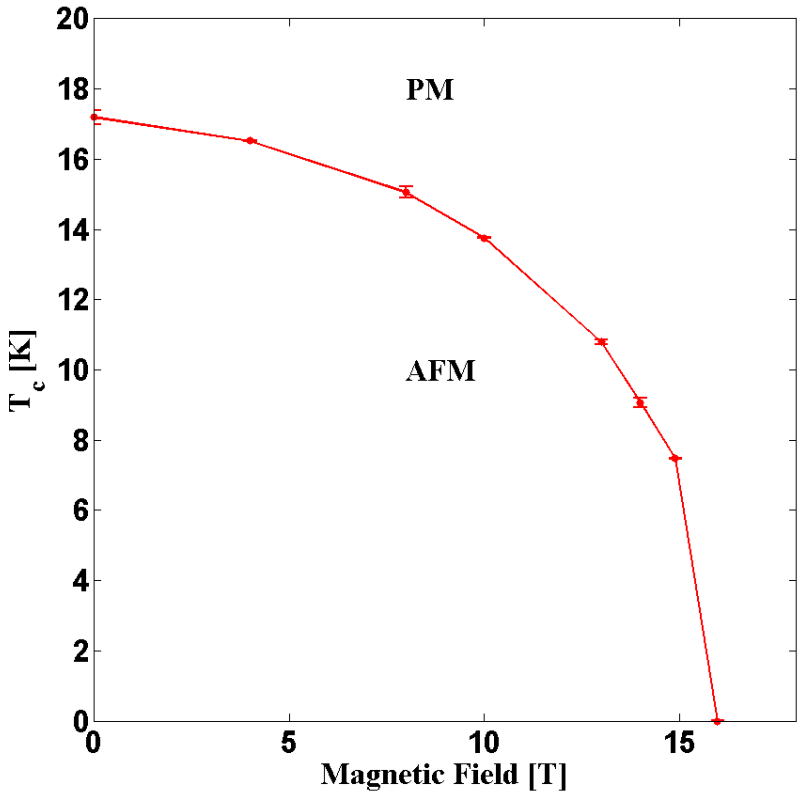

Figure 8.11: The measured phase diagram showing the transition from antiferromagnet AFM to paramagnet PM [21].

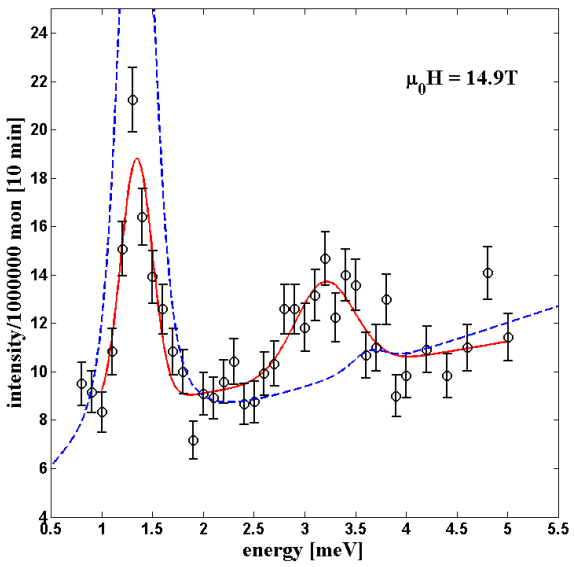

Figure 8.12: Inelastic scan at 14.9 T, data taken by [21] at the neutron instrument RITA II, PSI.

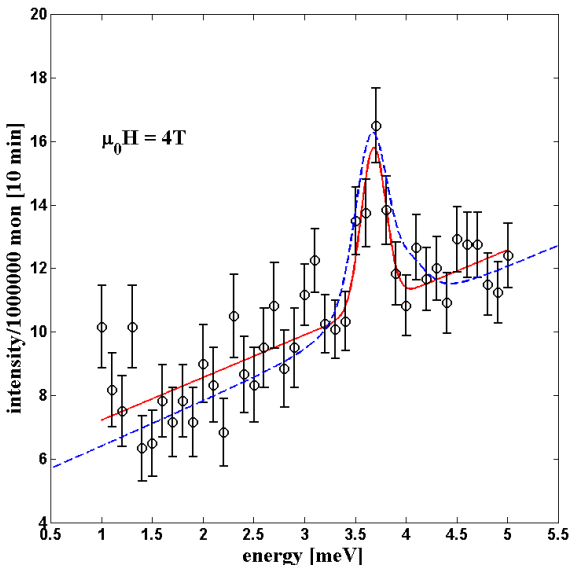

Figure 8.13: Inelastic scan at 4 T, data taken by [21] at the neutron instrument RITA II, PSI.

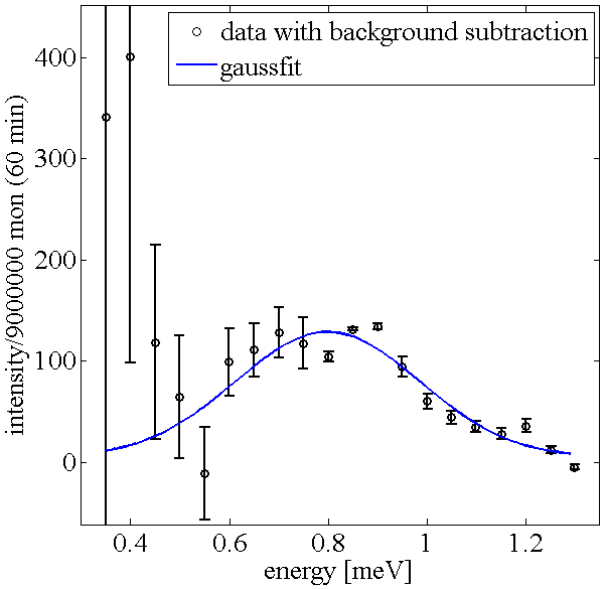

Figure 8.14: Inelastic scan at 15.2 T measured at FLEX. Only one mode is seen, the hard mode should be present at about 3 meV which is higher in energy than measured in this scan.

both modes. One can see the lower mode softens which is in agreement with the theory (blue lines). The excitation energies of the two modes has been measured as a function of magnetic field. Each scan point took about an hour plus, for some points, another hour for background measurements. To the left one can see the large elastic signal.

8.5 Conclusion on Neutron Scattering Experiments

8.5.1 Elastic Measurements

It is now safe to say that there definitely is a quantum phase transition close to 16 T. It was possible to fit the intensity to a power law and therefore β is now known to be 0.403 ± 0.009.

8.5.2 Inelastic Measurements

It was possible to add one point to the excitation energy for the lowest mode in figure 8.15, here one can also see that the energy gap goes to zero as predicted for a quantum phase transition by both 1d Ising theory in chapter 2 and the Jens Jensen theory.
The new physical results discovered in Berlin will imply that new experiments will be carried out at the new research reactor FRM II in Munich, which is ideal for these kind of measurements due to its high neutron flux.

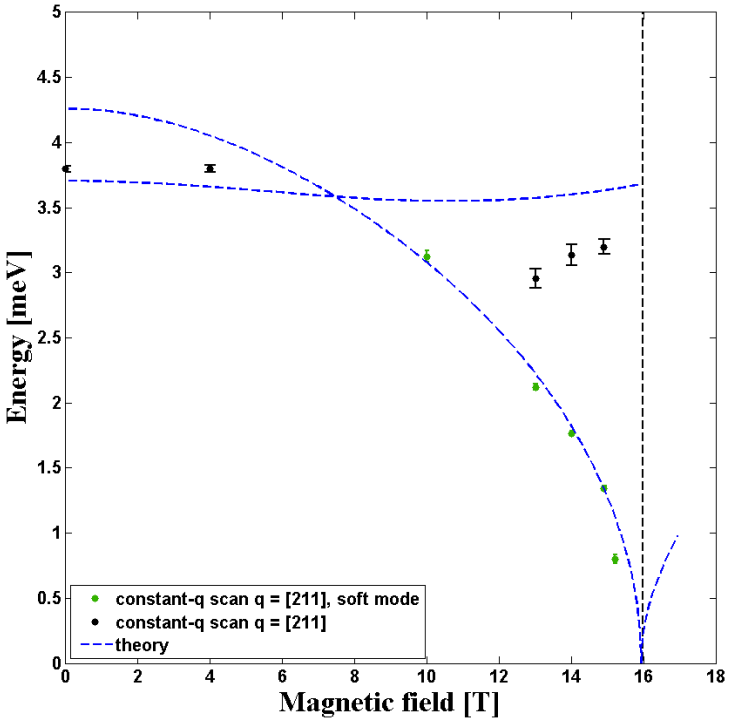

Figure 8.15: The excitation energies of the two modes as a function of magnetic field. Each scan point took about an hour plus another hour for background measurements. The large signal to the left of the figure is the elastic signal. The soft mode (green colour) goes two zero at 16 T. The hard mode stays at the initial energy of around 3 meV. The last point at 15.2 T has been measured at FLEX, the others at RITA II, PSI. This is in reasonable agreement with the theory represented by blue lines.

Chapter 9

Conclusion and Outlook

9.1 Conclusion

This thesis has shown that it was possible to build a torque magnetometer which functioned inside a dilution refrigerator. The setup showed to measure with a good resolution. The noise could be determined from the error bars and are approximately $1 \cdot 10^{-10}$ $\frac{\mathrm{V}}{\mathrm{T}}$ corresponding to $2 \cdot 10^{-3} < J_z >$.
The calibration to units of J_z was possible by using the mean field program made by Bastian Dalla Piazza.
The measurements did not agree with our original expectations, but the data analysis explained this discrepancy. The fact that the setup was not perfectly aligned turned out to explain the lack of the phase transition. The fact that the applied field was not transverse to the spin direction, completely smeared the transition in such an extent that it was no longer visible.
The mean field calculations and the measurements showed to agree well, especially the field scans had a very good agreement between data and theory.
The temperature scans were not all easy to compare with theory. The lowest measured field 0.05 T is on the limit of what the setup can measure. Therefore it is not surprising that it was difficult make it correspond with theory. At 3 T the measurements and theory were in fairly good agreement, but at higher fields the slope of the theory curve was too low. The reason for this discrepancy is not clear. Changing the exchange coupling in the calculations did not have an effect. The setup did not show to have any problems measuring high field at the field scans, which makes it unlikely to be the setup not being able to measure high fields.
The hysteresis seen at 50 mK was measured to have a coercive field which corresponds to the theoretical field from the hyperfine term in the Hamiltonian. This could be due to the hyperfine interaction, which has previously been confirmed to interfere with the electronic mode softening expected for a phase transition.
The temperature scans performed at 0.1 T and 0.2 T displayed an abrupt change in magnetization at temperatures from 140 mK to 200 mK, the reason for this change is unclear. It could be caused by the hyperfine interaction which has been measured to have an effect below 310 mK. Another possibility is that this change in magnetization is due to some background signal from the setup.

9.2 Outlook

9.2.1 Experimental Setup

Even though it was successful to measure the magnetization of $LiHoF_4$ at low temperatures, there is room for improvement in the setup. The angle between the cantilever and the applied field needs to be controlled when the setup is inside the dilution refrigerator. Thus making sure the applied magnetic field is transverse with respect to the cantilever and sample. This could be done by installing a piezoelectric motor which works inside a dilution refrigerator

9.2.2 Further Measurements

With a new improved setup it would be interesting to investigate the coupling to the nuclear spin. Partially by looking more into the second phase further, which occurred at low fieldsin the temperature scansand partially by looking into the low temperature hysteresis. To know at which temperature the hysteresis stops it is necessary to perform field scans at more temperatures.
Another important issue is the relaxation processes, we think that some nuclear relaxation could explain why the sample was more difficult to magnetize after 2.5 hours at low temperature in zero field. One could simply try and leave the sample for different time intervals start the measurements again and see how/if this changes the hysteresis.
It is desirable to have the magnetization in units of the Bohr magneton μ_B, performing the calibration on the same lock-in would facilitate the calibration thus making this possible.

9.2.3 NMR

One of the goals behind this project was to be able to control the interactions within the compound with a "handle" whilst measuring the sample properties through magnetization. This handle was thought to be NMR where manipulating the nuclear spins gains an indirect control over the electronic magnetism. This setup could be expanded in such a way if a coil emitting a radio frequency signal was installed around he cantilevers. Thereby also having another window for understanding how the hyperfine coupling influence the electronic moments.

9.2.4 Copper Nickel Alloy Strain Gauges

From this thesis it it is clear that the Cu-Ni alloy strain gauges could not be used. These strain gauges were very constant as a function of temperature but not as a function of field. The Ni clusters become magnetic at low temperatures, the dilution of Cu seem to turn the constantan alloy into a spin glass. Copper is non-magnetic and will separate the Ni-atoms from each other thus keeping them from ordering. At a certain concentration of Ni the Cu-Ni alloy will order. Actually it is possibly that we have seen a quantum phase transition as a function of the concentration of nickel at low temperatures. This was not within the idea of the project, but very interesting nonetheless. One could try to investigate Cu-Ni thin films further to see if it really behaves as a spin glass and if a quantum phase transition is present as a function of Cu dilution.

Bibliography

[1] Jens Als-Nielsen and Des McMorrow. *Elements of Modern X-Ray Physics*. John Wiley & Sons Inc., 2000.

[2] Neil W. Ashcroft and N. David Mermin. *Solid State Physics*. Brooks/Cole Thomson Learning, 1976.

[3] Varsha Banerjee and Sushanta Dattagupta. Model quantum magnet: The effect of hyperfine interactions on the phase diagram and dynamic susceptibility. *Phys. Rev. B*, 64:024427, 2001.

[4] D. Bitko, T. F. Rosenbaum, and G. Aeppli. Quantum critical behaviour for a model magnet. *Phys. Rev. Lett.*, 77(5):940–943, 1996.

[5] David Bitko. *Order and disorder in a model quantum magnet*. PhD thesis, The University of Chicago, August 1997.

[6] Stephen Blundell. *Magnetism in Condensed Matter*. Oxford University Press, 2001.

[7] D. I. Bower. Temperature dependence of gauge factor and magnetoresistance of some platinum-tungsten strain gauges. *Journal of Physics E: Scientific Instruments*, 5(9):846 – 848, 1972.

[8] Henrik Bruus and Karsten Flensberg. *Many Body Quantum Theory in Condensed Matter Physics*. Oxford University Press, 2004.

[9] D.E. Cox, B.C. Frazer, and G. Shirane. The magnetic structure of $CoCl_2 \cdot D_2O$. *Physics Letters*, 17(2):103 – 104, 1965.

[10] Nathaniel Craig and Ted Lester. *Hitchhiker's Guide to the Dilution Refrigerator*. Marcus Lab, Harvard University, 2004.

[11] DTU. *The DTU measurement setup (manual)*. Technical University of Denmark, Department of Physics.

[12] Theo Hahn. *International Tables for Crystallography, Volume A. Space Group Symmetry*. Springer, 2002.

[13] Ole Per Hansen, Malte Olsen, and Finn Berg Rasmussen. Køling ved blanding af heliumisotoper. *Fysisk Tidsskrift 73*, 4, 1975.

[14] P. E. Hansen, T. Johansson, and R. Nevald. Magnetic properties of lithium rare-earth fluorides: Ferromagnetism in $LiErF_4$ and $LiHoF_4$ and crystal-field parameters at the rare-earth and Li sites. *Physical Review B*, 12(11):5315 – 5324, 1975.

[15] M. T. Hutchings. Point-charge calculations of energy levels of magnetic ions in crystalline electric fields. *Solid State Physics*, 16:227 – 273, 1965.

[16] K. D. Jayasuriya, A. M. Stewart, and S. J. Campbell. The specific heat capacity of GE varnish (200-400 K). *Journal of Physics E: Scientific Instruments*, 15:885 – 886, 1982.

[17] Jens Jensen and Allan R. Mackintosh. *Rare earth magnetism: Structures and Excitations.* Oxford University Press, 1991.

[18] C. Keller and H. Schmutz. Die reaktion von lithiumfluorid mit den trifluoriden der lanthaniden und einiger actiniden. *Journal of Inorganic and Nuclear Chemistry*, 27(4):900 – 901, 1965.

[19] Charles Kittel and Herbert Kroemer. *Thermal physics.* W. H. Freeman and Company, 1980.

[20] Conradin Kraemer. *Quantum Phase Transitions in a Magnetic model System.* PhD thesis, ETH Zürich, July 2009.

[21] Jacob Larsen. Quantum phase transition of the near-Ising antiferromagnet $CoCl_2 \cdot 2D_2O$. Master's thesis, University of Copenhagen, August 2009.

[22] Jacob Larsen et al. Quantum phase transition in $CoCl_2 \cdot D_2O$. In preparation.

[23] Kim Lefmann. Neutron Scattering: Theory, Instrumentation, and Simulation, Course Notes, University of Copenhagen, August 2009.

[24] J. Magariño, J. Tuchendler, P. Beauvillain, and I. Laursen. EPR experiments in $LiTbF_4$ $LiHoF_4$ and $LiErF_4$ at submillimeter frequencies. *Phys. Rev. B*, 21(1):18–28, 1980.

[25] Michael P. Marder. *Condensed Matter Physics.* John Wiley & Sons Inc., 2000.

[26] Daniel C. Mattis. *The Theory of Magnetism Made Simple.* World Scientific, 2006.

[27] G. Mennenga, L. J. de Jongh, and W. J. Huiskamp. Field dependent specific heat study of the dipolar Ising ferromagnet $LiHoF_4$. *Journal of Magnetism and Magnetic Materials*, 44(1-2):59 – 76, 1984.

[28] G. Mennenga, L. J. de Jongh, W. J. Huiskamp, and I. Laursen. A comparative study of the magnetic ordering specific heats of four dipolar magnets: LiRF4 (R = Er, Dy, Ho, Tb). *Journal of Magnetism and Magnetic Materials*, 44(1-2):48 – 58, 1984.

[29] Sushil K. Misra and Joshua Felsteiner. Low-temperature ordered states of lithium rare-earth tetrafluorides LiRF4. *Phys. Rev. B*, 15(9):4309–4312, 1977.

[30] Hiroshi Mollymoto, Mitsuhiro Motokawa, and Muneyuki Date. High field transverse magnetization of ising antiferromagnet $CoCl_2 \cdot D_2O$. *Journal of the Physical Society of Japan*, 49(1):108–114, 1980.

[31] Albert Narath. Antiferromagnetism in $CoCl_2 \cdot D_2O$. ii. chlorine nuclear magnetic resonance and paramagnetic susceptibility. *Phys. Rev.*, 140(2A):A552–A568, 1965.

[32] R. K. Pathria. *Statistical Mechanics*. Butterworth-Heinemann, 1996.

[33] Julian Piatek. Characterisation of $LiHo_xEr_{1-x}F_4$ alloyed model magnets. Master's thesis, École Polytechnique Fédérale de Lausanne, January 2009.

[34] Bastian Dalla Piazza. Mean-Field calculations on the diluted dipolar magnet $LiHo_{1-x}Y_xF_4$. Master's thesis, École Polytechnique Fédérale de Lausanne, January 2009.

[35] Frank Pobell. *Matter and Methods at Low Temperatures*. Springer Verlag, 2007.

[36] John R. Reitz, Frederick J. Milford, and Robert W. Christy. *Foundations of Electromagnetic Theory*. Assison-Wesley, 1979.

[37] Henrik Rønnow. *Aspects of Quantum Magnetism in One, Two and Three Dimensions*. PhD thesis, University of Copenhagen, April 2000.

[38] Henrik Rønnow et al. Quantum phase transition of a magnet in a spin bath. *Science*, 308:389 – 392, 2005.

[39] Henrik Rønnow, Jens Jensen, et al. Magnetic excitations near the quantum phase transition in the Ising ferromagnet $LiHoF_4$. *Physical Review B*, 75:054426–1 – 054426–8, 2007.

[40] Subir Sachdev. *Quantum Phase Transition*. Cambridge University Press, 1999.

[41] Subir Sachdev. *The New Physics*, chapter Quantum Phase Transitions. Cambridge University Press, 2006.

[42] Gen Shapiro, Stephen M. Shapiro, and John M. Tranquada. *Neutron Scattering with a Triple-Axis Spectrometer Basic Techniques*. Cambridge University Press, 2002.

[43] G. Simonsen. *Vejledning i brug af 13 T magneten, og det tilhørende udstyr*, 1989.

[44] Spanish National Research Council (CSIC) - Department of Crystallography. Homepage, 2010. `http://www.xtal.iqfr.csic.es/Cristalografia/parte_06-en.html`.

[45] Stanford Research Systems. *Lock-In Amplifier, users manual*.

[46] John R. Taylor. *An introduction to Error Analysis*. Sausalito, California, 1982.

[47] Michael Tovar and Hans Anton Graf. The complete BENSC instrumentation brochure. Technical report, The Berlin Neutron Scattering Center, April 2007.

[48] Vishay. Homepage, 2010. http://www.vishay.com/strain-gages/transducer-class/list/product-11563/.

[49] Matthias Vojta. Quantum phase transitions. *Reports on Progress in Physics*, 66:2069 – 2110, 2003.

[50] Wikipedia, the free encyclopedia. Homepage, 2010. http://en.wikipedia.org/wiki/Strain_gauge.

Appendix A

List of scan performed with Pt-W Strain Gauge

A.1 Data on the Pt-W Strain Gauge with Sample

A.1.1 Temperature scans

from[K]	to[K]	rate[mK/s]	field[Tesla]	file number
0.065	4.5	0.02 - 0.5	3	36-39
4.5	0.081	0.02 - 0.5	3	40-44
4.5	0.288	0.02 - 0.5	4.95	55-58
0.065	2.2	0.02 - 0.5	0.5	80-84
0.065	3	0.1	4.5	95
0.065	3	0.1	0.2	97
0.065	3	0.1	0.050	100
0.070	3	0.1	3.5	102
0.066	3	0.1	0.1	105

A.1.2 Field scans

from[Tesla]	to[Tesla]	rate[Tesla/min]	temperature[K]	file number
0	- 0.1	0.01	0.050	6
-0.1	0.3	0.01	0.050	7
0.33	0.5	0.01	0.050	8
0.5	-0.7	0.01	0.050	9
-0.7	0.9	0.04	0.050	10
0.9	-0.98	0.02	0.050	11
0	-1.1	0.02	0.050	12
-1.1	1.3	0.02	0.050	13
1.3	-1.5	0.02	0.050	14
-1.5	-2.5	0.02	0.050	15
-2.5	-6	0.04	0.050	16
-6	-3.5	0.05	0.050	17
0	9	0.05	0.050	19
9	-6	0.05	0.050	20
-6	6	0.05	0.100	21
6	-6	0.05	0.100	22
9	-9	0.1	0.400	24
-9	9	0.1	0.600	25
9	-9	0.1	0.800	26
-9	9	0.1	1	27
-9	3.2	0.1	1.1	32
9	-9	0.1	2	33
-9	9	0.02	0.065	34
9	-9	0.1	4	85
-9	9	0.1	1.53	86
9	-9	0.1	1.4	87
-9	9	0.2	1.3	88
9	-9	0.2	1.2	89

A.2 Data on the Pt-W Strain Gauge without Sample

A.2.1 Temperature scans

from[K]	to[K]	rate[mK/s]	field[Tesla]	file number
0.052	3	0.02 - 0.5	0	60-64
2	0.053	0.02 - 0.5	9	69-73

A.2.2 Field scans

from[Tesla]	to[Tesla]	rate[Tesla/min]	temperature[K]	file number
-3.5	0	0.05	0.050	18
-6	6	0.1	0.050	23
9	-9	0.2	1	28
9	-9	0.1	0.065	59
9	-9	0.1	2	67
-9	9	0.1	2	68